RD-E 300 175

12

DNA 4361F

AD A053462

RESPONSE OF EARTH PENETRATOR STRUCTURES IN ANGLE-OF-ATTACK IMPACTS

SRI International
333 Ravenswood Avenue
Menlo Park, California 94025

June 1977

Final Report for Period 1 November 1975—31 October 1976

CONTRACT No. DNA 001-74-C-0140

THIS WORK SPONSORED BY THE DEFENSE NUCLEAR AGENCY
UNDER SUBTASK L41AAXYX966-05.

Prepared for
Director
DEFENSE NUCLEAR AGENCY
Washington, D. C. 20305

Destroy this report when it is no longer needed. Do not return to sender.

UNCLASSIFIED

SECURITY CLASSIFICATION OF THIS PAGE (When Data Entered)

REPORT DOCUMENTATION PAGE

READ INSTRUCTIONS BEFORE COMPLETING FORM

1. REPORT NUMBER: DNA 4361F

2. GOVT ACCESSION NO.

3. RECIPIENT'S CATALOG NUMBER

4. TITLE (and Subtitle): RESPONSE OF EARTH PENETRATOR STRUCTURES IN ANGLE-OF-ATTACK IMPACTS.

5. TYPE OF REPORT & PERIOD COVERED: Final Report, [redacted] 1 Nov 75—31 Oct 76

6. PERFORMING ORG. REPORT NUMBER: SRI PYU 3091

7. AUTHOR(s): J. D. Colton, [redacted] J. K. Gran, H. E. Lindberg, R. E. Emerson

8. CONTRACT OR GRANT NUMBER(s): DNA 001-74-C-0140

9. PERFORMING ORGANIZATION NAME AND ADDRESS: SRI International, 333 Ravenswood Avenue, Menlo Park, California 94025

10. PROGRAM ELEMENT, PROJECT, TASK AREA & WORK UNIT NUMBERS: NWED Subtask L41AAXYX966-05; X966

11. CONTROLLING OFFICE NAME AND ADDRESS: Director, Defense Nuclear Agency, Washington, D.C. 20305

12. REPORT DATE: Jun[redacted]77

13. NUMBER OF PAGES: 124 [illegible] 125

14. MONITORING AGENCY NAME & ADDRESS (if different from Controlling Office): DNA, SBIE, 4361F AD-E340 175, WU 05

15. SECURITY CLASS (of this report): UNCLASSIFIED

15a. DECLASSIFICATION/DOWNGRADING SCHEDULE

16. DISTRIBUTION STATEMENT (of this Report)

Approved for public release; distribution unlimited.

LPN - SRI - PYU - 3091

17. DISTRIBUTION STATEMENT (of the abstract entered in Block 20, if different from Report)

18. SUPPLEMENTARY NOTES

This work sponsored by the Defense Nuclear Agency under Subtask L41AAXYX966-05.

19. KEY WORDS (Continue on reverse side if necessary and identify by block number)

Earth Penetrator
Penetration
Explosive Simulation Experiments
Critical Impact
Shallow Burst Munition

20. ABSTRACT (Continue on reverse side if necessary and identify by block number)

An analysis based on a one-dimensional beam-mass model was developed to predict the early-time response of penetrator structures in angle-of-attack impacts. The model was verified by comparison with the strain response measured in a reverse ballistics test ~~performed by Avco~~ and with the strain response measured in idealized scale model penetrators ~~tested under this contract~~. Loads were simulated by a device that produces the resultant force-time history near the front end of the penetrator. The tests indicated that the loader could be

DD FORM 1 JAN 73 1473 EDITION OF 1 NOV 65 IS OBSOLETE

UNCLASSIFIED

SECURITY CLASSIFICATION OF THIS PAGE (When Data Entered)

410 281

20. ABSTRACT (Continued)

built in a larger size to test full-scale penetrators. The analysis was then used to investigate penetrator response. It was found that the peak compressive strain, which determines whether or not the penetrator casing fails, depends on the magnitude of the lateral load produced by impacts at an angle of attack, the load rise time (which is inversely proportional to impact velocity), and the relative mass of the nose and aft sections. Finally, a procedure was devised to characterize the strength of penetrator structures in terms of impact velocity and angle of attack. The resulting critical impact curves can be used to make tradeoffs among structural dimensions (e.g., length and wall thickness), to select the best structure for a particular application, and to provide a framework for planning and interpreting experiments and more detailed calculations.

PREFACE

This investigation was performed from November 1975 to October 1976 in the Poulter Laboratory of SRI International. The unique approach was to characterize the strength of penetrator structures under angle-of-attack impacts.

The authors wish to thank G. R. Abrahamson for suggesting the basic approach taken here, Lieutenant R. Nibe for monitoring the contract and providing overall guidance, J. E. Malinak for developing the structural response analysis, D. Witherly for suggestions in the design of the loader and for completing the design as a set of drawings, L. Dary and T. Henry for assembling the loader, D. Walter for recording the response, H. Rudnicki for making the high-speed photographs, H. Hanna for installing and detonating the explosive charges, and N. Smith for typing the manuscript.

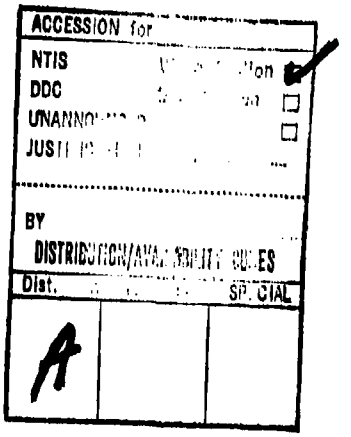

Conversion factors for U.S. customary to metric (SI) units of measurement.

To Convert From	To	Multiply By
angstrom	meters (m)	1.000 000 X E -10
atmosphere (normal)	kilo pascal (kPa)	1.013 25 X E +2
bar	kilo pascal (kPa)	1.000 000 X E +2
barn	meter^2 (m^2)	1.000 000 X E -28
British thermal unit (thermochemical)	joule (J)	1.054 350 X E +3
calorie (thermochemical)	joule (J)	4.184 000
cal (thermochemical)/cm^2	mega joule/m^2 (MJ/m^2)	4.184 000 X E -2
curie	*giga becquerel (GBq)	3.700 000 X E +1
degree (angle)	radian (rad)	1.745 329 X E -2
degree Fahrenheit	degree kelvin (K)	$t_K = (t°f + 459.67)/1.8$
electron volt	joule (J)	1.602 19 X E -19
erg	joule (J)	1.000 000 X E -7
erg/second	watt (W)	1.000 000 X E -7
foot	meter (m)	3.048 000 X E -1
foot-pound-force	joule (J)	1.355 818
gallon (U.S. liquid)	meter^3 (m^3)	3.785 412 X E -3
inch	meter (m)	2.540 000 X E -2
jerk	joule (J)	1.000 000 X E +9
joule/kilogram (J/kg) (radiation dose absorbed)	Gray (Gy)	1.000 000
kilotons	terajoules	4.183
kip (1000 lbf)	newton (N)	4.448 222 X E +3
kip/inch^2 (ksi)	kilo pascal (kPa)	6.894 757 X E +3
ktap	newton-second/m^2 ($N-s/m^2$)	1.000 000 X E +2
micron	meter (m)	1.000 000 X E -6
mil	meter (m)	2.540 000 X E -5
mile (international)	meter (m)	1.609 344 X E +3
ounce	kilogram (kg)	2.834 952 X E -2
pound-force (lbs avoirdupois)	newton (N)	4.448 222
pound-force inch	newton-meter (N·m)	1.129 848 X E -1
pound-force/inch	newton/meter (N/m)	1.751 268 X E +2
pound-force/foot^2	kilo pascal (kPa)	4.788 026 X E -2
pound-force/inch^2 (psi)	kilo pascal (kPa)	6.894 757
pound-mass (lbm avoirdupois)	kilogram (kg)	4.535 924 X E -1
pound-mass-foot^2 (moment of inertia)	kilogram-meter^2 ($kg·m^2$)	4.214 011 X E -2
pound-mass/foot^3	kilogram/meter^3 (kg/m^3)	1.601 846 X E +1
rad (radiation dose absorbed)	**Gray (Gy)	1.000 000 X E -2
roentgen	coulomb/kilogram (C/kg)	2.579 760 X E -4
shake	second (s)	1.000 000 X E -8
slug	kilogram (kg)	1.459 390 X E +1
torr (mm Hg, 0° C)	kilo pascal (kPa)	1.333 22 X E -1

*The becquerel (Bq) is the SI unit of radioactivity; 1 Bq = 1 event/s.
**The Gray (Gy) is the SI unit of absorbed radiation.

A more complete listing of conversions may be found in "Metric Practice Guide E 380-74," American Society for Testing and Materials.

CONTENTS

ILLUSTRATIONS

TABLES

1. SUMMARY

Recent work on earth penetrating devices[1-6] has focused on the terradynamics of the target material and on the structural response of the penetrator. Test results[5-6] show that large bending strains can be produced in the penetrator casing when it is impacted at an angle of attack of only a few degrees. When these strains exceed the yield strain, local weakening of the cross section leads to breakup of the penetrator; thus it is desirable to keep the penetrator response elastic. Because this response is sensitive to both impact velocity V and angle of attack α, a tradeoff in these two impact parameters can be made in the design of an earth penetrator. The primary objective of our work was to determine this tradeoff in the form of critical impact curves for representative penetrator structures. A second objective was to demonstrate that an explosive loading technique can be used to simulate angle-of-attack impacts in the laboratory.

Construction of critical impact curves requires knowledge of both the structural response of the penetrator and the response of the target material (terradynamic response). In this work these two responses were treated independently, then combined by matching the terradynamic loads with the loads applied to the penetrator structure.

Structural response was calculated with a mathematical model based on elastic Timoshenko beam theory with axial thrust. This model allows efficient calculation of the elastic response of penetrators under combined axial and lateral loading. The peak response stress was calculated for a range of load rise times and axial and lateral load amplitudes.

Terradynamic response and the associated loads that are applied to the penetrator structure are not easily determined. However, available experimental data and computer code calculations show that the loads have three characteristics. First, the shape of the resultant load

history rises lineraly to a peak, followed by a constant value where the rise time is the nose length divided by the impact velocity. Second, the peak loading force is proportional to impact velocity. Third, based on comparison of calculated structural response and of response measured in an angle-of-attack reverse ballistics test, the angle between the resultant force and the penetrator axis is three times the angle of attack.

With these three load characteristics, the peak stress calculated as a function of load rise time and amplitudes can be expressed in terms of the impact velocity and angle of attack. We then can construct critical impact curves that show the combinations of V and α that produce a given level of peak strain, or factor of safety, in the structure. The principal advantage of critical impact curves is that they characterize the response over a range of impact conditions. For example, critical impact curves for four structures are shown in Figure 1.* These curves can be used to select the penetrator material, on the basis of yield stress, for a given range of V and α within which the penetrator must function. They can also be used to interpret results of experiments or interpret more detailed load and structural response calculations (e.g., a finite element code prediction). For example, the appropriate values of V and α can be selected to minimize the tests or code calculations needed to define the curve.

The critical impact curves are perhaps most useful for making design tradeoffs among candidate penetrator structures. For example, the curves for Structure B (deep penetrator) and for Structure C (shallow penetrator) pass through a similar region in the V-α plane. Both these penetrators can be made stronger by increasing only the wall thickness (from that of Structure C to that of Structure A) or by decreasing the length (from that of Structure B to that of Structure A). For small angles of attack,

---

*P_{1000} is the average pressure over the frontal area of the penetrator at an impact velocity of 1000 ft/sec and is a characteristic of the target material.

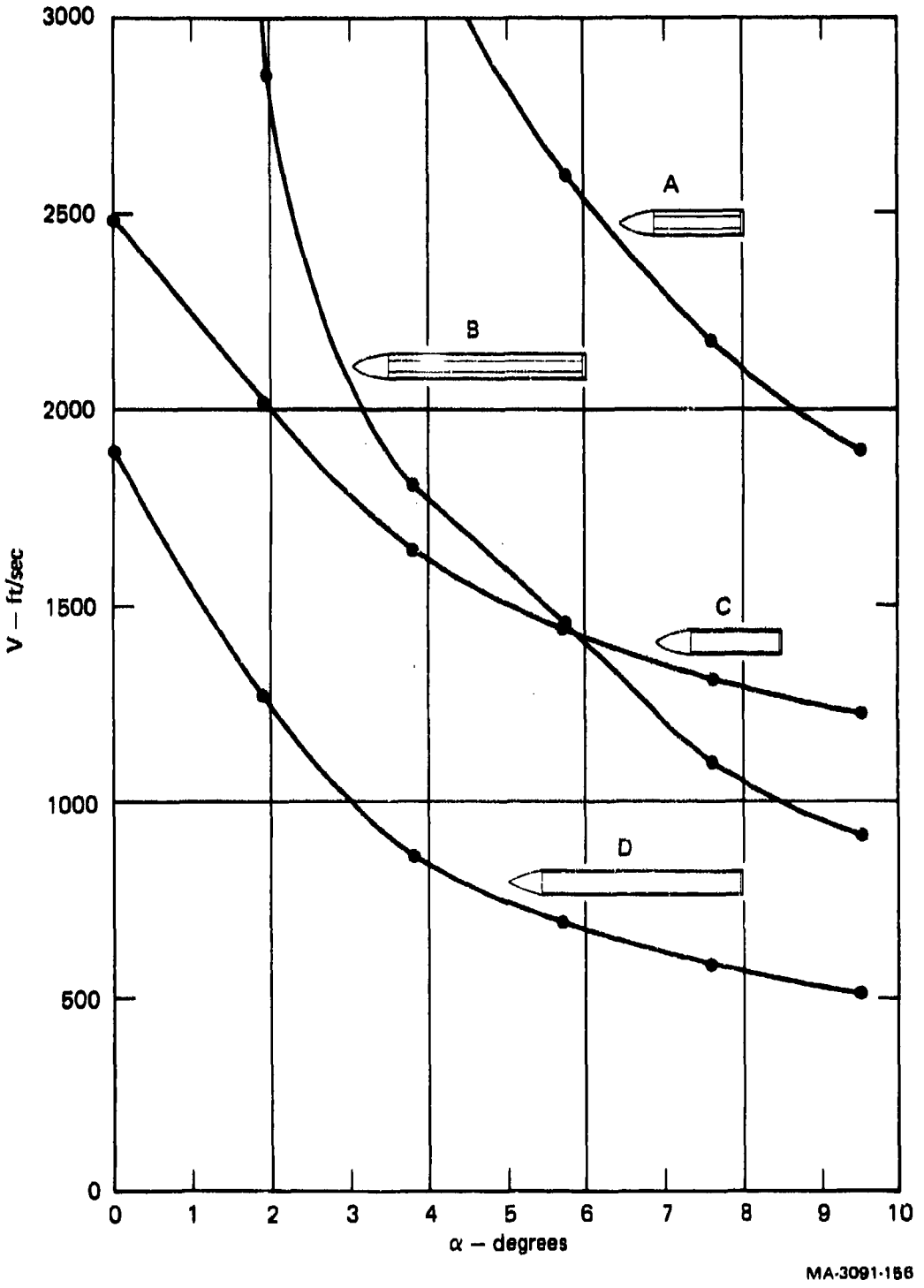

FIGURE 1 IMPACT VELOCITY VERSUS ANGLE OF ATTACK FOR CONSTANT PEAK RESPONSE STRESS FOR DIFFERENT STEEL PENETRATOR STRUCTURES (σ_{max}/P_{1000} = 10)

however, the velocity range can be extended more by increasing wall thickness than by decreasing length. Similar conclusions can be drawn by comparing curves for Structures B and C with that of Structure D.

To meet the second objective of this work, demonstration of a technique for simulating angle-of-attack impacts, we used an existing explosive simulation device. This device produces resultant axial and lateral time-varying loads similar to those occurring in angle-of-attack impacts, but not the detailed load distribution. The controlled flow of high pressure gases from a confined explosion is used to load a piston that, in turn, loads a penetrator initially at rest. Since we simulate only the damage-producing portion of the load, which extends up to and slightly beyond the maximum load, the kinetic energy impacted to the penetrator is much less than that required in ballistics tests; thus, simulator tests can be performed conveniently in the laboratory. This technique also allows hard-wired measurement of the structural response of the penetrator.

Several penetrator structures were tested in nominally 1/4 scale. For example, the model typical of deep earth penetrator structures (thick-walled model) is made of AISI 1020 steel, is 9 inches (22.9 cm) long, and has a 0.875-inch-diameter (2.22-cm-diameter) cylindrical cavity over the aft two-thirds of its length. The load produced on this penetrator at an angle of attack was simulated by tilting the model penetrator through an angle of 19°30' with respect to the penetrator axis. The peak axial compressive strain was 0.022 percent. The peak total (axial plus bending) compressive strain was about 0.042 percent. This bending response is similar to that observed in angle-of-attack reverse ballistics tests performed by AVCO.[5]

These and other test results show that the load simulator can apply to model penetrators loads similar to those occurring in angle-of-attack impacts. The tests also indicate that the loader could be built in a larger size to test full-scale penetrators.

2. INTRODUCTION AND DETAILED SUMMARY

BACKGROUND

Earth penetrating devices have potential for use as tactical weapons. Such a device would have a projectile shape and sufficient impact velocity to enter soil, soft rock, or concrete and travel into the target before a charge in the penetrator is detonated.

A variety of penetrator structures have been proposed for different impact conditions. For deep penetration into hard targets, penetrators with a radius-to-thickness ratio of about 3 and a length-to-diameter ratio of about 10 have been used.[1] A thick wall was chosen to withstand the impact stress, and a long slender shape was chosen to minimize broaching. For shallow penetration (as little as one penetrator length) into soft targets, a radius-to-thickness ratio of about 10 and a length-to-diameter ratio of 3 to 6 have been proposed.

Determining the feasibility of deploying an earth penetrating weapon requires investigation into three areas associated with impact and penetration. First, the early-time impact response of the casing must be understood so that it can be designed to stay intact and allow penetration of the target. Second, the response of the internal components must be understood so that they can be made to function after the impact. Third, the terradynamics, or motion of the penetrator through the target media, must be understood so that the system can be designed to penetrate to the required depth for detonation.

Most of the previous work on earth penetrators has focused on terradynamics.[1-3] These investigations have demonstrated experimentally that solid or thick-walled projectiles can travel tens of

feet in soil and soft rock. In addition they have yielded analytical techniques for calculating the forces on a rigid penetrator and the resulting motion of the penetrator and the target for a rigid penetrator under normal impact.[3-4]

Both calculated impact loads[4] and measured acceleration response[2] show that the resultant force-history for normal impact consists of two distinct parts, as Figure 2 illustrates: an approximately linear rise to a peak over the time t_r required for the structure to penetrate to its full diameter, and a very gradual decay associated with the rigid body deceleration of the structure. For a nominal full-scale structure [6 inches (15.24 cm) in diameter, 60 inches (152.4 cm) long, and weighing 400 pounds (181 kg)] impacting sandstone at 1500 ft/sec (457 m/sec), the loading rise time is about 1 msec and the peak force is about 500,000 pounds (224 kN).[4]

Less work has been done on determining the response of penetrator structures or internal equipment. In particular, we need to know the loads that produce damage in a penetrator casing and how these loads depend on the structural or loading parameters that are at the disposal of a designer. Nevertheless, existing results from tests on deep-penetrator structures have identified some of the important parameters. In reverse ballistic tests performed by AVCO,[5] relatively low strains were produced in a simple penetrator structure under a normal impact with a rock simulant; however, under an angle-of-attack impact, much larger strains were produced by the bending induced in the penetrator. In ballistic tests performed on scale model penetrators by Martin Marietta Aerospace Company,[6] the penetrator structure failed in angle-of-attack impacts; these tests results also indicate that large strains and failure were caused by bending.

These observed failures in penetrators under angle-of-attack impacts are postulated to occur as follows. The axial component of the load produces a compressive stress along the entire length of the penetrator. The lateral component of the load produces bending stresses whose magnitudes in tension and compression are equal at a given axial

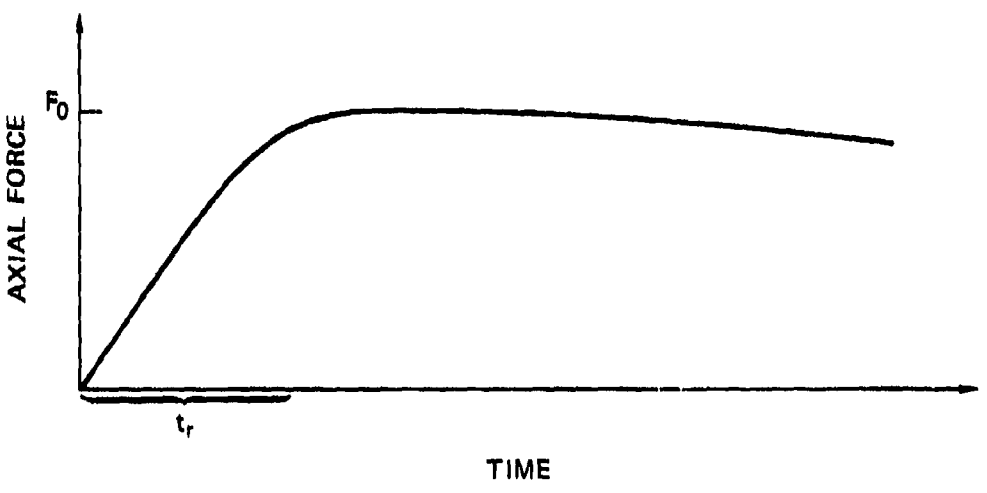

FIGURE 2 IMPACT LOAD-TIME HISTORY ON A PENETRATOR STRUCTURE

location. Thus the total stress of greatest amplitude is compressive and produces local yielding of the penetrator wall. The weakened cross section at this location then allows continued deformation and ultimately fracture under the large tensile strains at this location. Thus, incipient yielding in compression defines the onset of a divergent instability. The response that leads to yielding, that is, the elastic response, therefore determines if failure occurs. Thus the analysis need predict only the elastic response and the critical response parameter is the maximum total compressive stress.

Also, observed maximum compressive strains and failures in penetrator structures occur at distances greater than one diameter from the penetrator nose.[5-6] The stress distribution over the cross section at these locations depends only on the resultant forces applied to the end of the structure. Thus failure depends only on the resultant axial and lateral loading forces with the appropriate time-history, and not on the details of the pressure load distribution on the penetrator nose. We will see that this observation allows us to use a relatively simple experimental technique and response analysis.

OBJECTIVES AND APPROACH

The primary objectives of this work were to develop a simple analysis that accounts for penetrator bending induced by angle-of-attack impacts and to determine the effect of structural and loading parameters on the survivability of a penetrator casing on impact. These results can then be used to (1) identify those parameters to which the damage producing loads are sensitive, e.g., impact velocity and angle of attack; (2) provide a means of arriving at an optimum structural design within the parameter ranges dictated by system requirements; and (3) select specific configurations and loads for testing and for more detailed calculations.

A secondary objective was to demonstrate the capability of an explosive load simulator, already developed on a separate DNA contract,* for loading a scale model penetrator-like structure with a resultant load simulating an impact load. These experimental results were used to validate the analysis developed here. Also, by developing and demonstrating the usefulness of this device in small scale, we have made the concept readily available for testing full-scale penetrator structures.

The analytical approach to predicting penetrator response is based on elastic Timoshenko beam theory with axial thrust. This engineering theory treats the loading and response in terms of the resultant longitudinal force, transverse force, and bending moment at any cross section along the structure. The nose, aft mass, and payload are modeled as rigid masses. A one-dimensional finite difference characteristic grid along the length of the structure can then be used in the numerical solution of the governing equations. This procedure is an efficient way to calculate the elastic response of penetrators, allowing a broad range of loading and structural parameters to be examined at a low cost. It is not intended to replace more elaborate finite element and finite difference codes, but rather to supplement code calculations in the design stage when a number of configurations are being considered and structural details are yet to be determined.

The impact loads developed and their dependence on the impact conditions are not well understood, especially under angle-of-attack impacts. Therefore, the load is treated as a parameter; that is, we calculate the response for a range of loading parameters as well as for the parameters that describe the penetrator casing. The loads are related to the impact conditions through available experimental and analytical load data.

---

*Contract No. DNA001-75-C-0257

The experimental approach makes use of an existing explosive simulation device that produces resultant axial and lateral time-varying loads similar to those occurring in angle-of-attack impacts, but not the detailed load distribution. The device uses the controlled flow of high pressure gases from a confined explosion to produce loads on a penetrator initially at rest. This technique allows hard-wired measurement of the structural response of the penetrator and avoids the high velocities required to produce loads by target impact (we simulate only the damage-producing portion of the load that extends up to and slightly beyond the maximum load).

The experiments are summarized first. Then we describe the development of the analysis, comparison of predicted and measured responses, and the application of the analysis to determining critical impact curves.

EXPERIMENTS

Figure 3 is a sectioned assembly drawing of the loading fixture. As shown, it is a configuration for simulating normal impact loads on 1/4-scale model penetrators. High-pressure gaseous explosive products flow through the orifices and transmit the load to the penetrator through the piston. The rise time, duration, and decay time can be varied by using different size spacings and vent holes.

To simulate the load on a penetrator that impacts at an angle of attack, the piston is designed to produce a combined axial and lateral loading and to measure the load applied to the penetrator. The combined loading is produced by tilting the penetrator through an angle θ with respect to the piston axis. During the loading the penetrator is allowed to slide relative to the piston. The resultant vertical force history is measured with a load cell inside the piston; the resultant horizontal force history is deduced from the measured motion of the penetrator.

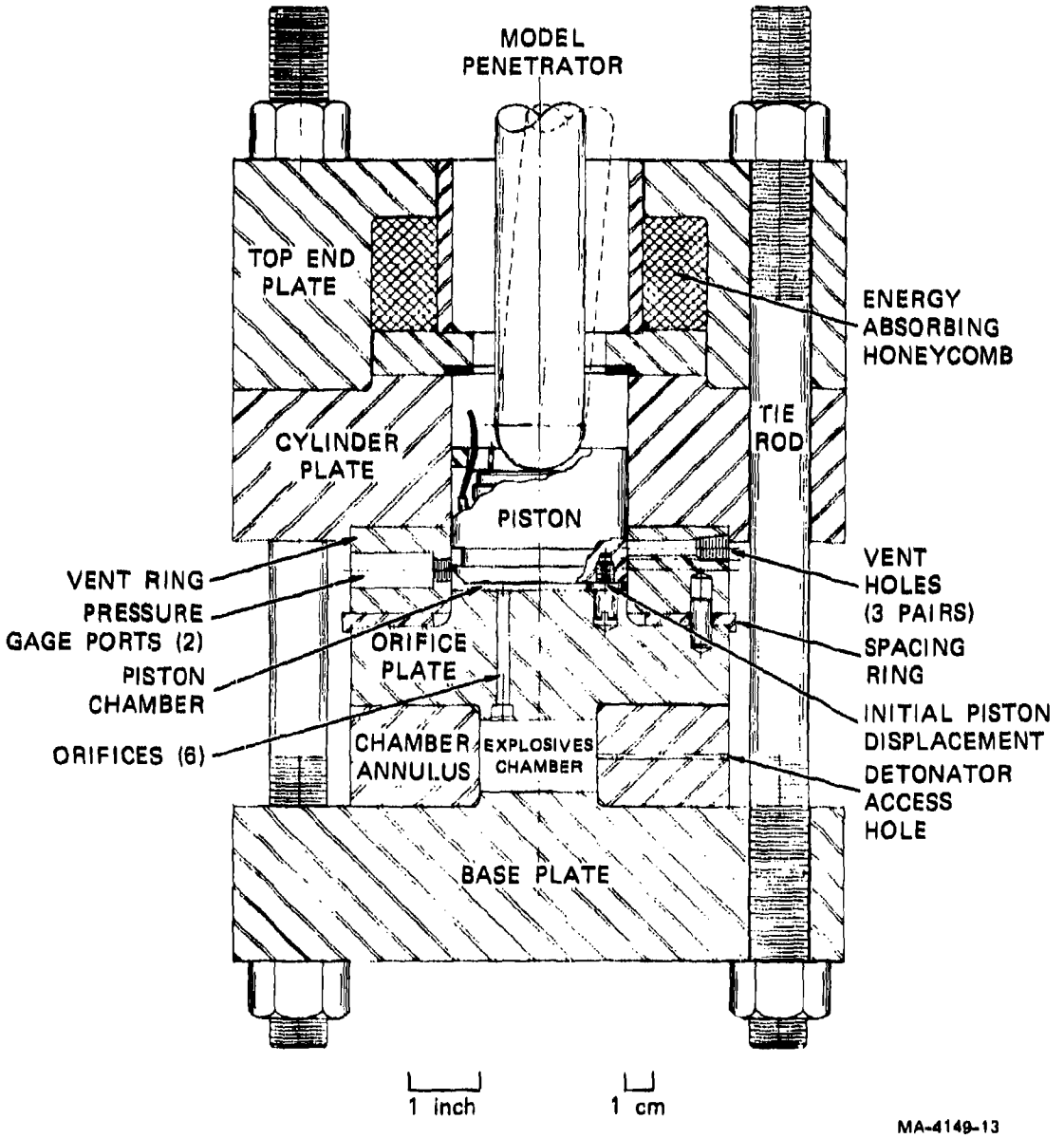

FIGURE 3 ASSEMBLY DRAWING OF TEST FIXTURE FOR SIMULATING IMPACT LOADS

All the model structures tested have a 1.50-inch (3.81-cm) outer diameter and a hemispherical front end, rather than a pointed nose, to allow the desired load to be applied more easily and accurately. The model typical of deep earth penetrator structures (thick-walled model) is made of AISI 1020 steel, is 9 inches (22.9 cm) long, and has a 0.875-inch-diameter (2.22-cm-diameter) cylindrical cavity over the aft two-thirds of its length. Each model is instrumented with eight axial strain gages, four at the front station about 2 inches from the nose and four at the aft station at about the midlength. At each station the gages are uniformly spaced around the circumference and oriented so that the gages measure only strain in the axial direction.

Figure 4 shows the load cell and strain records from Test 64 of the thick-walled model. The initial angle of tilt θ was 19°30' (0.340 rad). In this test the peak load, Figure 3(a), was 15,000 pounds (66.7 kN). The peak axial compressive strain, Gages 5 and 7, Figure 3(b), was 0.022 percent. The bending strain reduced the strain at Gage 6 but added to the strain at Gage 8 to produce a peak compressive strain of about 0.042 percent. This bending response is similar to that observed in angle-of-attack reverse ballistics tests performed by AVCO.[5] At higher load levels, yielding would first occur in the vicinity of Gage 8, followed by a reduction in bending stiffness, buckling, and fracture of the penetrator structure.

These and other test results show that the load simulator can apply to model penetrators loads similar to those occurring in angle-of-attack impacts. The structural response of the penetrator has been accurately measured, using hard-wired strain gages. The tests indicate that the loader could also be built in a larger size to test full-scale penetrators.

ANALYSIS OF PENETRATOR RESPONSE

In the analysis, the central portion of the penetrator is modeled by elastic Timoshenko beam theory including thrust. This formulation includes the two dominant response mechanisms governing angle-of-attack

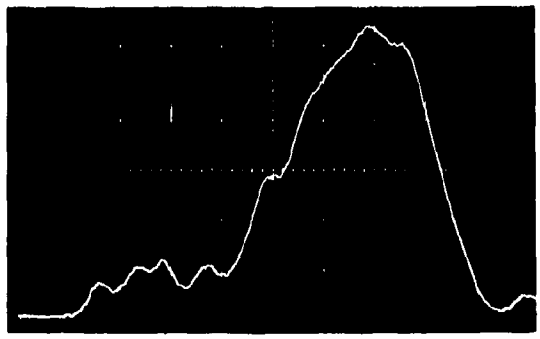

(a) LOAD CELL RECORD
[2500 lbs/cm (11.1 kN/cm) 50 μsec/cm
150 μsec delay]

GAGE 5 (ϵ_{axial})

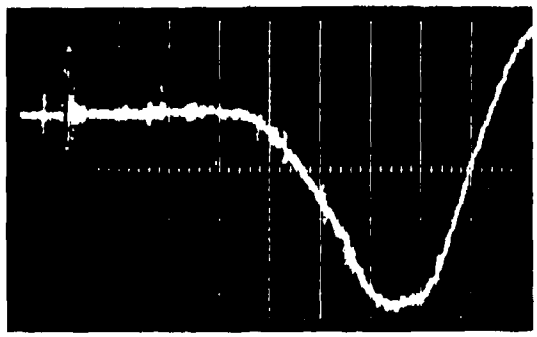

GAGE 8 ($\epsilon_{axial} + \epsilon_{bending}$)

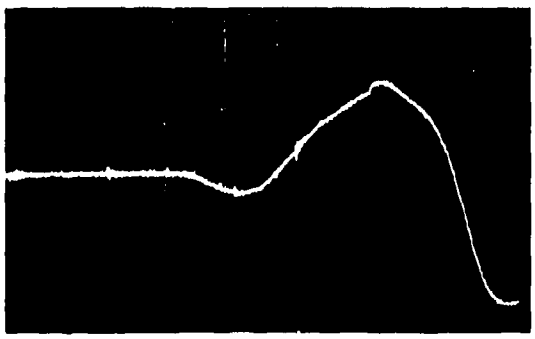

GAGE 6 ($\epsilon_{axial} - \epsilon_{bending}$)

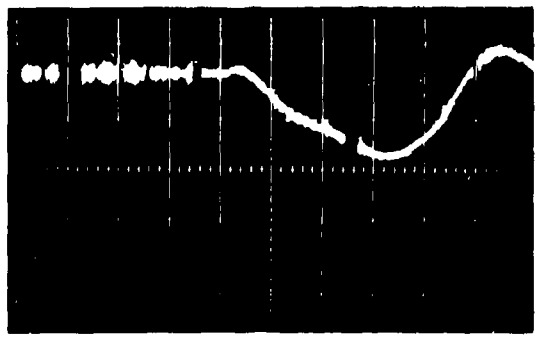

GAGE 7 (ϵ_{axial})

(b) STRAIN GAGE RECORDS FROM AFT STATION
(0.016%/cm, 50 μsec/cm, 150 μsec delay)

MA-3091-137A

FIGURE 4 TEST 64–19°30′ (0.340 rad) ANGULAR LOADING OF THICK-WALLED MODEL

impacts: axial compression and bending under lateral loads. The front portion of the solid nose and the solid aft end are modeled as rigid masses. Loading of this structure is specified by the magnitude, time history, and orientation of a resultant impact force through a fixed point in the front mass.

The response predicted by the analysis was first compared with the penetrator strains measured in the simulator experiments. The measured loads were used as input for the analyses. To account for the small uncertainty in the point of application of the resultant loading force in the simulator experiments (due to deformation of the face of the loading piston), upper and lower bounds on the response were calculated for extreme locations of the point of load application for each experiment. Thus, these comparisons not only provided a check on the analysis, but also aided in the understanding of the simulator loading technique.

For the thick-walled penetrator of Test 64, Figure 5 shows the upper and lower bounds on calculated strains along with the strain measured at strain Gage 8. The error bands on each of the predicted strains correspond to the uncertainty in the horizontal force and in the angle of inclination. The total strain calculated for the two extreme points of load application bound the initial peak measured in the experiment.

The analysis was then used to investigate the effects of the ratio of lateral to axial load, pulse shape, rise time, end masses, and lateral payload inertia. We discuss here only the effect of rise time. This effect was studied by applying loads with the different rise times shown in Figure 6(a) and with a ratio of lateral to axial load of 0.2. As discussed in Section 5, this corresponds to an angle of attack of about 3.8 degrees. The structure was a simple steel tube with length-to-diameter ratio $\ell/d = 6$ and radius-to-thickness ratio $a/h = 4$.

The bending and axial stress histories at Station $\xi = x/\ell = 0.4828$, normalized with respect to the normal stress σ_s at the loaded end of the tube are shown in Figure 6(b).

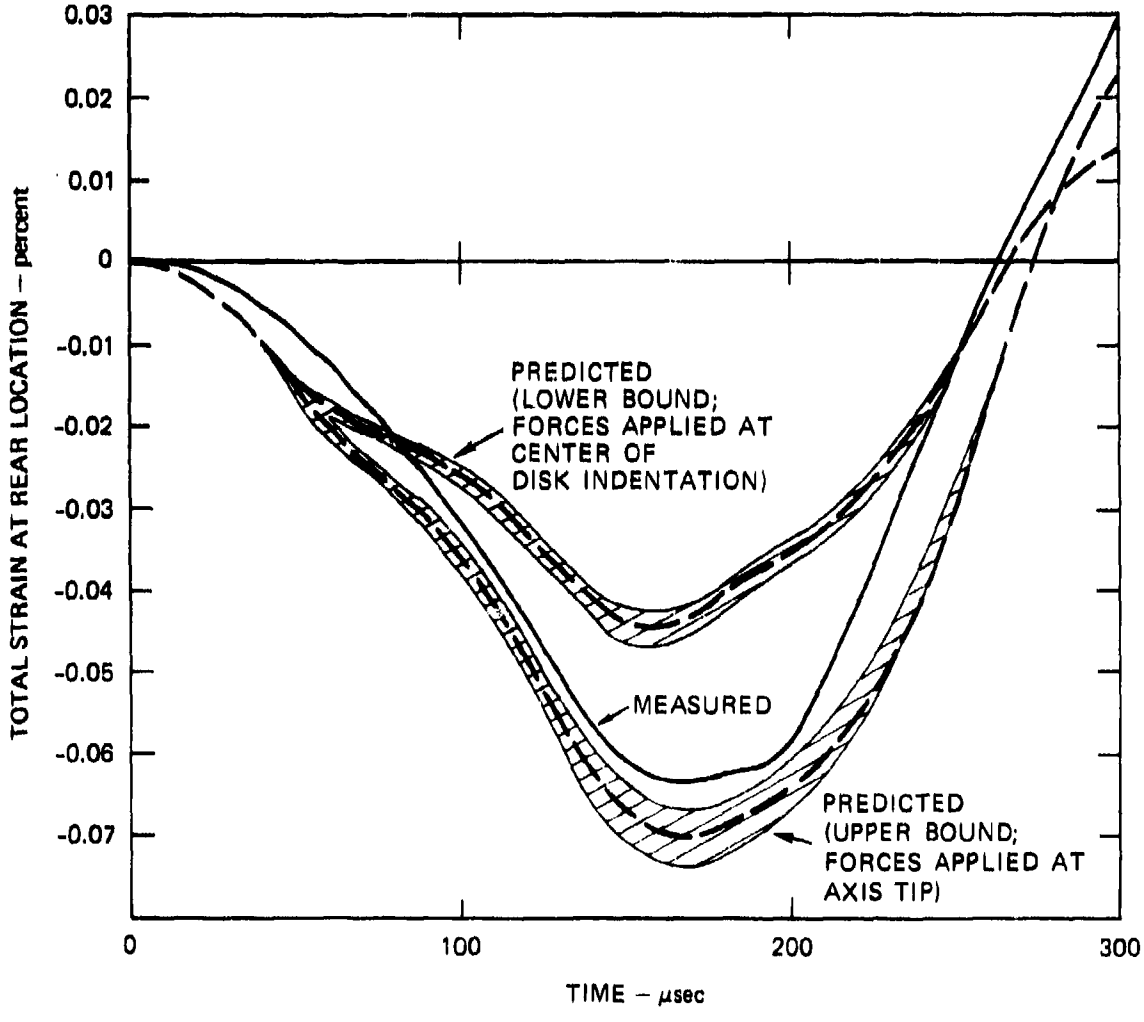

FIGURE 5 PREDICTED STRAINS AND MEASURED STRAIN IN SIMULATOR EXPERIMENT 64 (THICK-WALLED STRUCTURE)

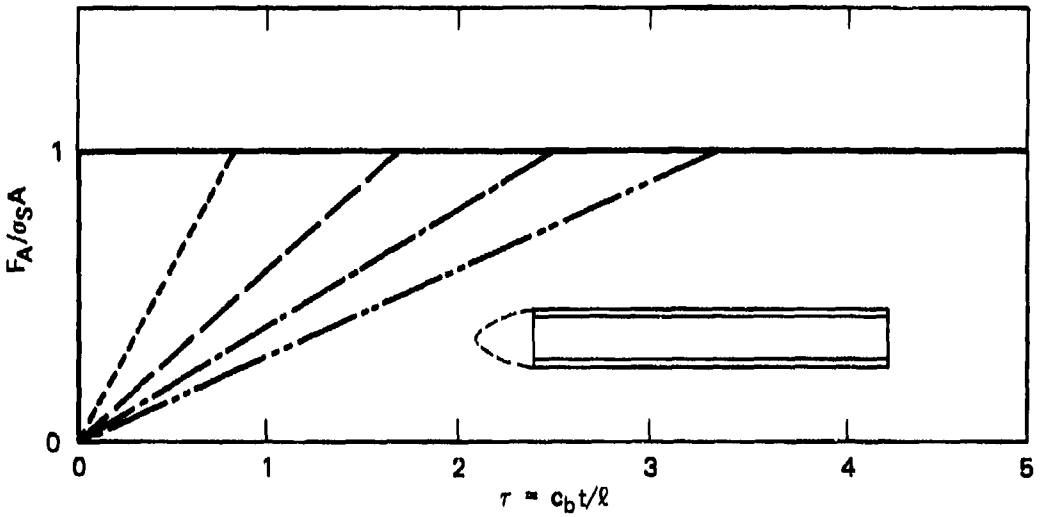

(a) AXIAL LOADING FORCE, F_A VERSUS TIME (η = 0.20)

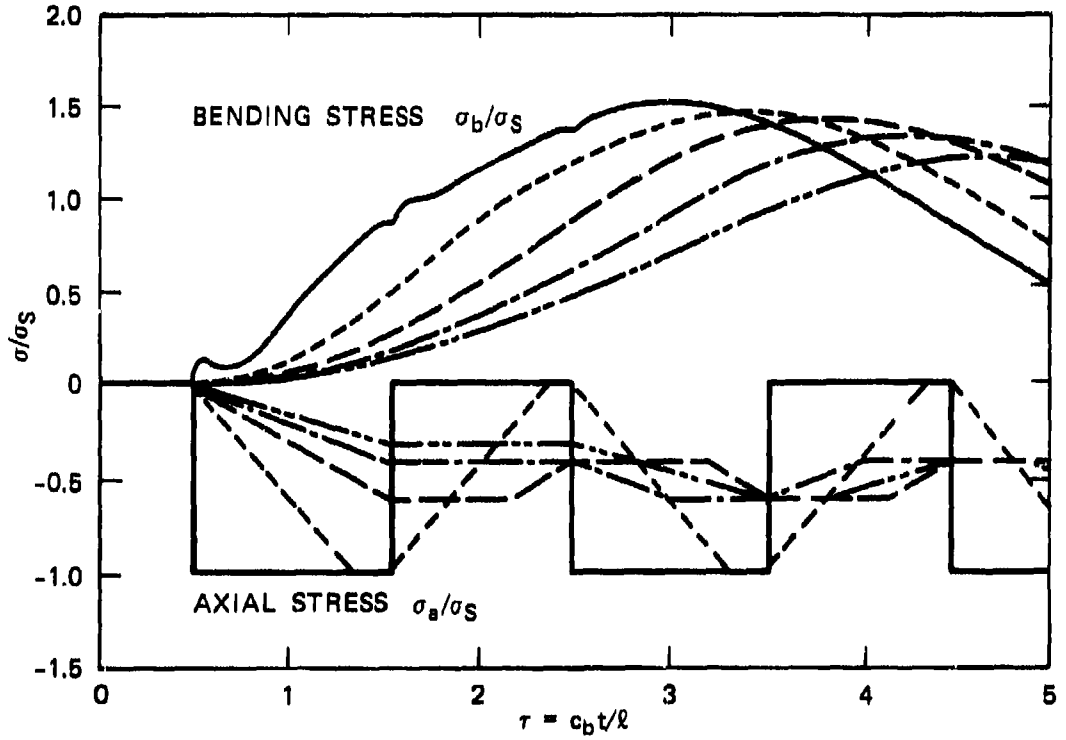

(b) STRESS VERSUS TIME AT $\chi = x/L = 0.4828$

MA-3091-121A

FIGURE 6 RESPONSE OF A SIMPLE STEEL TUBE TO LOADS WITH DIFFERENT RISE TIMES (ℓ/d = 6, a/h = 4)

The largest bending stress ($\sigma_b/\sigma_s = \pm 1.51$) is produced by the loading of zero rise time (step input). In order of increasing loading rise times, the peak bending stresses σ_b/σ_s produced are 1.48, 1.40, 1.31, and 1.20. As the rise time increases further, the peak stress at this location approaches the steady-state value of $\sigma_b/\sigma_s = 0.793$. Furthermore, the time at which the peak occurs increases with rise time.

For the axial stress, the peak stress at a given location is determined by whether the loading rise time is less than or greater than the time at which a reflected tensile stress wave from the aft free end arrives at the location. For loading curves with rise times of less than one transit time, the maximum axial stress produced is $\sigma_a/\sigma_s = -1.00$. For the loading curves with rise times of more than one transit time, the maximum stress is $\sigma_a/\sigma_s = -0.617$. The steady-state value at this location is $\sigma_a/\sigma_s = -0.517$.

Thus, we conclude that the largest effects due to increasing the loading rise time are the increase in the times at which peak bending occurs and the variation in axial stress for loading rise times near one transit time. The variation in loading rise time has less effect on the peak bending stress and on the peak axial stress for rise times larger than two transit times.

CRITICAL IMPACT CURVES

In this section we apply the analysis to some of the penetrator structures of interest. These structures range from deep penetrators (large ℓ/d, small a/h) to shallow penetrators (small ℓ/d, large a/h). Calculations were also made for penetrators with intermediate values of ℓ/d and a/h so that we could see how these ratios affect response.

For design purposes the most useful information is the relationship between the impact parameters and the response parameters. This relationship can be used to make design tradeoffs between the penetrator structure and the impact conditions. For example, for a given penetrator and a given target, a tradeoff can be made between impact velocity and angle of attack.

This impact-response relationship, including both terradynamics and structural response, is complex and not understood for many impact conditions. However, some insight can be gained by introducing an appropriate set of parameters that describe the loading on the penetrator. The impact-load relationship (determined only from terradynamics) and the load-response relationship (determined entirely by structural response) can be treated separately and combined to produce the impact-response relationship sought.

The load-damage relationship can be determined readily using the analysis described above; such a relationship for a simple tube was shown in Figure 6. In contrast, the terradynamic impact-load relationship is not as well understood. Therefore, we make two reasonable assumptions, based on currently available information, to obtain an impact-load relationship that allows this procedure to be illustrated and shows the nature of the impact-response relationship. From available theoretical and experimental results, we first make the approximation that the axial loading force F is proportional to the impact velocity V. For normal impacts this relationship has been verified for soil targets and also appears to hold for rock targets.* Second, we assume that the lateral load is proportional† to the angle of attack α, over the range of α of interest. This assumption is consistent with a comparison between predicted strain and strain measured in angle-of-attack reverse ballistics tests performed by AVCO.

With this impact-load relationship we transform the load-response relationship into the critical impact curves shown in Figure 1 for four penetrator structures. These curves are plots of combinations of impact velocity V and angle of attack α for which the peak compressive stress in the penetrator is constant. Thus, the curves give the tradeoff between impact velocity and angle of attack. The specific curves drawn

*P. F. Hadala, private communication, January 1977.

†More precisely, we assume that $\tan^{-1}\eta = 3\alpha$ where $\eta = F_L/F_A$, as discussed in Section 5.

assume that the critical stress σ_{max} is ten times the "pressure" $P_{1000} = F_{1000}/A$ at a 1000 fps (305 m/sec) normal impact. Structure B is similar to that already used for deep penetration into hard targets. Structure C is similar to that proposed for shallow penetration. Structures A and D were analyzed to show the effects of changing ℓ/d or a/h.

The critical impact curves can be used to select the penetrator material, on the basis of yield stress, for a given range of V and α within which the penetrator must function. For example, if for Structure B and a given target, the maximum impact velocity is to be 2000 ft/sec and the maximum angle of attack is to be 3 degrees, a material with a yield strength of at least 10 P_{1000} is needed. In a similar way the critical load curves could be used to select targets for which a given system (i.e., specified σ_y, V, and α) could be used.

Critical impact curves can also be used to interpret results of experiments of more detailed load and structural response calculations (e.g., a finite element code prediction). A particular experiment or detailed calculation gives a single point on a critical impact curve. Although such a data point is probably more accurate than the curves calculated with the beam-mass model used here, more points are needed to determine the shape of the curve. The curves calculated with the beam-mass model can be used to determine this shape. Thus the appropriate values of V and α can be selected to minimize the data points needed to define the curve. For example, for Structure B small increments in α and larger increments in V should be made to efficiently define the $\sigma_{max}/P_{1000} = 10$ curve for small α.

The critical load curves are perhaps most useful for making design tradeoffs among candidate penetrator structures. For example, the curves for Structure B (deep penetrator) and for Structure C (Shallow penetrator) pass through a similar region in the V-α plane and intersect at $V = 1500$ ft/sec and $\alpha = 5.7$ degrees. However, the curve for Structure B is steeper and, for small angles of attack, this structure can withstand greater impact velocities. Both these penetrators can be

made stronger by increasing only the wall thickness (from that of Structure C to that of Structure A) or decreasing the length (from that of Structure B to that of Structure A). Note that either of these changes reduces the payload volume. Also, for small angles of attack, the velocity range can be extended more by increasing wall thickness than by decreasing length. Similar conclusions can be drawn by comparing curves for Structures B and C with that of Structure D.

The method developed here for characterizing the strength of penetrator structures has been applied to four idealized structures. The principal advantage of this procedure is that it characterizes the response over a range of impact conditions. It can be applied to more complex structures than those analyzed here to plan and interpret experiments and detailed calculations and to compare the performance of different structures for a particular application.

REPORT ORGANIZATION

The remainder of this report is divided into four sections. Section 3 describes the experiments on 1/4-scale model penetrator-like structures and the measured response. Section 4 presents the development of the mathematical analysis, comparison of predicted response with measured response, and the effect of certain parameters, such as loading rise time, on the predicted response. Section 5 presents critical impact curves, that is, combinations of impact velocity and angle of attack that produce the same peak stress in a given structure. Structures analyzed have radius-to-thickness ratios ranging from 2.0 to 10.0 and length-to-diameter ratios ranging from 3.6 to 8.0.

3. SIMULATOR EXPERIMENTS

The primary objective of the experimental work described here was to evaluate a concept for economical testing of penetrator structures. To make such an evaluation the test fixture was designed for loading nominal 1/4-scale model penetrators; the resulting design can be fabricated in full scale for testing actual penetrator structures. A secondary objective was to provide experimental data for comparison with the analysis.

The load simulator design is based on two basic principles. First, damage to the penetrator occurs during or shortly after the load reaches its peak amplitude; therefore, only this portion of the load history need be simulated. The change in momentum of the penetrator during this time is small compared to the total momentum of a penetrator on impact. Therefore by applying only this early time portion of the load to a penetrator initially at rest, the response of interest is simulated but the resulting momentum transmitted to the structure is much less than the initial momentum required in ballistic or reverse ballistic tests. This allows simulator tests to be performed in the laboratory. Second, observed maximum compressive strains and failures in penetrator structures occur at distances greater than one diameter from the penetrator nose. The stress distribution over the cross section at these locations depends only on the resultant forces applied to the end of the structure. Thus the load simulator was designed to produce the resultant axial and lateral loading forces with the appropriate time-history, and not the details of the pressure load distribution on the penetrator nose.

The remainder of this section covers three aspects of the load simulation tests: the design and construction of the test fixture, the 1/4-scale model structures that were tested, and some typical results of the tests.

TEST FIXTURE

Operation

Figure 7 is a sectioned assembly drawing of the fixture in configuration for simulating normal impact loads on 1/4-scale model penetrators. The fixture operates as follows: high-pressure gaseous explosive products are produced in the explosive chamber by detonation of a solid explosive. The gas flows through an orifice plate and into a cylinder containing a piston that is in contact with the penetrator. The load is transmitted to the penetrator through the piston (the details of this interface are discussed later). The fixture was designed so that the rise time of the pressure load could be varied by using different initial piston displacements or different orifice areas. The duration of the nearly constant load plateau can be varied by using vent holes at different locations along the cylinder, and the decay time can be varied by using different size vent holes.

To aid in the design of the fixture, the pulse produced by a given geometry was predicted by using the GASLEAK computer code,[8] which models the flow of gases in a series of chambers connected by orifices. The theoretical model of the flow assumes that (1) the duration of the loading pulse is long compared with the transit time of pressure waves in each chamber (quasi-steady flow), (2) negligible heat is transferred from the hot gas to the surrounding cylinder (adiabatic flow), and (3) the hot detonation products behave as a perfect gas. Experience in other similar applications has shown excellent agreement between the theorteically predicted pressure pulse and the experimentally measured pulse.

Construction

The device is constructed on a stack of alloy steel rings and circular plates clamped together by eight tie rods. The explosive chamber is formed by a thick annulus that fits between the base plate and the orifice plate. The cross-sectional area of each of the six

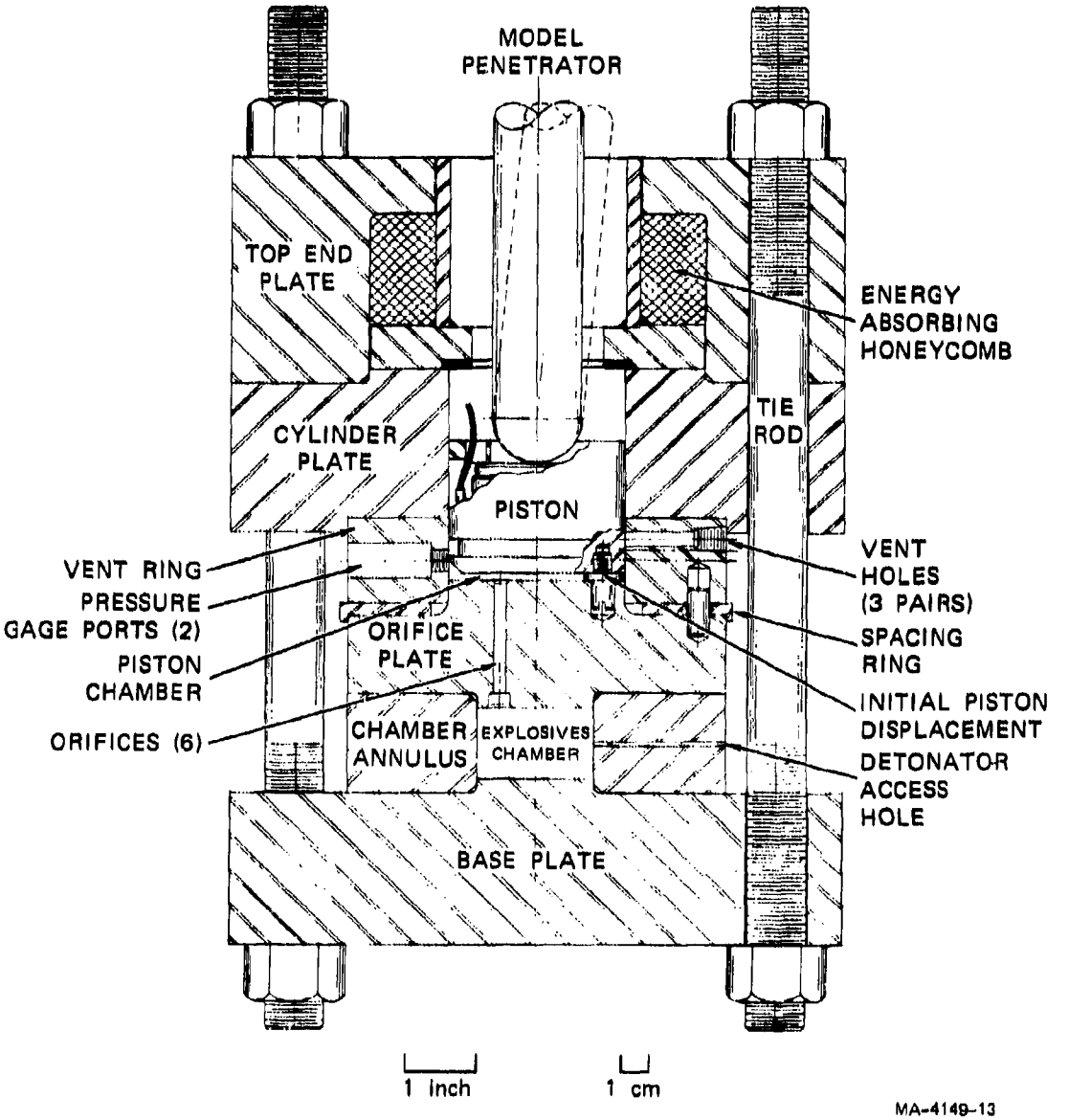

FIGURE 7 ASSEMBLY DRAWING OF TEST FIXTURE FOR SIMULATING IMPACT LOADS

orifices may be varied by inserting plugs drilled with the proper size hole into the recesses on the lower side of the orifice plate. The cylinder in which the piston travels is formed by the vent ring and the cylinder plate. The initial volume of the piston chamber is controlled by a spacing washer between the piston and orifice plate, which sets the initial piston displacement.

The vent ring has three pairs of vent holes, each pair at a different axial location. These holes vent the piston chamber to the atmosphere as the piston passes. The size of the vent area may be varied with threaded plugs that reduce the area of the vent holes or close the holes completely. The axial location of the holes is set by the thickness of the spacing ring. Two pressure gages are mounted diametrically opposed in the vent ring to measure the chamber pressure. After the pulse is produced, the piston decelerates by impacting the energy-absorbing aluminum honeycomb.

Experimental Setup

To simulate the load on a penetrator that impacts at an angle of attack, the piston is designed to produce a combined axial and lateral loading and to measure the load applied to the penetrator. The combined loading is produced by tilting the penetrator through an angle θ with respect to the piston axis, as shown in the sectioned drawing of the piston in Figure 8. The angle θ may be varied from zero to 20° (0.35 rad). As discussed in Section 3, this corresponds to an angle of attack of about 3.7 degrees. In structural response tests, the vertical force F_v is measured with a piezoelectric load cell* (Kistler 906A). Two discs are placed between the penetrator and the load cell, and the interface between the discs is lubricated with a

*As discussed later, a load cell was not used in the long-rod calibration tests.

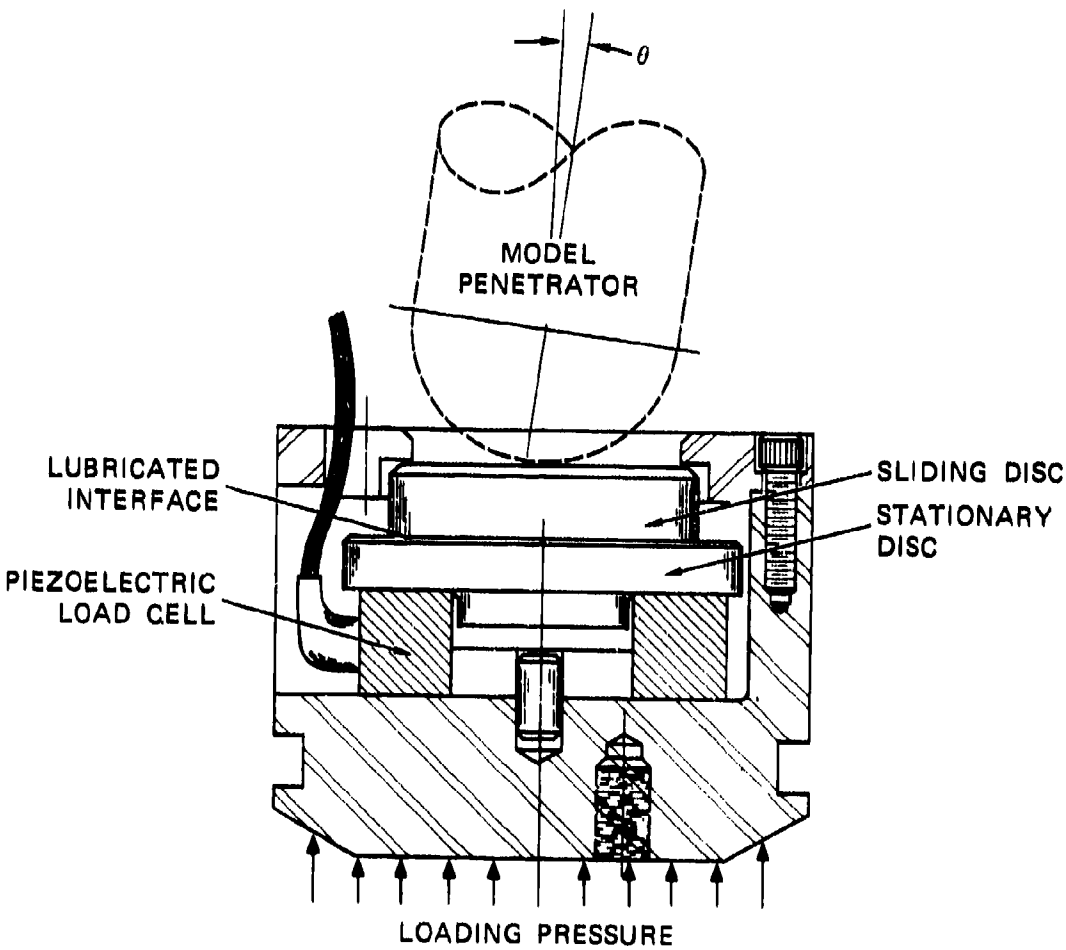

FIGURE 8 PISTON FOR ANGULAR LOADING

high-pressure solid lubricant (Dow Corning Molykote 321R) to minimize the horizontal frictional force.* When the load is applied, sliding occurs between the two discs, and the vertical force F_V and a horizontal frictional force F_H are applied to the penetrator.

The ratio of the applied loads F_H/F_V can be determined from the motion of the penetrator. With the assumption that this ratio is constant during application of the loading,† the load ratio is related to the angle β between the path of the center of mass of the penetrator and the vertical axis of the simulator as follows:

$$\frac{F_H}{F_V} = \tan \beta$$

The angle β was measured using high speed photography; the largest value of β measured was about 9 degrees. Figure 9 shows the assembled device with a 1/4-scale model penetrator in position for a normal impact simulation. Before the experiment, the model is held in place by low-strength, machined Styrofoam rings that fit inside the top end plate and the cylinder plate. In angular impact tests, the initial angle θ between the axis of the penetrator and the axis of the simulator is measured with a vernier protractor. After the load simulation, the penetrator leaves the device and is stopped by an external energy absorber (aluminum honeycomb or Styrofoam) located in a 5-foot-long (1.52-m-long) safety shroud. The shroud ensures containment of the model penetrator after the simulation. Figure 10 shows the device with the safety shroud in place for testing.

---

*For impact at an angle of attack, the component of the friction force lateral to the penetrator acts in the opposite direction from the lateral force we wish to simulate.

†This assumption was examined in a series of tests in which the load duration was shortened by means of a mechanical stop placed above the piston. The tests indicate that the load ratio variation during the impact simulation is within measurement error.

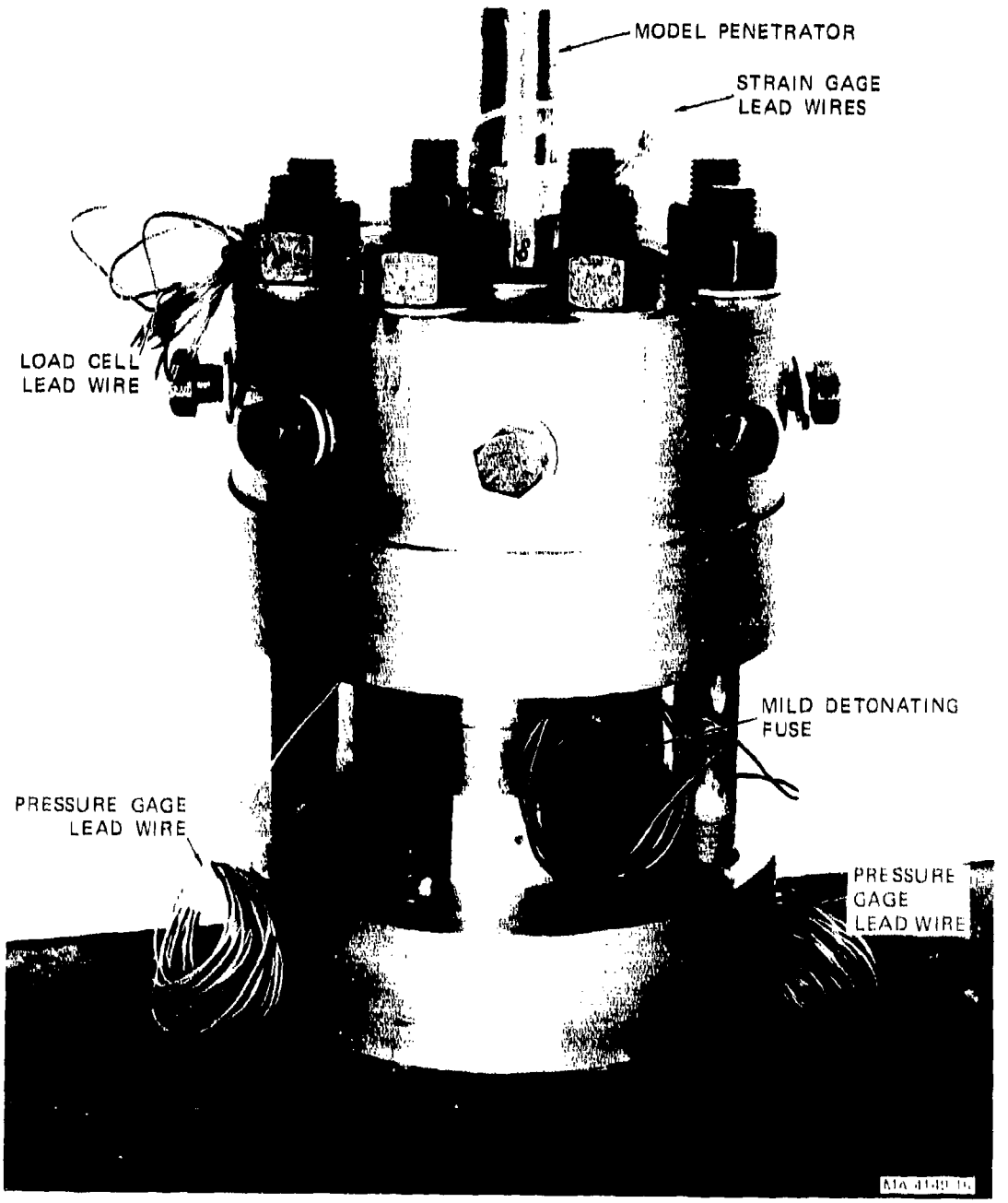

FIGURE 9 ASSEMBLED TEST FIXTURE FOR SIMULATING IMPACT LOADS

In some experiments high speed movies were taken to measure the angle β. In these experiments the camera (Hycam Model 410004) was placed 3 feet (91 cm) from the simulator and photographed 12 inches (30 cm) of penetrator travel at the nominal rate of 10,000 frames per second (a safety shroud that allows a large field of view was used rather than the shroud shown in Figure 10). The center of mass of the penetrator was marked with a bullseye to allow its path to be photographed after the load simulation. To provide a reference for tracing the motion of the model penetrator, a grid was placed on the top of the simulator, filmed, and removed before the experiment.

After the experiment the motion of the center of mass of the model was determined by using a Telereadex film analyzer. A frame of the film showing the reference grid was first projected onto a table and traced onto a sheet of paper. Subsequent frames were projected onto the traced grid. The position of the center of mass in several frames was marked on the grid. Typically, the path of motion was about 15 inches (38 cm) long on the projection screen. The tangent of the angle β between the path of the center of mass and a vertical grid line was then measured directly. Accuracy of measurement was about ± 0.01 radians.

MODEL STRUCTURES

Two general types of structures were used in the experiments. First, we used a calibration rod long enough that waves reflected from its free end did not reach the piston during the load rise time. Then, we tested several shorter structures typical of penetrators.

Calibration Rod

In the calibration experiments (Tests 12 through 30) we used an AISI-1020 steel rod 1.5 inches (3.81 cm) in diameter and 30 inches (76.2 cm) long. To simulate a normal impact, we placed this long rod perpendicular to the top face of the piston with the rod-piston interface conditions shown in Figure 11(a). The 3/4-inch-diameter (1.90-cm-diameter) steel disc applied the load to the central area of the rod so that any

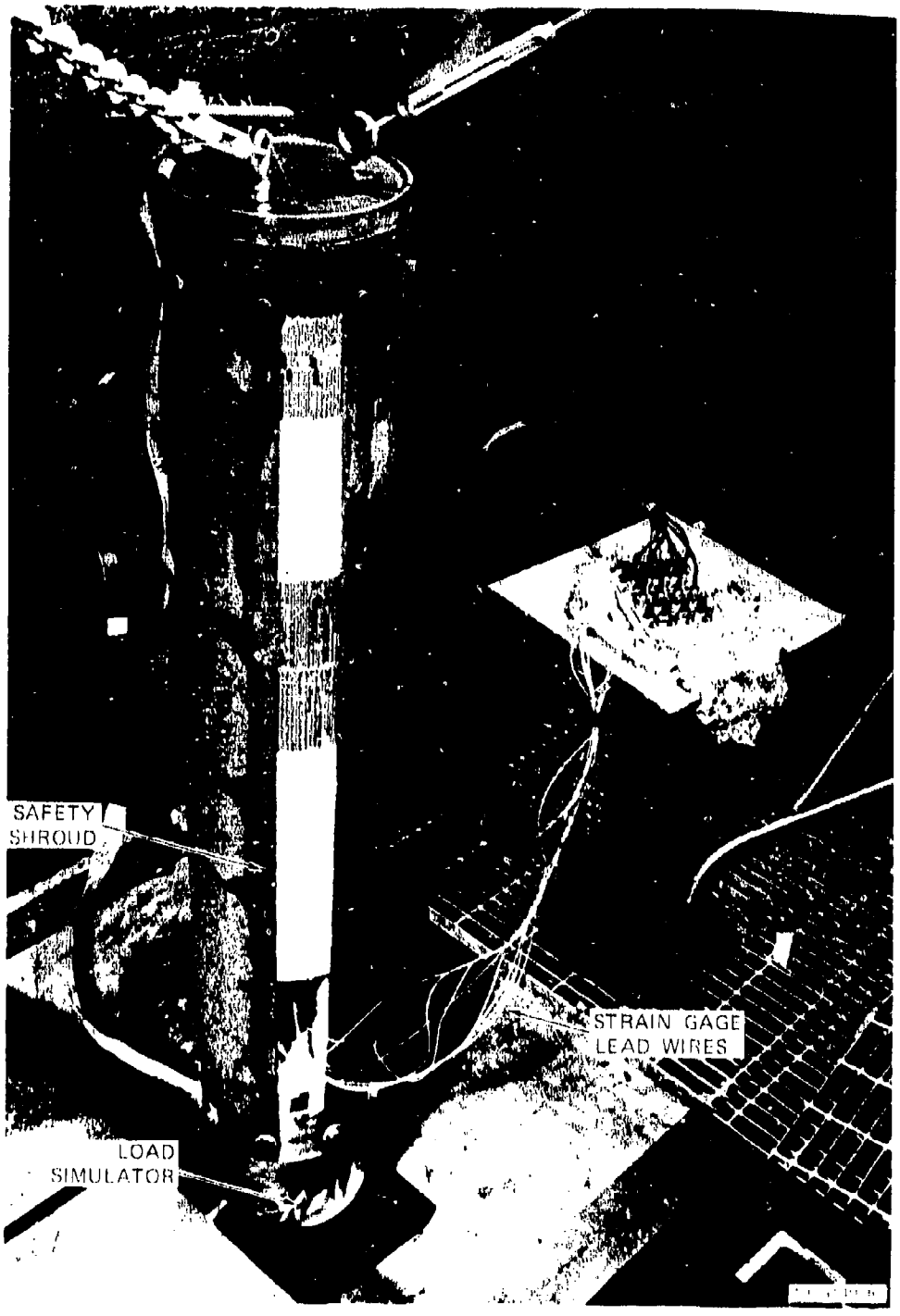

FIGURE 10 FIXTURE READY FOR TESTING

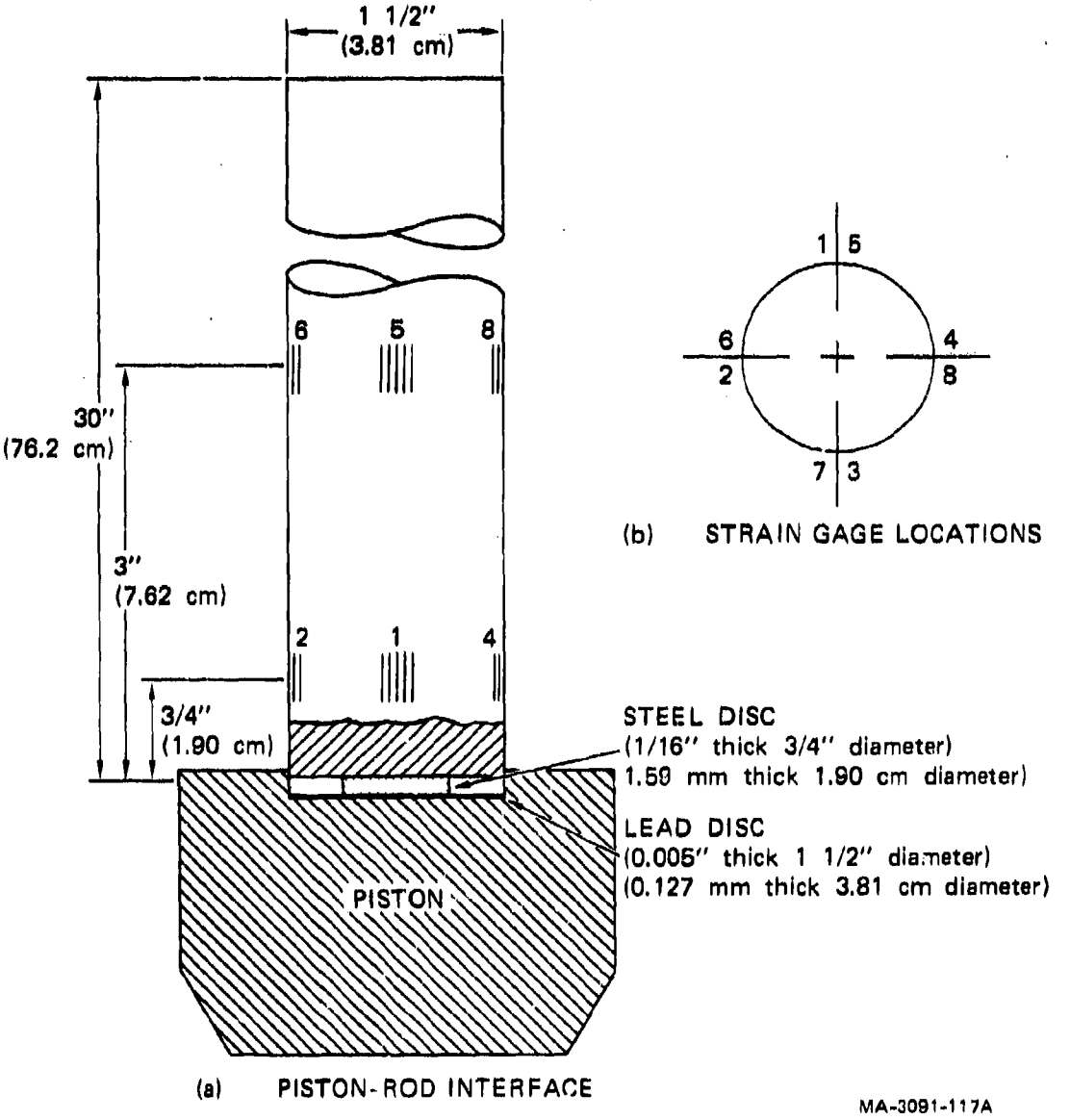

FIGURE 11 LOADING CONFIGURATION FOR LONG ROD

eccentricity of the loading would be reduced. The lead sheet smoothed any surface irregularities. Strain measured near the front end of the long rod was used as a check on the load.

The calibration rod is instrumented with eight strain gages (Micro-Measurements Type EP-08-250GB-120) to measure the rod strain in the axial direction. The locations of the gages are shown in Figure 11(b). The four gages at each axial station are evenly spaced around the rod.

Penetrator Models

Figure 12 is a general schematic drawing of four of the penetrator models used in the experiments. The models have a 1.50-inch (3.81-cm) outer diameter and have a hemispherical front end rather than a pointed nose to allow the desired load to be applied more easily and accurately. Each model is instrumented with eight strain gages to measure strain in the axial direction. The details of each model are given in Table 1.

The solid steel model is 9 inches (22.9 cm) long and is made of AISI 1020 steel. It is the simplest model since it has a uniform cross section (except at the loaded hemispherical end). The solid aluminum model is geometrically identical to the solid steel model but is made of 6061-T6 aluminum. It was only used to check the behavior of the piston sliding plate when a lightweight model was tested.

Two of the models have cavities (indicated by the dashed lines in Figure 12). Both are made of AISI 1020 steel. The thick-walled model is 9 inches (22.9 cm) long with a 0.875-inch-diameter (2.22-cm-diameter) and a 6-inch-long (15.24-cm-long) cylindrical cavity. The radius-to-thickness ratio of the cylindrical portion of this model is typical of deep earth penetrator structures. The thin-walled model is 6.625 inches (16.8 cm) long with a 1.305-inch-diameter (3.43-cm-diameter) and a 4.7-inch-long (11.94-cm-long) cavity. The radius-to-thickness ratio of this model is typical of proposed shallow penetrator structures.

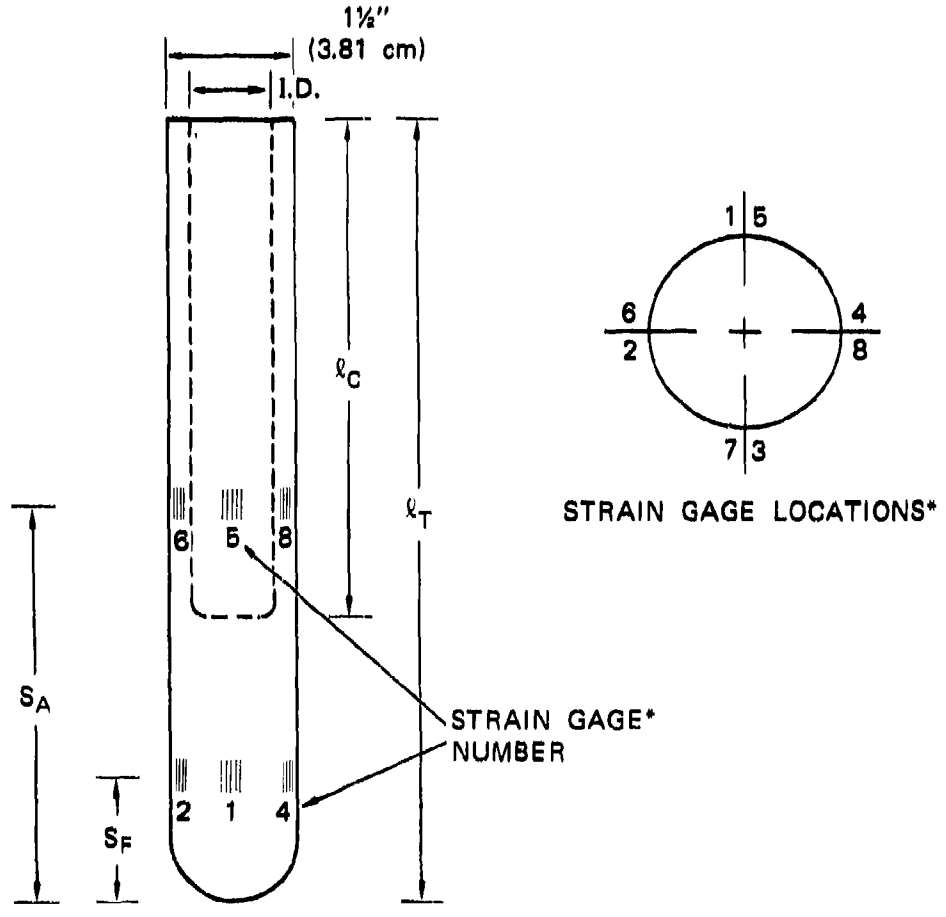

*On the solid steel model the positions of gages 2 and 6 are interchanged with those of gages 4 and 8.

MA-3091-131A

FIGURE 12 MODEL PENETRATOR WITH CAVITY

Table 1

MODEL PENETRATOR STRUCTURES

Model	Abbr.	Mass (gm)	Length [ℓ_T][a] (cm)	Cavity Length [ℓ_c] (cm)	Cavity Diam. [I.D.] (cm)	Strain Gage Locations[b] Front [S_F] (cm)	Strain Gage Locations[b] Aft [S_A] (cm)
Solid 1020 steel	SS	2030	22.86	--	--	3.81	11.43
Thick-walled 1020 steel	TkW	1535	22.86	15.24	2.22	3.81	11.43
Thin-walled 1020 steel	TnW	620	16.83	11.94	3.43	6.10	10.45
Solid 6061-T6 aluminum	SAl	683	22.86	--	--	--	--
Tapered 6061-T6 aluminum	TAl	759	19.05	--	--	5.08	9.53

[a] Letters in brackets refer to schematic drawing of model penetrator in Figure 12.

[b] Distance measured from front of model structure.

In four tests a tapered solid aluminum model was used to provide data for future analysis of tapered structures. The loaded end is a 1.50-inch-diameter (3.81-cm-diameter) hemisphere similar to the other models. The body tapers outward to 1.875-inch-diameter (4.76-cm-diameter) at the aft end. The overall length is 7.50 inches (19.0 cm).

EXPERIMENTAL RESULTS

The details of each test and the responses measured are given in Appendix A (Tables A-1 through A-4). The strain responses measured in Tests 64 and 66 are compared with the predicted responses in Section 4.

The test results reflect the development and refinement of the simulation technique. For example, initial tests with the long rod indicated that any slight deviation in the perpendicularity of the rod and the piston face caused the load to be applied eccentrically at the edge of the rod. This effect varied from test to test, causing irregular bending strains. A small-diameter interface disc was placed between the rod and the piston to reduce this effect. Although this reduced the bending, significant undesired bending strains still occurred. The problem was resolved in the later models by using a hemispherical loaded end. Other parts of the simulation technique added during the test program included: a load cell for measuring the applied vertical load and high speed photography for determining the ratio of the applied horizontal force to the applied vertical force.

In the tests with angular loading, two opposing strain gages at each of the two stations were aligned in the plane of bending. The other two gages at each station were in the neutral plane in which no bending occurs. In the figures that follow, the four gages from each station are grouped together as indicated in Figure 4: the strain gage record from each station that contains the compressive side of bending is displayed in the upper right-hand corner of the group of four records from that station. The gage record containing the tensile side of bending is in the lower left-hand corner of the group. The other two records in each group show only the axial strain. (Note

that the gage numbers of the gages in the bending plane varied from test to test.) When all eight strain gage records are shown, the front station is the top group of four, and the aft station is the lower group.

Long Rod

Figure 13 shows the chamber pressure and front station strain records from Test 16. In this test the long calibration rod was loaded axially. The nonuniformity of the strains due to the eccentrically applied load discussed previously can be seen by comparing the magnitudes and shapes of the four strain records. The average peak strain of 0.020 percent corresponds to an axial force of 10,600 pounds (47.1 kN). The peak pressure corresponds to an axial force of 11,300 pounds (50.3 kN). The difference in the two force levels is caused by the inertia of the piston.

Solid Steel Model

Figure 14 shows the pressure, load cell, and strain gage data recorded in Test 37 in which the 9-inch-long (22.9-cm-long) solid steel model was normal to the piston face. The results of this test show several characteristics typical of the model tests. As the load is applied to the model, the hemispherical end indents the sliding disc on the piston, causing plastic deformation of the disc. This deformation and the inertia of the piston account for the difference between the rise time shown on the pressure record and that shown on the load cell record. The load cell record shows that the load rises, gradually levels, and then drops off. The simulation load comprises the load rise and leveling off and ends as the load begins to drop. As will be discussed in Section 4, the peak penetrator response occurs shortly after the load reaches its peak; therefore, the duration of the simulation is adequate. The uniformity of the axial strain at each station is attributed to the hemispherical end. This test and similar ones show that the circumferential variation in measured strain due to axial loads is about 3 percent.

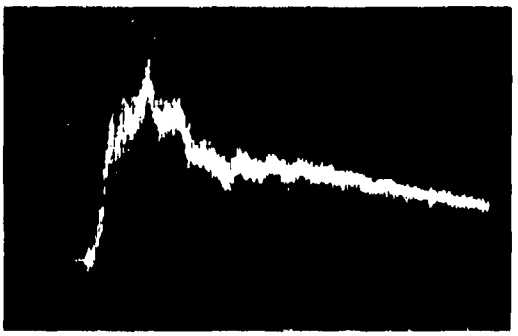

400 psi/cm (2758 kPa/cm) 200 μsec/cm

(a) PRESSURE RECORD (GAGE 1)

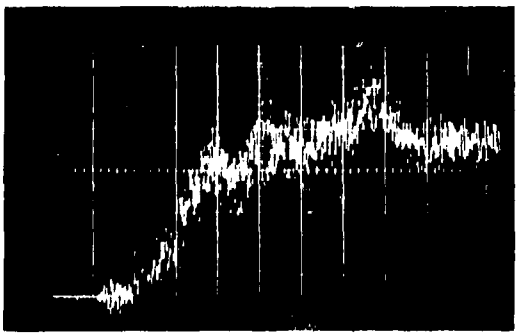

400 psi/cm (2758 kPa/cm) 50 μsec/cm

(b) PRESSURE RECORD (GAGE 1)

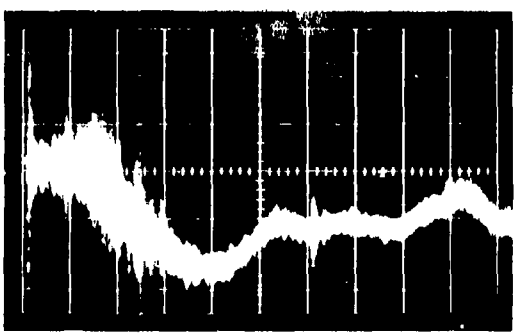

GAGE 1

0.0079%/cm 100 μsec/cm

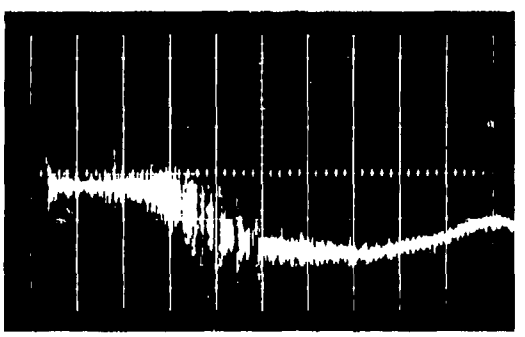

GAGE 4

0.0079%/cm 50 μsec/cm

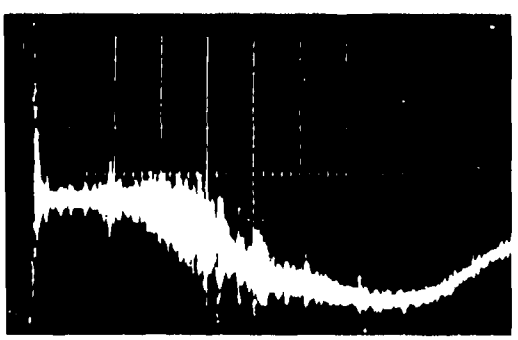

GAGE 2

0.0079%/cm 50 μsec/cm

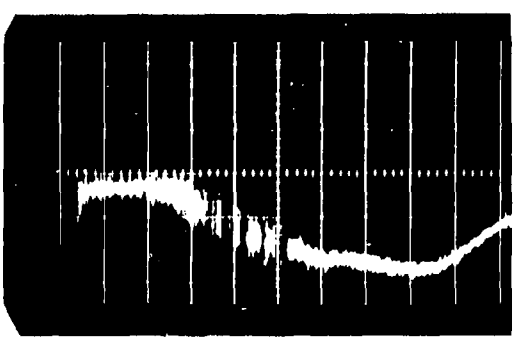

GAGE 3

0.0079%/cm 50 μsec/cm

(c) STRAIN GAGE RECORDS FROM FRONT STATION

MP-3091-118A1

FIGURE 13 TEST 16—CALIBRATION TEST WITH LONG ROD

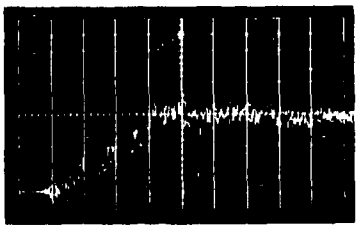

1000 psi/cm (6894 kPa/cm)
50 μsec/cm 100 μsec delay
(a) PRESSURE RECORD (GAGE 2)

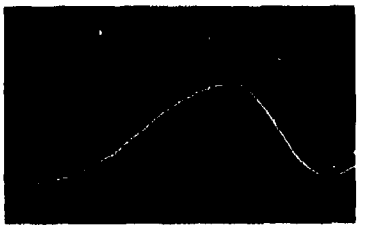

5000 lbs/cm (22.2 kN/cm)
50 μsec/cm 200 μsec delay
(b) LOAD CELL RECORD

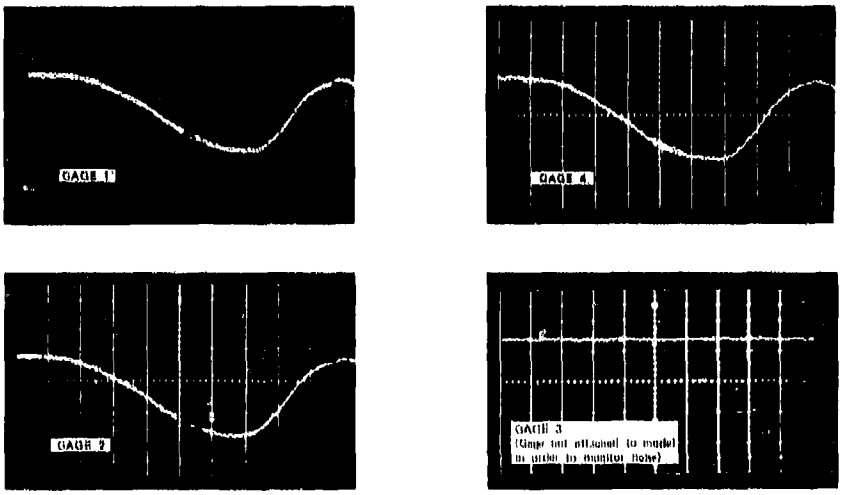

(c) 0.01%/cm 50 μsec/cm 200 μsec DELAY
STRAIN GAGE RECORDS FROM FRONT STATION

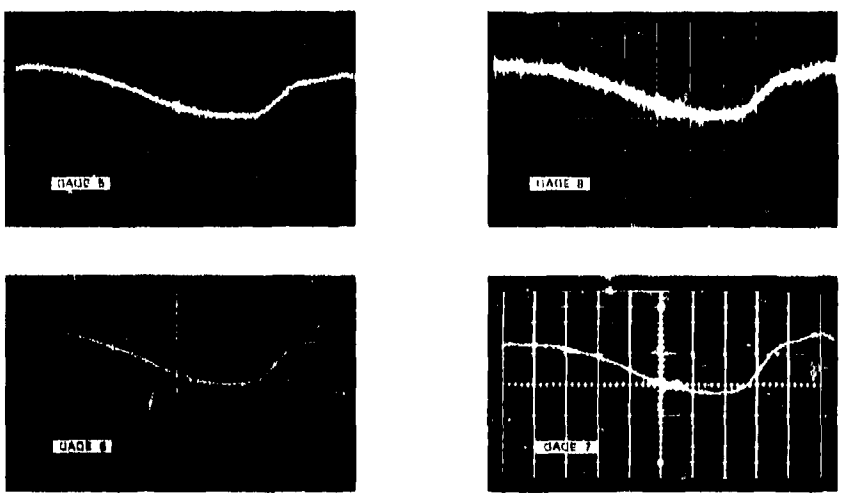

0.01%/cm 50 μsec/cm 200 μsec delay
(d) STRAIN GAGE RECORDS FROM AFT STATION

MA-3091-136A

FIGURE 14 TEST 37—NORMAL LOADING OF SOLID STEEL MODEL

Figure 15 shows the results of Test 34. In this test the axis of the solid steel model was tilted 5 degrees (0.09 rad) with respect to the axis of the piston, and the explosive charge mass was the same as that of Test 37. The bending strain due to the resulting transverse load can be seen most clearly in the records from Gages 6 and 8 at the aft station. Gages 5 and 7 were on the neutral plane of bending and therefore recorded only the axial strain of the rod; the peak axial strain of 0.015 percent is comparable to that for normal loading (Figure 15). The record from Gage 8 shows that in this case the superposed compressive axial strain and the tensile bending strain almost cancelled each other, resulting in a small total strain during the 500 μsec recorded. Thus the peak bending strain was also about 0.015 percent.

Thick-Walled Model

Figure 16 shows the applied load and aft station strain records from Test 40 in which the 3.37-pound (1.53-kg) thick-walled steel model was normal to the piston. The peak load was 16,500 pounds (73.4kN) and the average axial strain was 0.027 percent. As in Test 37, the circumferential variation in strain is small.

Figure 17 and 18 show the results from Tests 43 and 64. In Test 43 the peak load was 16,000 pounds (71.2 kN) and the peak axial strain at the aft station was 0.023 percent. In Test 64 the peak load was 15,000 pounds (66.7 kN) and the peak axial strain was 0.022 percent. The initial angle of tilt θ in Test 64 [19°30' (0.340 rad)] was 2.7 times that of Test 43 [7°10' (0.125 rad)]. The peak bending strain in Test 64 (0.042 percent) was 2.6 times that of Test 43 (0.016 percent). Thus there is a nearly linear relation between the angle of tilt θ and the bending strain.

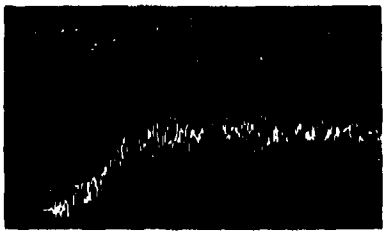

1000 psi/cm (6894 kPa/cm)
50 μsec/cm 100 μsec delay
(a) PRESSURE RECORD (GAGE 1)

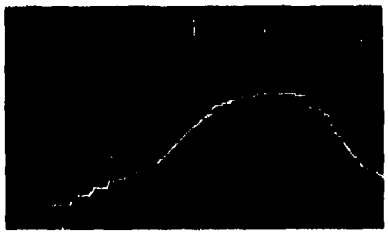

5000 lbs/cm (22.2 kN/cm)
50 μsec/cm 150 μsec delay
(b) LOAD CELL RECORD

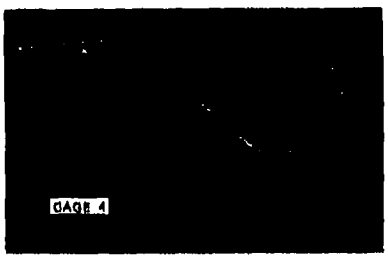

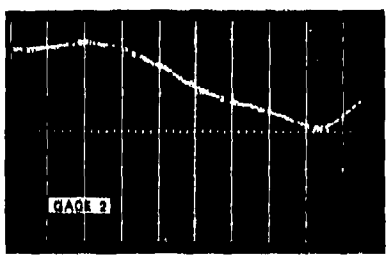

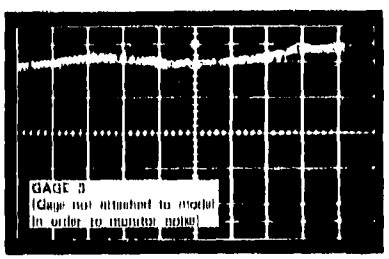

(c) 0.01%/cm 50 μsec/cm 150 μsec DELAY
STRAIN GAGE RECORDS FROM FRONT STATION

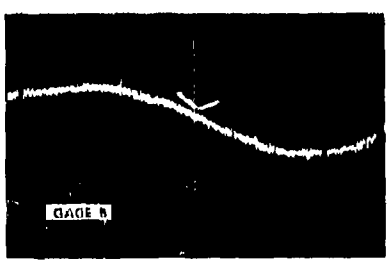

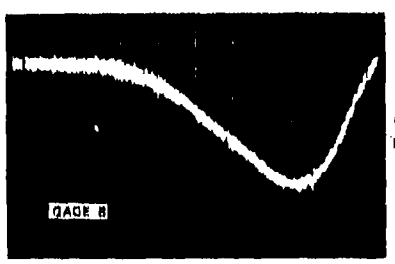

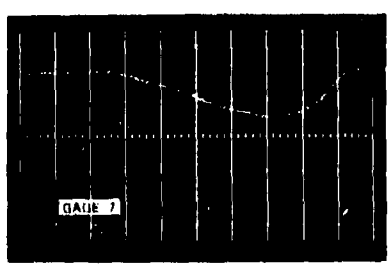

0.01%/cm 50 μsec/cm 150 μsec delay
(d) STRAIN GAGE RECORDS FROM AFT STATION

MA-3091-124A

FIGURE 15 TEST 34–5 (0.09 rad) ANGULAR LOADING OF SOLID STEEL MODEL

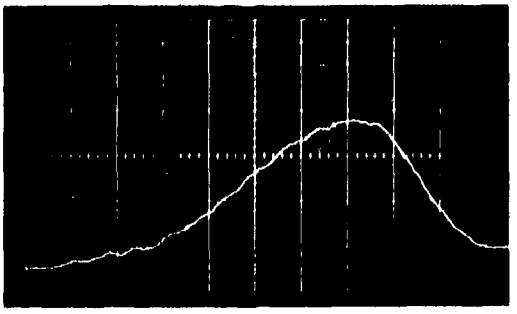

(a) LOAD CELL RECORD
[5000 lbs/cm (22.2 kN/cm)
50 μsec/cm 150 μsec delay]

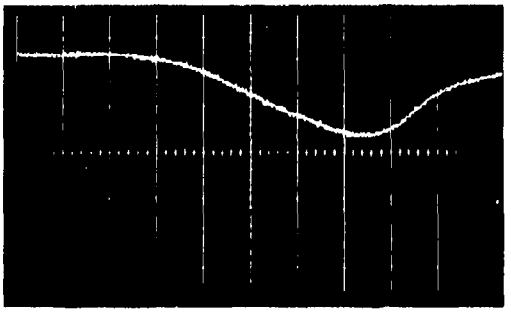

GAGE 7

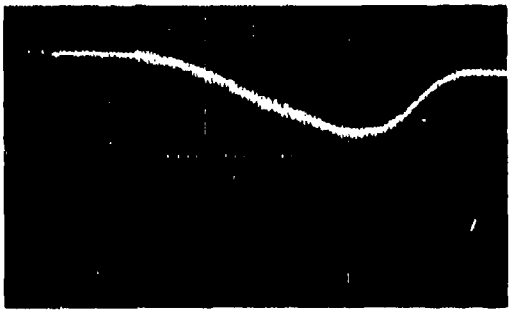

GAGE 6

GAGE 8

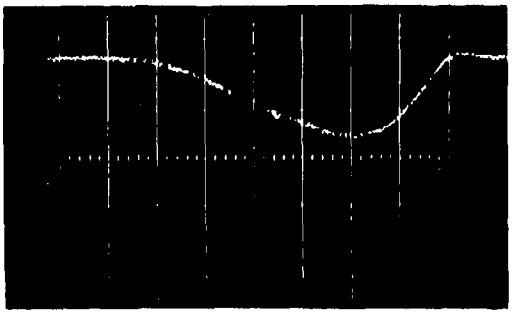

GAGE 5

(b) STRAIN GAGE RECORDS FROM AFT STATION
(0.016%/cm, 50 μsec/cm, 150 μsec delay)

MA-3091-130A

FIGURE 16 TEST 40—NORMAL LOADING OF THICK-WALLED MODEL

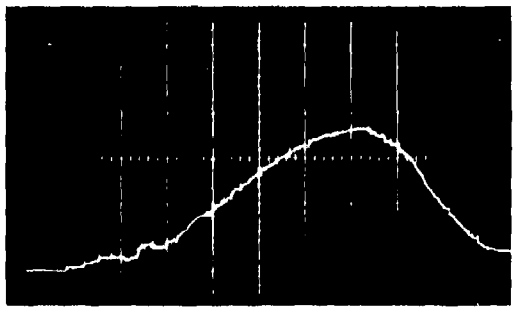

(a) LOAD CELL RECORD
[5000 lbs/cm (22.2 kN/cm)
50 μsec/cm 150 μsec delay]

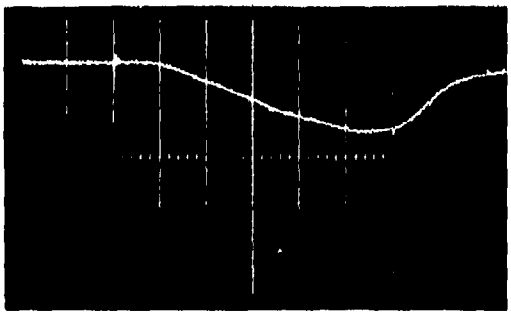

GAGE 7

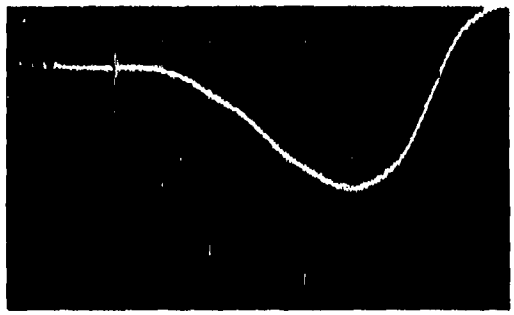

GAGE 6

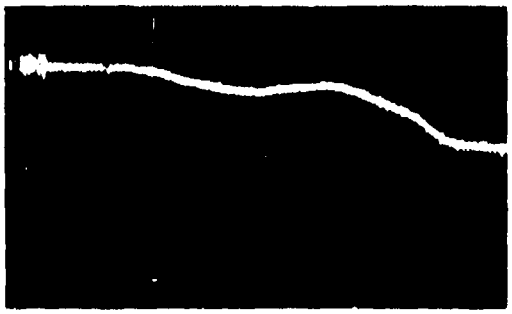

GAGE 8

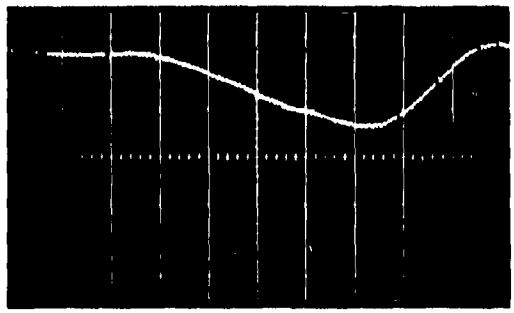

GAGE 5

(b) STRAIN GAGE RECORDS FROM AFT STATION
(0.016%/cm, 50 μsec/cm, 150 μsec delay)

MP-3091-132A

FIGURE 17 TEST 43–7°10′ (0.125 rad) ANGULAR LOADING OF THICK-WALLED MODEL

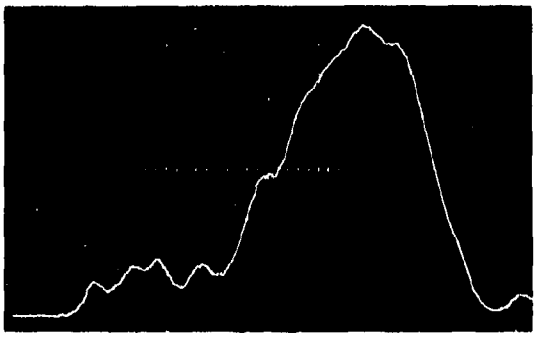

(a) LOAD CELL RECORD
[2500 lbs/cm (11.1 kN/cm) 50 μsec/cm
150 μsec delay]

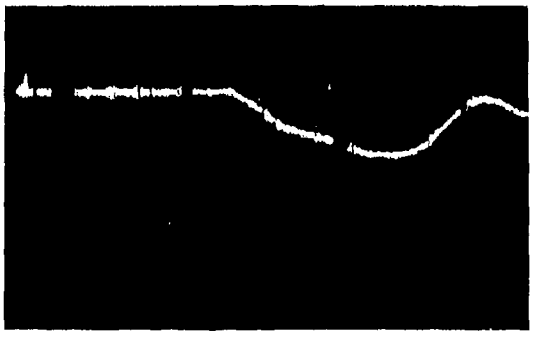

GAGE 5 (ε_{axial})

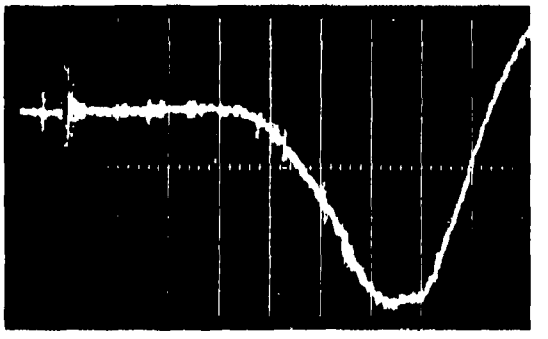

GAGE 8 ($\varepsilon_{axial} + \varepsilon_{bending}$)

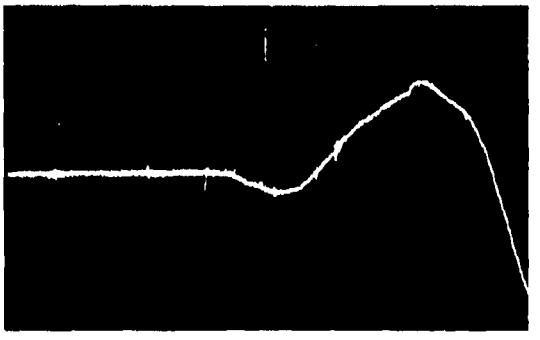

GAGE 6 ($\varepsilon_{axial} - \varepsilon_{bending}$)

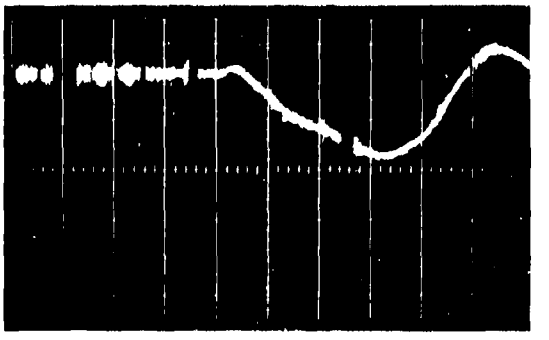

GAGE 7 (ε_{axial})

(b) STRAIN GAGE RECORDS FROM AFT STATION
(0.016%/cm, 50 μsec/cm, 150 μsec delay)

MA-3091-137A

FIGURE 18 TEST 64–19°30′ (0.340 rad) ANGULAR LOADING OF THICK-WALLED MODEL

Thin-Walled Model

Figures 19 and 20 show the records from Tests 55 and 66 in which the 1.37-pound (0.62-kg) thin-walled model was loaded both axially and laterally. In test 55 the angle of tilt was 8°10' (0.143 rad), the peak load was 11,000 pounds (48.9 kN), the peak axial strain was 0.019 percent, and the bending strain was small relative to the axial strain. In Test 66 the angle of tilt was 18°15' (0.319 rad), the peak load was 11,250 pounds (50.0 kN), the peak axial strain was 0.023 percent, and the peak bending strain was 0.015 percent. (Note that the strain records have different time scales in the two tests.)

CONCLUSIONS

The test results show that the load simulator can apply to model penetrators loads similar to those occurring in angle-of-attack impacts. The structural response of the penetrator has been accurately measured using hard-wired strain gages. The tests indicate that the loader could also be built in a larger size to test full-scale penetrators.

For the 1.5-inch-diameter penetrator models tested here, the shortest rise time produced was about 150 μsec. For a penetrator whose nose length is about 1.5 times its diameter, this corresponds to an impact velocity of 1.5 (1.5 inch)/150 μsec = 1250 ft/sec (385 m/sec). It may be desirable to further decrease the load rise time by making the orifice plate thinner or by making the piston surface harder to simulate greater impact velocoties.

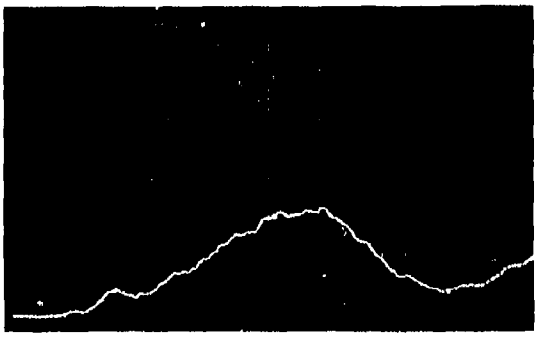

(a) LOAD CELL RECORD
[5000 lbs/cm (22.2 kN/cm)
50 μsec/cm 150 μsec delay]

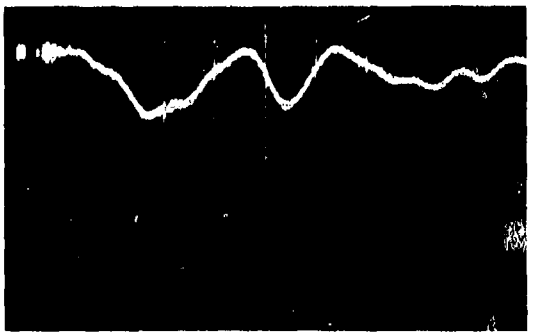

GAGE 7

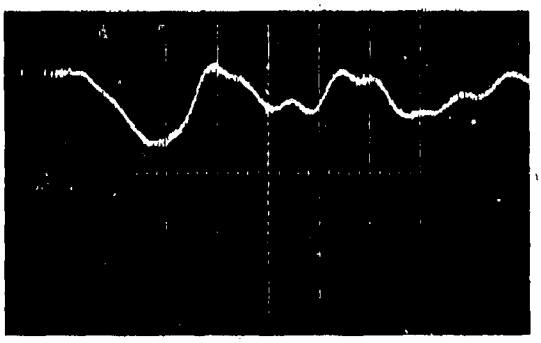

GAGE 6

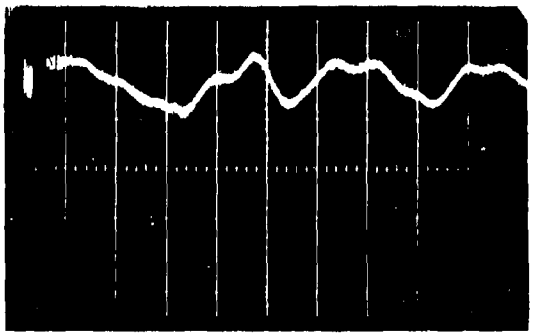

GAGE 8

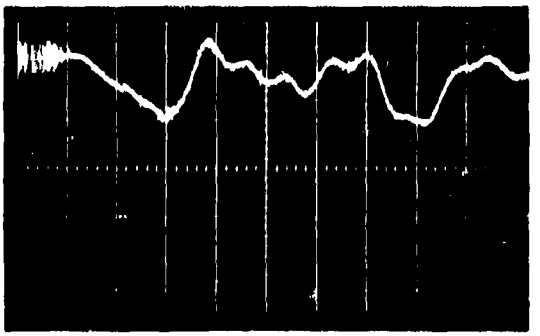

GAGE 5

(b) STRAIN GAGE RECORDS FROM AFT STATION
(0.016%/cm, 100 μsec/cm, 150 μsec delay)

MP-3091-138

FIGURE 19 TEST 55-8"10' (0.143 rad) ANGULAR LOADING OF THIN-WALLED MODEL

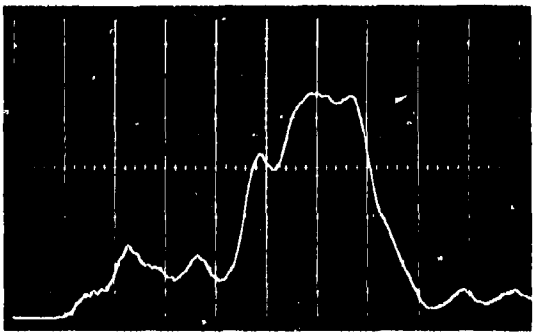

(a) LOAD CELL RECORD
[2500 lbs/cm (11.1 kN/cm)
50 μsec/cm 150 μsec delay]

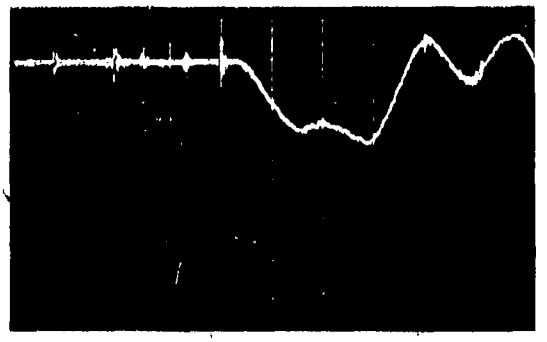

GAGE 6

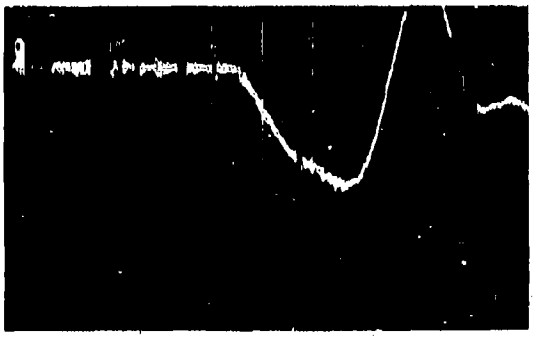

GAGE 5

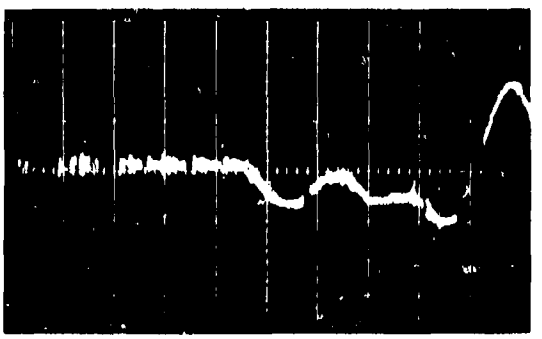

GAGE 7

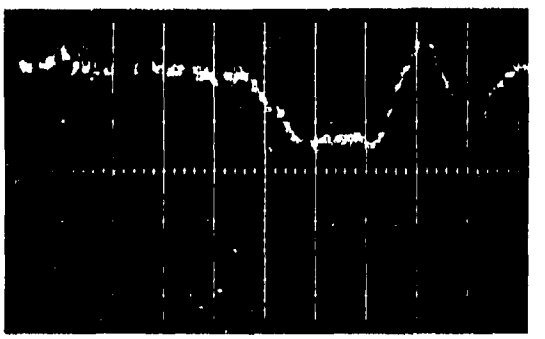

GAGE 8

(b) STRAIN GAGE RECORDS FROM AFT STATION
(0.016%/cm, 50 μsec/cm, 150 μsec delay)

MP-3091-139

FIGURE 20 TEST 66–18°15′ (0.319 rad) ANGULAR LOADING OF THIN-WALLED MODEL

4 ANALYSIS OF PENETRATOR RESPONSE

In this section we develop the theory for predicting penetrator response under angle-of-attack impacts, compare the response predicted by this theory with that measured in simulation experiments and with that measured in a reverse ballistics test performed at AVCO, and investigate the effect of specific loading and structural parameters on penetrator response.

As discussed previously, large strains and failures in penetrators were observed experimentally in several angle-of-attack impacts. Comparison of the location of these failures with the peak strains measured in the simulator tests performed here and in reverse ballistics tests performed at AVCO indicate that these failures occur as follows. Impacts at an angle of attack produce bending as well as axial thrust in the penetrator. When the total compressive stress due to axial thrust plus bending reaches the yield stress, the bending stiffness of the penetrator is reduced and the bending strain increases further until failure occurs. Thus, the analysis is based on elastic response because that is what determines whether or not failure can ultimately occur.

THEORY

The central portion of the penetrator, drawn schematically in Figure 21(a), is modeled by elastic Timoshenko beam theory including thrust. This formulation includes the two dominant response mechanisms governing angle-of-attack impacts: axial compression and bending under lateral loads. The front portion of the solid nose and the solid aft end are modeled as rigid masses. Loading of this structure is specified by the magnitude, time history, and orientation of a resultant impact force; in all cases studied here we take the resultant force to pass through a fixed point in the front mass.

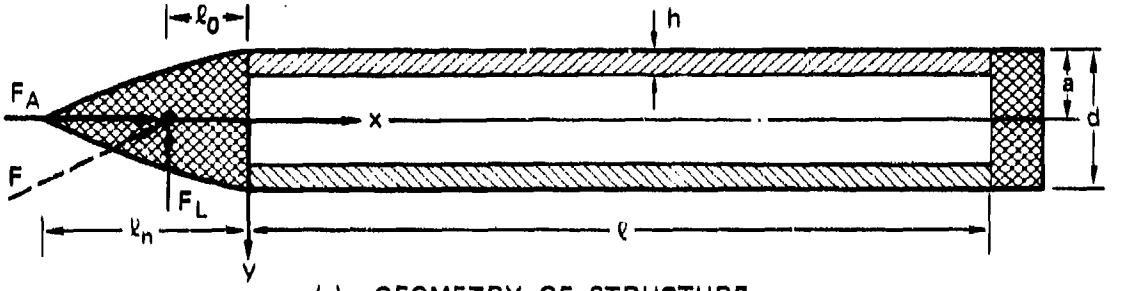

(a) GEOMETRY OF STRUCTURE

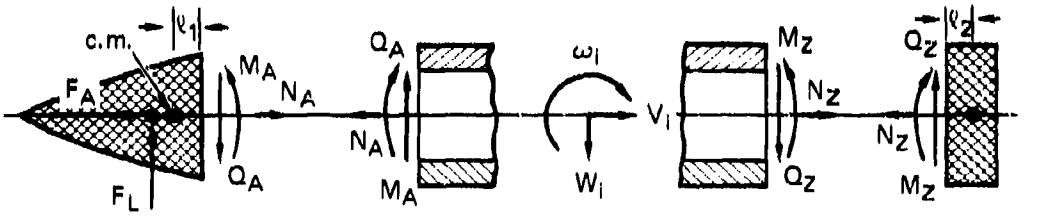

(b) FORCES AND MOMENTS ON THE BEAM AND FRONT AND AFT RIGID MASSES

MA-3091-109A2

FIGURE 21 MATHEMATICAL MODEL OF AN IDEALIZED PENETRATOR STRUCTURE

Beam Equations

Six equations governing the motion of the beam section are required: two governing axial compression and four governing bending. The equations governing axial response of the beam are

$$N - EA \frac{\partial u}{\partial x} = 0 \tag{1a}$$

$$\frac{\partial N}{\partial x} - \rho A \frac{\partial^2 u}{\partial t^2} = 0 \tag{1b}$$

where N is axial force in compression, E is modulus of elasticity, A is cross-sectional area, u is axial displacement, x is the coordinate along the beam axis, ρ is density, and t is time. The first of these equations is Hooke's law and the second is the equation of motion in the axial direction.

The equations governing bending response of the beam are

$$M + EI \Psi_x = 0 \tag{1c}$$

$$Q - k'AG(y_x - \Psi) = 0 \tag{1d}$$

$$\frac{\partial M}{\partial x} - Q + \rho I \frac{\partial^2 \Psi}{\partial t^2} = 0 \tag{1e}$$

$$\frac{\partial Q}{\partial x} - \rho A \frac{\partial^2 y}{\partial t^2} = 0 \tag{1f}$$

where M is bending moment, I is cross-sectional moment of inertia, Ψ is that part of the slope of the deflection curve caused by bending (the total slope y_x is caused by both bending and shearing), Q is shear force, $k' = \pi^2/12$ is the shear correction coefficient, G is shear modulus, and y is transverse deflection. The first of these

equations is the bending moment-curvature relation of elementary beam theory. The second expresses the shear-force shear-deformation relation. The third is the equation of motion for rotation, and the fourth is the equation of motion for translation.

The motion of the forward and aft rigid masses is coupled with the motion of the beam. It is convenient to treat this interaction by the characteristic equations of the beam. Therefore, we now discuss the characteristic form of equations (1).

Equations (1) are a set of partial differential equations in x and t. The method of characteristics affords a transformation of these equations into total differential equations that apply along particular, or characteristic, lines in the x-t plane. The details of this transformation are given in Reference 7. The reciprocal slopes of the characteristic lines correspond to wave speeds at which disturbances can propagate. For the system of equations (1), disturbances can propagate at four possible velocities along the beam: $\pm c_b$ and $\pm c_s$, where $c_b = \sqrt{E/\rho}$ is the bar velocity, and $c_s = \sqrt{k'G/\rho}$ is the shear velocity. Axial waves propagate at $\pm c_b$ and are governed by equations (1a) and (1b), while transverse waves propagate at both $\pm c_b$ and $\pm c_s$ and are governed by equations (1c) through (1f). To make the subsequent analysis more clear, we give the label $I^{\pm}$ to the characteristic lines having slopes $\pm 1/c_b$ when referring to equations (1a) and (1b) governing axial response, and $II^{\pm}$ to the same lines when referring to equation (1c) through (1f) governing transverse response, as indicated in Figure 22(b). We give the label $III^{\pm}$ to the characteristic lines having slopes $\pm 1/c_s$, as also indicated in Figure 22(b). The governing or characteristic axial equations along lines $I^{\pm}$ are

$$I^{\pm}: \quad d[N \mp \rho c_b A\, dv] = 0 \tag{2}$$

where $v = \partial u/\partial t$ is the axial particle velocity.

The characteristic transverse equations along lines $II^{\pm}$ and $III^{\pm}$ are

$$II^{\pm}: \quad d[M \pm \rho I\, c_b\, \omega] = \pm c_b\, Q\, dt$$
$$III^{\pm}: \quad d[Q \mp \rho A\, c_s\, w] = -k'AG\omega\, dt \tag{3}$$

where $\omega = \partial\Psi/\partial t$ is the rotational velocity and $w = \partial y/dt$ is the transverse velocity.

Equations (2) and (3) are two independent sets of total differential equations; that is, the solutions to equations (2) can be found independently from the solutions to equation (3). Each set of equations (2) or (3) are coupled, of course, and must be solved as a group. The solution to each set was obtained by a forward differencing finite difference method along the characteristics. So that solutions could be placed on a common right Cartesian grid, values at points H and J in Figure 22(b) were approximated from those at points G and K by linear interpolation before the numerical integration. Thus the solutions at point P can be written in terms of those at points G and K. This solution applies at all interior points of the grid of Figure 22(a). Details of the solution are given in Reference 7. At end points A and Z in the grid, the rigid masses must be taken into account.

End Mass Equations

The coupled motion of the front rigid mass and the front end of the Timoshenko beam is governed by the equations of motion and stress-strain relations of the Timoshenko beam, by the equations of motion of the front rigid mass, and by requiring compatibility of displacement and rotation of the front end of the beam and the front rigid mass. The equations for the Timoshenko beam are most conveniently represented by the finite difference

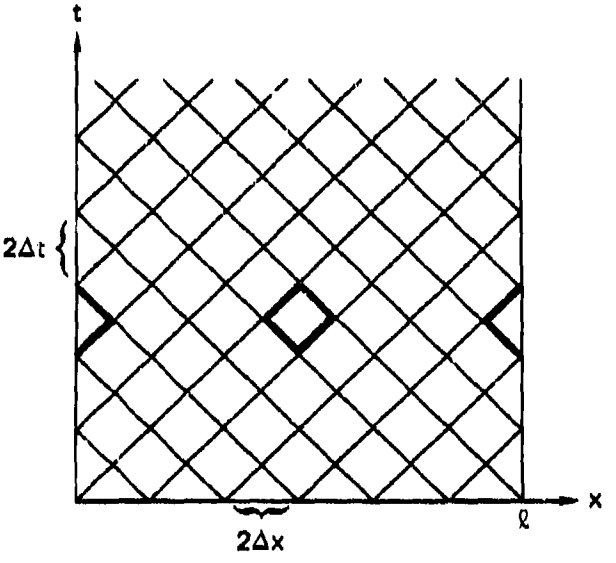

(a) COMPLETE GRID (COARSE SPACING FOR CLARITY)

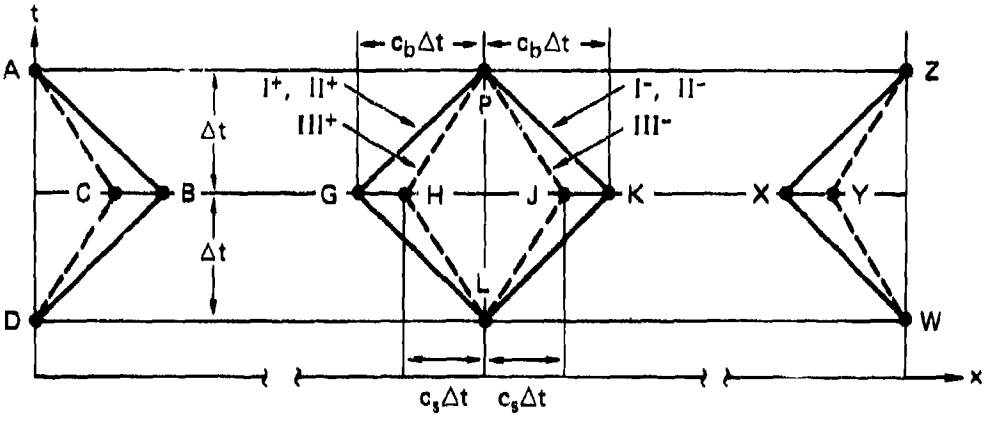

(b) DETAILS OF SHADED PORTIONS OF PART (a)

MA-3091-159

FIGURE 22 SOLUTION GRID FOR METHOD OF CHARACTERISTICS

form of the characteristic equations corresponding to characteristic lines I^-, II^-, III^- on the grid in the left side of Figure 22(b):

$$I^-: \quad N_A - N_B + \rho c_b A(v_A - v_B) = 0 \tag{4a}$$

$$II^-: \quad M_A - M_B - \rho I c_b(\omega_A - \omega_B) = -c_b \left(\frac{Q_A + Q_B}{2}\right) \Delta t \tag{4b}$$

$$III^-: \quad Q_A - Q_C + \rho A c_s(w_A - w_C) = -k'AG\left(\frac{\omega_A + \omega_C}{2}\right) \Delta t \tag{4c}$$

The equations for axial, transverse, and rotational motion of the front rigid mass are:

$$F_A + N_A = m_f \frac{dv_f}{dt} \tag{5a}$$

$$-F_L + Q_A = m_f \frac{dw_f}{dt} \tag{5b}$$

$$-M_A + Q_A \ell_o = I_f \frac{d\omega_f}{dt} \tag{5c}$$

where the subscript f indicates values at the front mass, m_f is the front mass, F_A is axial load, F_L is lateral load, $_o$ is indicated in Figure 21(a), and I_f is the moment of inertia of the front mass about the point on the axis through which F_L acts.

In finite difference form these equations are

$$F_A + N_A = m_f \left(\frac{v_A - v_D}{2\Delta t}\right) \tag{6a}$$

$$-F_L + Q_A = m_f \left(\frac{w_A - w_D}{2\Delta t}\right) \tag{6b}$$

$$-M_A + Q_A \ell_o = I_f \left(\frac{\omega_A - \omega_D}{2\Delta t}\right) \tag{6c}$$

Because the same values of v, w, and ω are used in equations (4) and (6), compatibility of displacement and rotation between the front rigid mass and the beam is ensured.

The couples motion of the aft mass and the aft end of the beam is governed by a similar set of equations. The finite difference form of the characterkstic equations for the aft mass is

$$I^+: \quad N_Z - N_Z - \rho c_b A(v_Z - v_X) = 0 \tag{7a}$$

$$II^+: \quad M_Z - M_X + \rho I c_b (\omega_Z - \omega_X) = c_b \left(\frac{Q_Z + Q_X}{2}\right) \Delta t$$

$$III^+: \quad Q_Z - Q_Y - \rho A c_s (W_Z - W_Y) = -k'AG \left(\frac{\omega_Z + \omega_Y}{2}\right) \Delta t \tag{7c}$$

The finite difference form of the equations of motion of the aft mass are:

$$-N_z = m_a \left(\frac{v_Z - v_W}{2\Delta t} \right) \qquad (8a)$$

$$-Q_z = m_a \left(\frac{w_Z - w_W}{2\Delta t} \right) \qquad (8b)$$

$$M_z + Q_z \ell_2 = I_a \left(\frac{\omega_Z - \omega_W}{2\Delta t} \right) \qquad (8c)$$

where the subscript a refers to values at the aft mass, m_z is the aft mass, ℓ_2 is indicated in Figure 21(b), and I_a is the moment of inertia of the aft mass about its center.

Each set of six simultaneous linear algebraic equations, (4) with (6) and (7) with (8), can then be solved for their six unknowns at points A and Z. By representing values of the variables at points C and Y in terms of their values at points A, B, and D, and Z, X, and W, the solutions can also be expressed in terms of their values at the corners of the Cartesian grid of Figure 22(b). The complete solution is given in Appendix B.

Payload Equations

When a penetrator impacts a target, the inertia forces from an interior payload can affect the response of the penetrator casing. The effect of the axial inertia can be eliminated during the early-time response simply by attaching the payload with a compliant elastic mount or by a weak plastic mount such as crushable foam. The transverse or whipping inertia cannot be treated in a similar way because, to allow maximum penetration, the outside diameter of the penetrator, and hence the tolerance between the penetrator casing and the payload, must be minimized. Thus, the effect of the payload transverse inertia must be examined.

The bending stiffness of the payload is generally much less than that of the penetrator casing. Thus, the payload is modeled as a distributed mass with no bending stiffness. This effect was modeled mathematically by increasing the density from ρ to ρ' in the equation of translational motion of the beam. The corresponding shear velocity c_s decreases to c_s'. In the region of the payload, the following characteristic equation must be used:

$$III^{\pm}: \quad d[Q \mp \rho' A c_s' w] = -k A G \omega dt \qquad (9)$$

Note that this changes the location of points H and J in Figure 22(b). Nevertheless, these equations are solved in the same way as the beam equations without the payload but with appropriate locations for H and J.

RESPONSE PREDICTED IN SIMULATOR EXPERIMENTS

The analysis was used first to calculate the penetrator strains measured in two of the simulator experiments described in Section 3. The structures analyzed were a thick-walled penetrator model (Test 64) and a thin-walled penetrator model (Test 66), both with hemispherical noses; the dimensions of these structures are given in Table 1. The loads measured in the experiments were used as input for the analyses. To account for the uncertainty in the point of application of the resultant loading force in the simulator experiments, upper and lower bounds on the response were calculated for extreme locations of the point of load application for each experiment. These comparisons not only provided a check on the analysis but also aided in the understanding of the simulator loading technique.

To describe the loading of the penetrator in a simulator experiment, we must know the vertical force resultant F_V (i.e., the force parallel to the loading piston axis), the horizontal force resultant F_H, the angle of inclination θ of the penetrator axis relative to the vertical loading piston axis, and the points of application of F_V and F_H (about which

the distributed vertical and horizontal forces produce no moments). From the inset in Figure 23, the axial and transverse force resultants are, respectively,

$$F_A = F_V \cos\theta + F_H \sin\theta$$

and

$$F_L = F_V \sin\theta - F_H \cos\theta$$

We now obtain each of these loading parameters from the experimental measurements. The vertical force is obtained from the load cell readings taken during the test. However, the load cell record is the force on the bottom side of the sliding disc, which differs from the force on the penetrator by the acceleration force of the disc. The strain gage records indicate that no noticeable force is applied to the penetrator during approximately the first 175 μsec of the load cell record [e.g., see Figure 18(a)] when all the gaps in the load path between the load cell and penetrator are closed and the sliding disc begins to deform under a small force. Therefore, as input to the analysis, we omit this early portion of the load cell record. In addition, subsequent small oscillations appear in the load cell record. These are caused by a vibration in the piston. This vibration is not transmitted to the penetrator model through the plastically deforming sliding disc as evidenced by the smooth strain gage records [Figure 18(b)]. Therefore, the oscillations were also smoothed out for the F_V input. Thus, the F_V curves used in the analysis of these two tests were taken as shown in Figures 23 and 24, where they are compared with the actual load cell records.

A reasonable assumption concerning F_H is that the ratio of F_H to F_V in a given experiment is constant for the duration of the loads. This ratio was determined from high speed movies of the penetrator in free flight, during which the center of gravity of the penetrator travels in the direction of the resultant impulse (see Section 3). The ratio F_H/F_V is equal to the slope of the trajectory of the center of mass of the penetrator, which could be measured to within ±10 percent. For

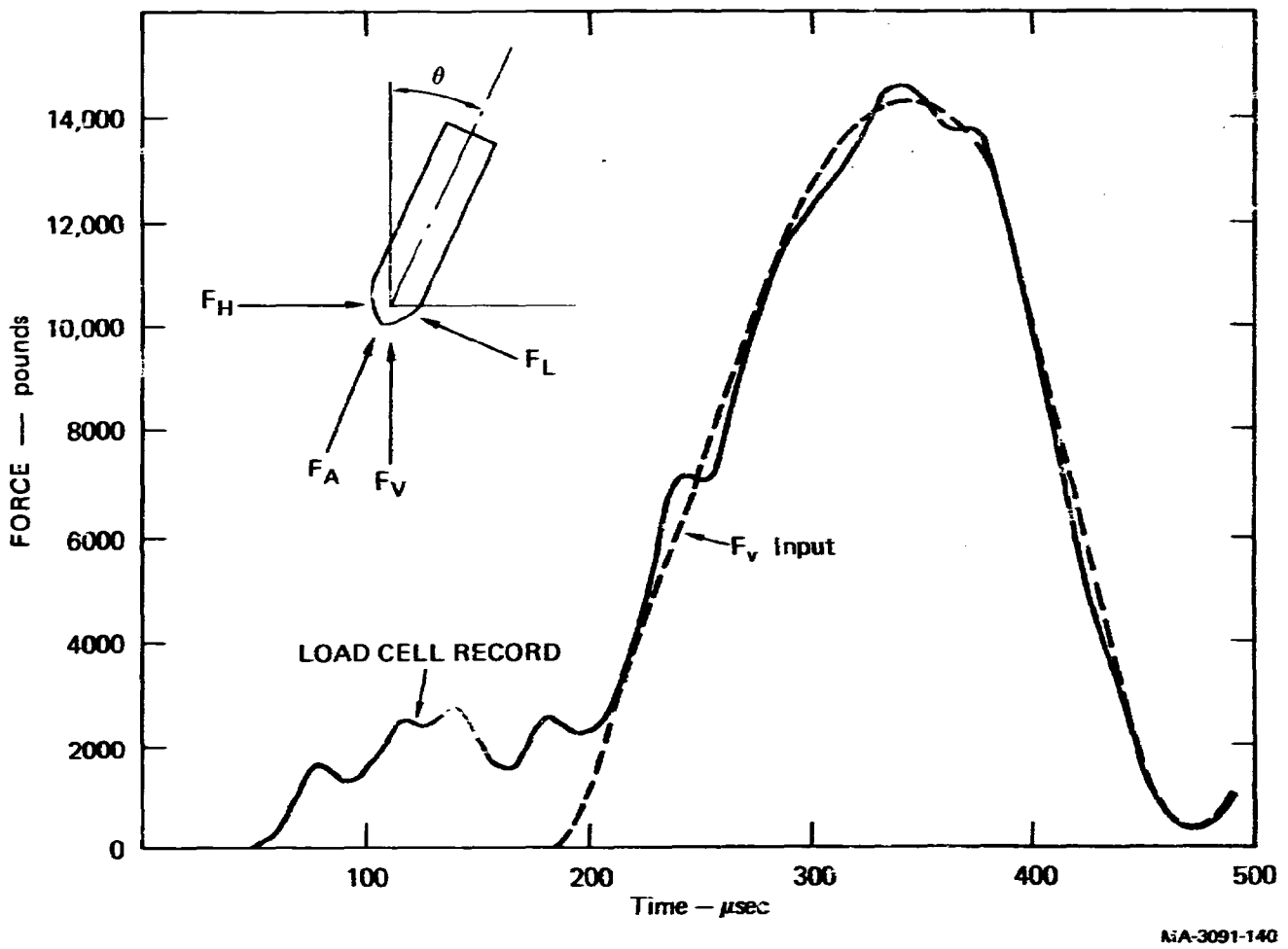

FIGURE 23 LOAD CELL RECORD AND F_V INPUT FOR SIMULATOR TEST 64 (THICK-WALLED STRUCTURE)

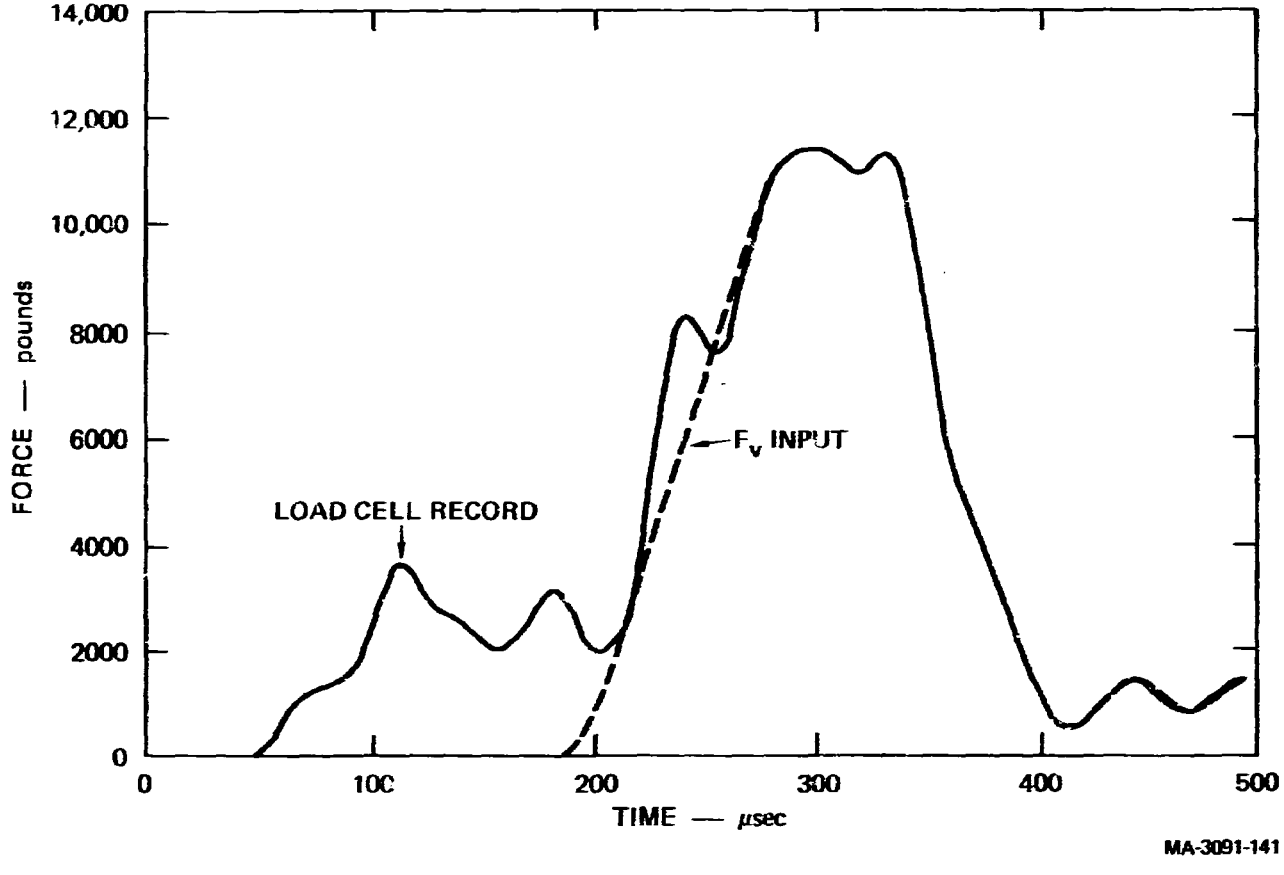

FIGURE 24 LOAD CELL RECORD AND F_V INPUT FOR SIMULATOR TEST 66 (THIN-WALLED STRUCTURE)

Tests 64 and 66, in which θ is in the neighborhood of 20 degrees, a 10 percent variation in F_H leads to only a 2.5 percent variation in F_L and essentially no variation in F_A. In Test 64, $F_H/F_V = 0.141$, and in Test 66, $F_H/F_V = 0.074$.

The angle of inclination of the penetrator model was measured before the experiment to an accuracy of ±15'. In Test 64 $\theta = 19°30'$, and in Test 66 $\theta = 18°15'$. For these angles, ±15' variation leads to about ±1 percent variation in F_L and essentially no variation in F_A. Since the exact point of application of the load is unknown, the response was predicted for two bounds on this location. One bound on the location of the point of load application is through the nose tip of the penetrator at the axis. This is a left bound (for the configuration shown in Figure 8) because the penetrator models were inclined to the vertical so that the point of load application is actually to the right of the penetrator axis. The bound on location to the right was taken as the center of the dent in the sliding disk because the resulting motion of the penetrator was to the right (Figure 8).

For Test 64, Figure 25 shows the upper and lower bounds on predicted strains along with the strain measured at strain gage 8. The error bands on each of the predicted strains correspond to uncertainty in F_H and θ. The total strain calculated for the two extreme points of load application bound the initial peak measured in the experiment. Since the edge of the dent was so near the axis tip (0.06 inch), it is reasonable that the upper bound calculation lies closer to the measured response. It also indicates that the predicted strain depends significantly on the point of load application. The bounds on the actual point of application of the resultant load in this experiment could be decreased, for example, by taking the left bound (Figure 8) as the left edge of the dent in the sliding disk.

For Test 66, Figure 26 shows the upper and lower bound calculated strains along with the strain measured at gage 5. Again, the error bands represent variations in F_H and θ. In this case, the first peak in strain is predicted very closely by the lower bound calculation,

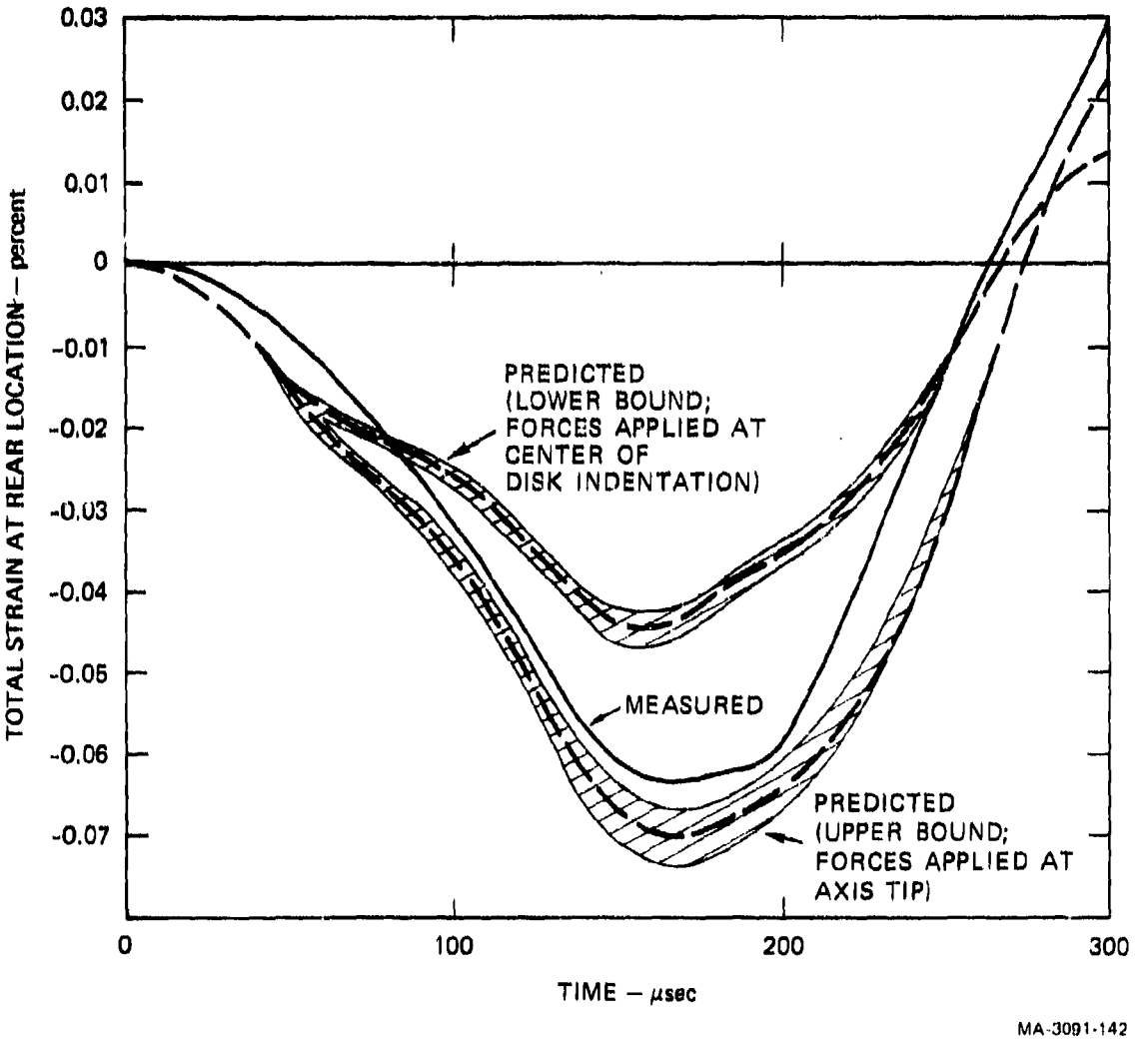

FIGURE 25 PREDICTED STRAINS AND MEASURED STRAIN IN SIMULATOR TEST 64 (THICK-WALLED STRUCTURE)

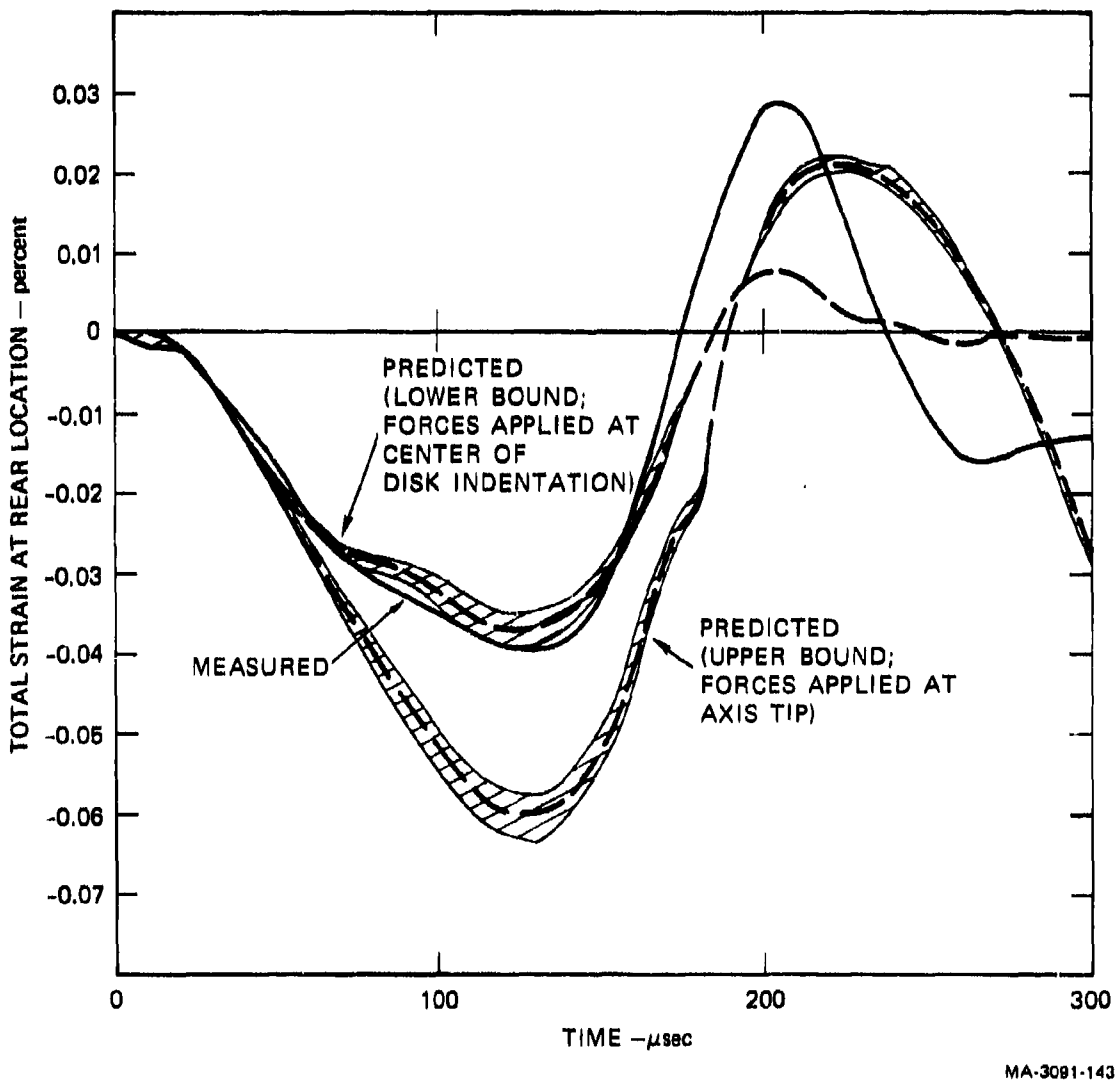

FIGURE 26 PREDICTED STRAINS AND MEASURED STRAIN IN SIMULATOR TEST 66 (THIN-WALLED STRUCTURE)

indicating that F_H was applied near the center of the dent. This is reasonable since the dent in this test was relatively small (0.3-inch diameter).

These comparisons show that, with accurate knowledge of the loads on the penetrator, the analysis is capable of predicting penetrator response with reasonable accuracy. It also shows, however, that considerable differences arise from uncertainty in the point of application of the loads. Thus, although the predicted response is accurate for a given input, the correlation with experiments is limited by the quality of the experimental load data.

APPLICATION OF THE ANALYSIS

Using the analysis, we now determine the effects of eccentricity factor, pulse shape, rise time, end masses, and lateral payload on penetrator response and nose rotation as it affects terradynamics.

Eccentricity Factor

As further verification of the applicability of the analysis and to estimate the ratio of lateral to axial load (called the eccentricity factor η) developed on impact at an angle of attack, we applied the analysis to the reverse ballistics Test D-1 performed at AVCO.[5] The eccentricity factor was determined by adjusting the axial and lateral load amplitudes so that the predicted strain response best matched the measured strain response.

The penetrator structure used in AVCO's Test D-1 is shown in Figure 27. This structure was impacted by a 15.2-inch-diameter (38.6-cm-diameter) mortar projectile at 1500 ft/sec (457 m/sec) at a 5 degree angle of attack. The strain data used here were taken from the three stations indicated in Figure 27. From these strain measurements, we computed the axial and bending strains at these three locations on the structure at each of three times. The nine axial and nine bending strain data points are shown in Figures 28(b), 28(c), and 28(d).

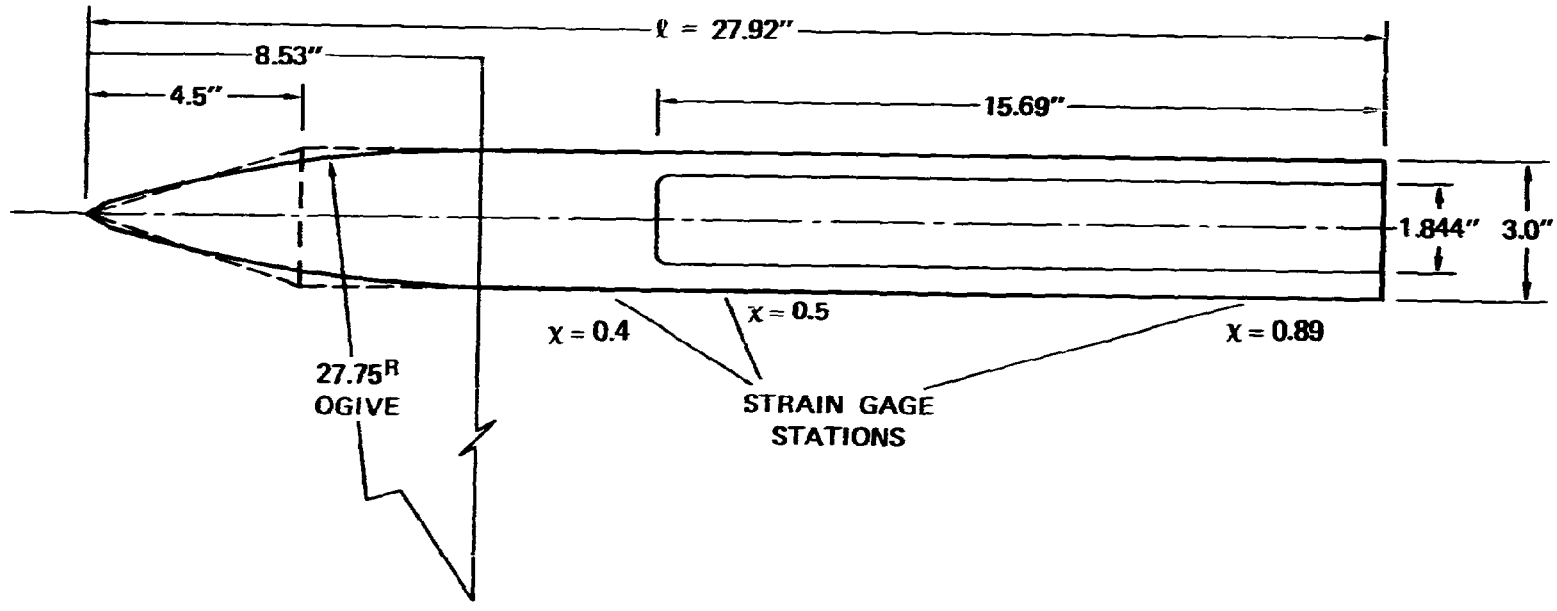

MA-3091-144

FIGURE 27 SCHEMATIC OF AVCO REVERSE BALLISTICS TARGET PROJECTILE

Dashed lines indicate idealized mathematical model with conical rigid nose.

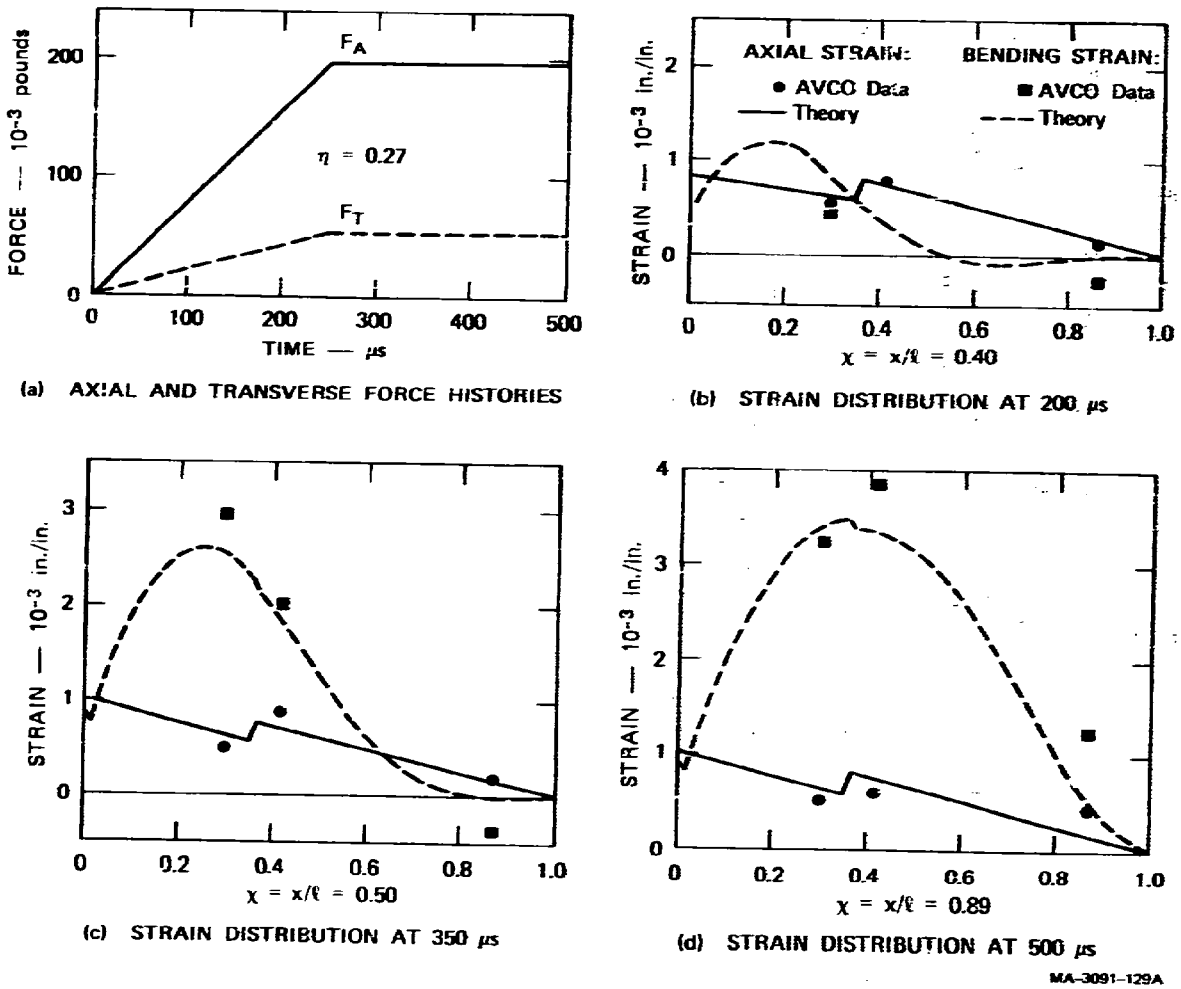

FIGURE 28 COMPARISON OF THE STRAIN PREDICTED FOR THE IDEALIZED PENETRATOR STRUCTURE OF FIGURE 27 WITH THE STRAIN MEASURED IN AVCO REVERSE BALLISTICS TEST D-1

The idealized structure used to calculate strains is also shown in Figure 27. The nose length is 4.5 inches (11.4 cm). In the structure tested, this length is the distance between the point of the nose and the station where the diameter reaches 77 percent of the diameter of the aft cylindrical section. The shapes of both axial and lateral load-time histories were taken as bilinear, with the rise time of 250 μsec corresponding to the 4.5-inch nose length divided by the impact velocity of 1500 ft/sec. In the analysis, the loads were applied at the center of mass of the rigid nose of the idealized structure.

The axial and lateral load amplitudes that give best agreement between measured and calculated strains were determined independently. For example, the axial response was first calculated for an axial load of unit amplitude. Then, for each axial strain data point, the unit load was weighted such that the calculated axial strain agreed with the measured strain. The axial load amplitude that best matched the axial strain data was taken as the average of the nine such weighting factors; this gives F_A = 195,000 pounds. By the same method, we found that a lateral load amplitude of 53,000 pounds best matched the bending strain data.

These load histories and resulting strain distributions are shown in Figure 28. In general, good agreement was obtained between the calculated and measured strains. It is concluded that this analysis is capable of predicting the shape of the strain distribution and its time history in a penetrator under angle-of-attack impacts. For this 5 degree angle of attack, the eccentricity factor is η = 53,000/195,000 = 0.27. Thus, the eccentricity angle, $\tan^{-1}\eta$ = 15 degrees, is greater than the angle of attack α by a factor of about 3. This result will be used in Section 5 in the calculation of critical impact curves.

The effect of varying the eccentricity factor was studied by applying loads of different eccentricity factors to another structure. Since only relative changes in the response are of interest, the structure analyzed had only the gross characteristics of penetrators. Specifically, we analyzed a simple steel tube with a ratio of length to outside diameter

of $\ell/d = 6$ and a ratio of radius-to-thickness of $a/h = 4$. The axial load history is shown in Figure 29(a). Calculations were made for seven different eccentricity factors ranging in value from 0 to 0.3.

The stress histories at Station $\chi = 0.4828$ for the tensile surface (Side A) and the compressive surface (Side B) of the structure for three different load ratios are shown in Figure 29(b). Table 2 presents the peak tensile and compressive stresses and the times and locations at which they occur. The time and location of peak stress change monotonically, but only slightly, over the range of load ratios, resulting in a nearly linear variation in peak tensile and compressive stresses with load ratio, as shown in Figure 29(c). Thus, for a particular loading rate and length of structure, the time and location of peak stresses do not change significantly, and their magnitude varies directly with load ratio for ratios of 10 percent to 30 percent.

Table 2

DEPENDENCE OF MAXIMUM STRESS ON TRANSVERSE/AXIAL FORCE RATIO ($\ell/d = 6$, $a/h = 4$)

F_L/F_A	0	0.05	0.10	0.15	0.20	0.25	0.30
Maximum tensile stress/σ_s	0	0	0.237	0.542	0.850	1.173	1.479
Location - χ	--	--	0.52	0.48	0.48	0.45	0.45
Time - τ	--	--	4.41	4.50	4.50	4.50	4.50
Maximum compressive stress/σ_s	-1	-1.099	-1.356	-1.621	-1.902	-2.203	-2.479
Location - χ	0	0.21	0.24	0.31	0.31	0.34	0.34
Time - τ	3.33	3.75	3.75	3.75	3.75	3.84	3.84

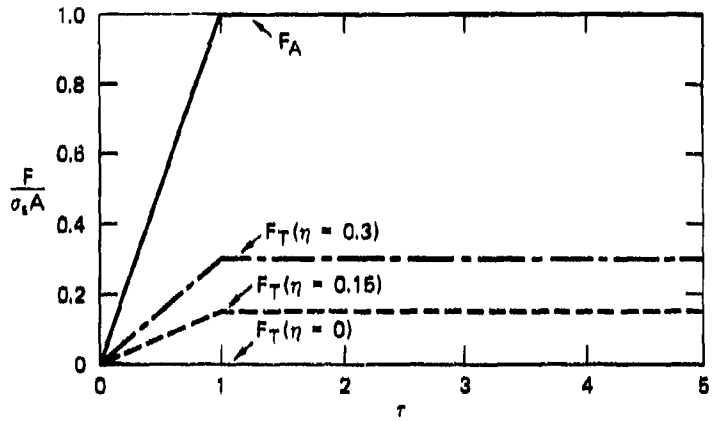

(a) LOAD HISTORY

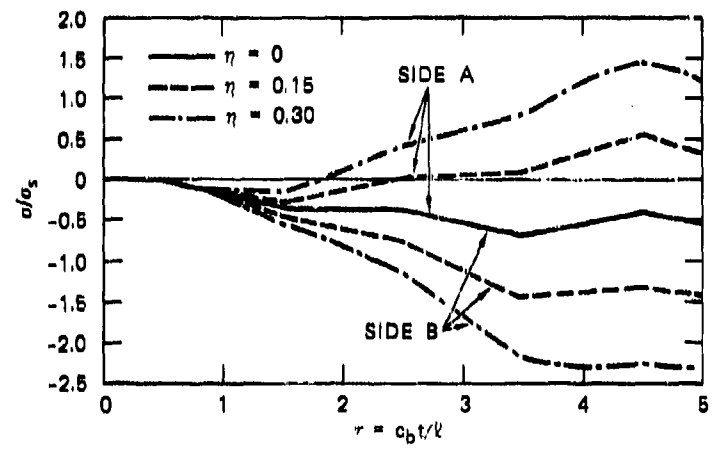

(b) STRESS HISTORIES AT $\chi = x/\ell = 0.4828$

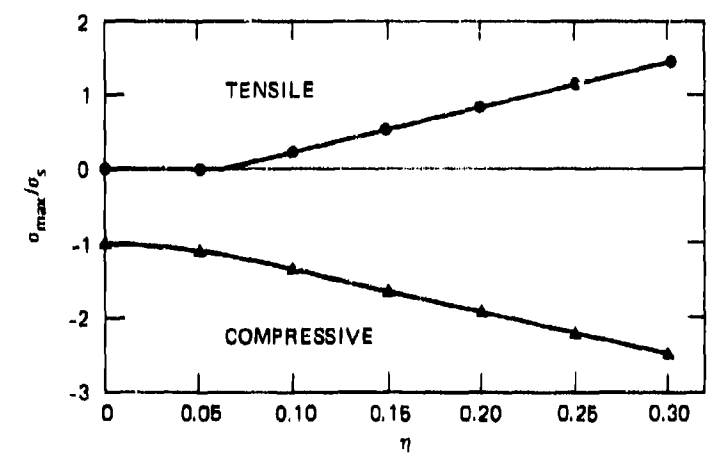

(c) PEAK STRESS VERSUS ECCENTRICITY FACTOR, η

MA-3091-113A

FIGURE 29 DEPENDENCE OF TOTAL STRESS ON ECCENTRICITY FACTOR IN A SIMPLE STEEL TUBE ($\ell/d = 6$, $a/h = 4$)

Pulse Shape

The effect of the shape of the loading-time curve on penetrator response was studied by applying loads of three different time histories to the same structure. The axial load time histories are shown in Figure 30(a); in each case the ratio of the lateral load to the axial load was 0.2. The structure was the same simple steel tube used to study the eccentricity factor ($\ell/d = 6$, $a/h = 4$).

For the three load histories the corresponding axial and (tensile) bending stress histories at Station $\chi = 0.2759$ are shown in Figure 30(b). At $\tau = 3$, that is, after three transits of a longitudinal wave over the length of the structure, Figure 30(a) shows that loading Force A has just reached its peak amplitude, Force B is about 14 percent less than Force A, and Force C is about 24 percent less than Force A. At $\tau = 3.5759$, the time required for the disturbance from the load at $\tau = 3$ to arrive at the $\chi = 0.2759$ station, Figure 30(b) shows that the bending stress for Load B is about 10 percent less than bending stress for Load A and that bending stress for Load C is about 20 percent less than bending stress for Load A. Axial stress for Load B is about 19 percent less than axial stress for Load A, and axial stress for Load C is about 25 percent less than axial stress for A. Thus, for these loading curves, having rise times of three to five transit times, the stresses generally follow the loading, and the effect of the detailed shape of the loading curve on the stresses is small.

Rise Time

The effect of loading rise time on penetrator response was studied by applying loads with the different rise times as shown in Figure 31(a) and with an eccentricity factor of 0.2. The structure was the simple steel tube analyzed previously. The bending and axial stress histories at Station $\chi = 0.4828$, normalized with respect to $\sigma_s = F_A/A$, corresponding to each loading curve are shown in Figure 31(b).

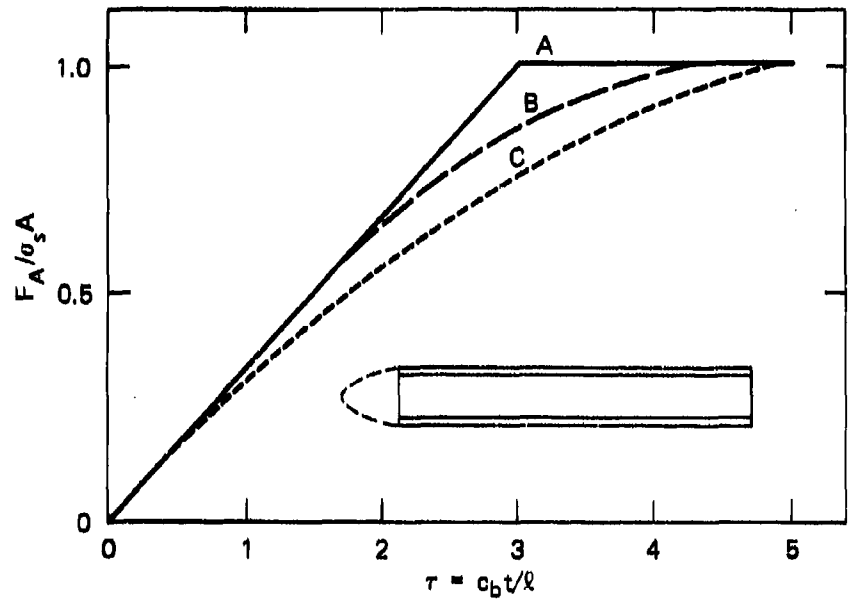

(a) LOAD HISTORIES (η = 0.20)

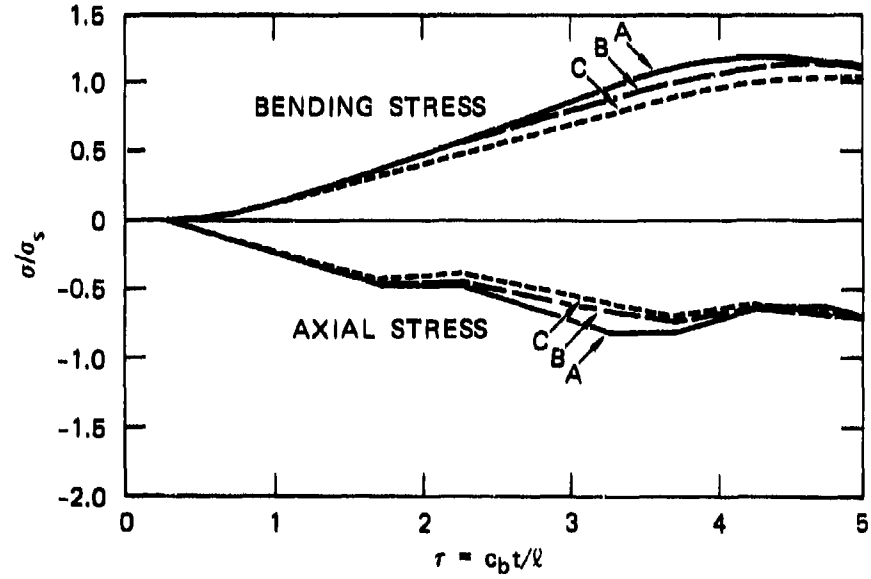

(b) AXIAL AND BENDING STRESS HISTORIES AT $\chi = x/\ell = 0.2759$

MA-3091-112A

FIGURE 30 RESPONSE OF A SIMPLE STEEL TUBE TO DIFFERENT LOAD HISTORIES (ℓ/d = 6, a/h = 4)

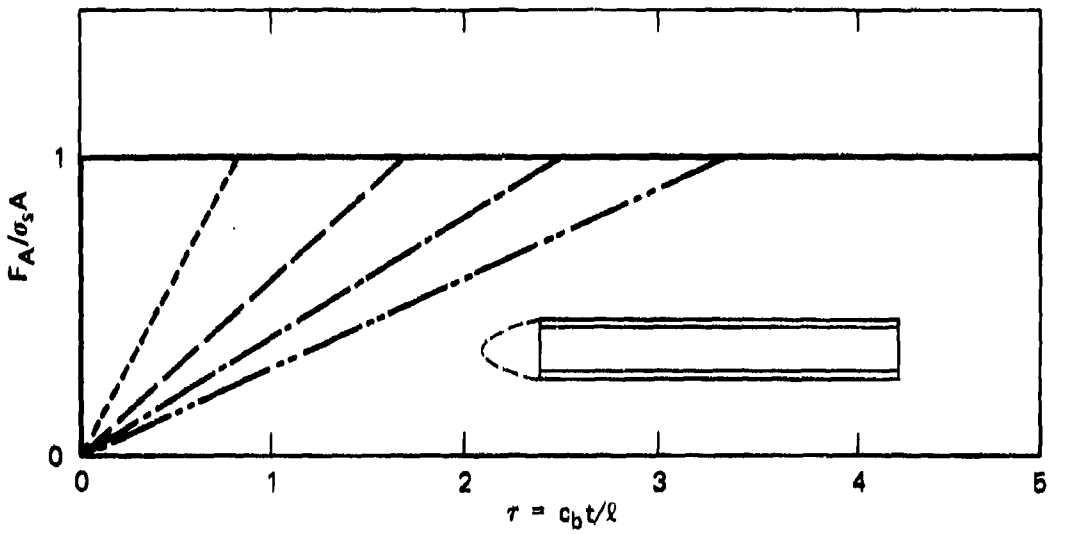

(a) AXIAL LOADING FORCE, F_A VERSUS TIME (η = 0.20)

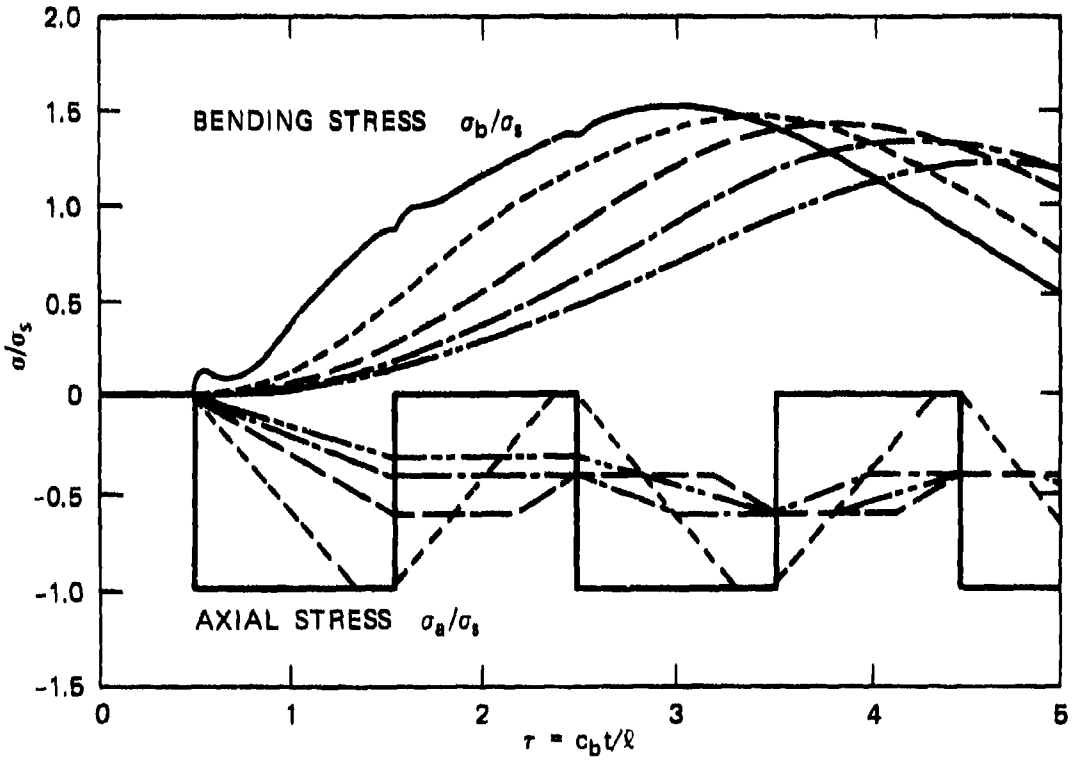

(b) STRESS VERSUS TIME AT χ = x/L = 0.4828

MA-3091-121A

FIGURE 31 RESPONSE OF A SIMPLE STEEL TUBE TO LOADS WITH DIFFERENT RISE TIMES (ℓ/d = 6, a/h = 4)

The largest bending stress value ($\sigma_b/\sigma_s = 1.51$) is produced by the loading of zero rise time (step input). In order of increasing loading rise times, the peak bending stresses σ_b/σ_s produced are 1.48, 1.40, 1.31, and 1.20. As the rise time increases further, the peak stress at this location approaches the steady-state value of $\sigma_b/\sigma_s = 0.793$. Furthermore, the time at which the peak occurs increases with rise time.

For the axial stress, the peak stress at a location is determined by whether the loading rise time is less than or greater than the time required for a reflected tensile stress wave to arrive at that location from the aft free end. For the loading curves with rise times of less than one transit time, the maximum value of σ_a/σ_s is -1.00. For the loading curves with rise times of more than one transit time, the maximum stress is $\sigma_a/\sigma_s = -0.617$. The steady-state value at this location is $\sigma_a/\sigma_s = -0.517$.

Thus, we conclude that the largest effects of increasing the loading rise time are to increase the times at which peak bending occurs and to vary the axial stress for loading rise times near one transit time. For rise times larger than two transit times, the variation in loading rise time has less effect on the peak bending stress and the peak axial stress.

End Masses

The effect of including the forward and aft rigid end masses in the calculation of penetrator response was determined by analyzing the structure shown in Figure 32(a). The central portion of the structure is the steel tube analyzed in previous calculations. The front conical mass has a length equal to the outside diameter d, and the aft cylindrical mass has a length equal to 1/3 the diameter. Thus, the forward and aft masses are equal, each being about 12.7 percent of the mass of the hollow section. Four versions of this structure were analyzed: without end masses, with a front mass, with an aft mass, and with both front and aft masses. In each case the eccentricity factor is $n = 0.2$ and the rise time is $\tau = 2.5$ as shown in the top of Figure 32(b). For

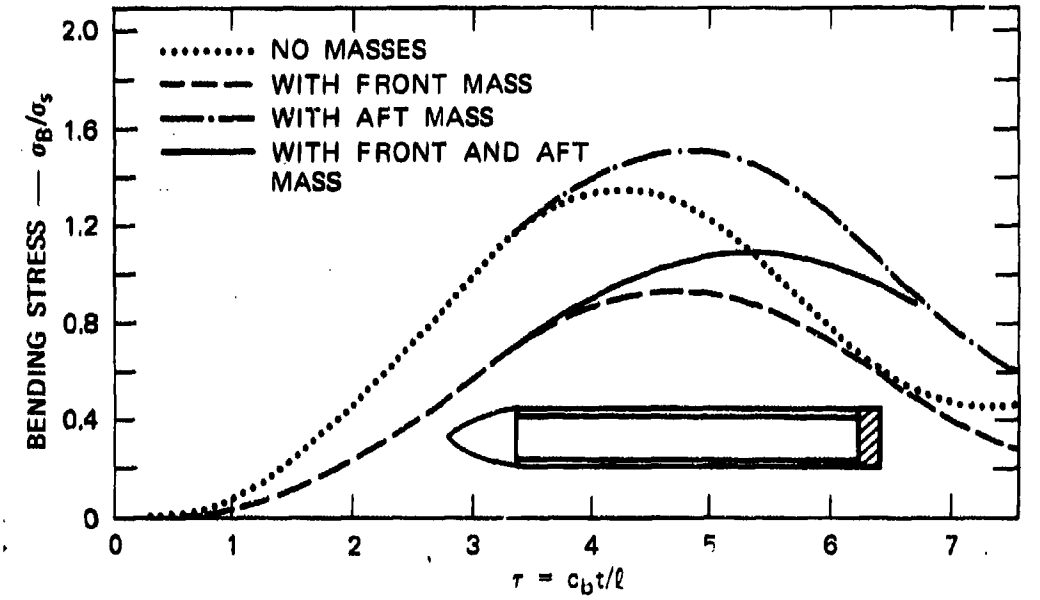

(a) BENDING STRESS HISTORY

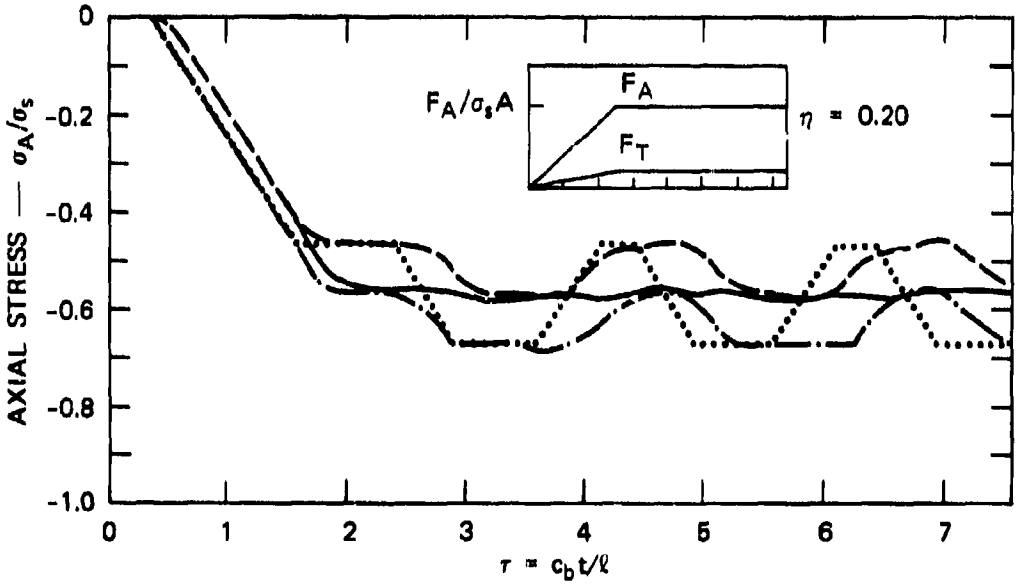

(b) AXIAL STRESS HISTORY

MA-3091-120A

FIGURE 32 STRESS HISTORIES FOR A SIMPLE STEEL TUBE WITH AND WITHOUT END MASSES (AT $\chi = x/\ell = 0.4138$; $\ell/d = 6$, $a/h = 4$)

a structure with a front mass, the lateral load F_L is applied through the center of gravity of the front mass. For a structure without a front mass, the lateral load is applied at the front end of the hollow section.

The predicted bending and axial stress histories at Station $\chi = x/\ell = 0.4138$ are shown in Figure 32(a) and (b). This station is the location of maximum bending stress for the structure without end masses. The locations of maximum bending stress for the other cases are $\chi = 0.3793$ with the front mass $\chi = 0.4483$ with aft mass, and $\chi = 0.4138$ with both masses. These are adjacent locations on the finite difference grid for the structure. Thus, the presence of end masses has virtually no effect on the location of the maximum bending stress.

The magnitude of the peak bending stress, however, is affected by the end masses. There is a 31 percent reduction when the front mass is included, a 12 percent increase when the aft mass is included, and a 19 percent reduction when both masses are included. Including either the front or aft mass increases the time at which the peak response occurs by about 14 percent. Including both masses increases this time by about 28 percent.

Similarly, for the axial stress, there is a 14 percent reduction in peak stress when the front mass is included, an insignificant change in peak stress when the aft mass is included, and about a 14 percent reduction in peak stress when both masses are included. A reduction of about 14 percent in frequency of response occurs with inclusion of the front or aft mass; inclusion of both masses practically eliminates the stress oscillations.

Thus, we conclude that inclusion of the front mass reduces the peak axial and bending stresses, inclusion of the aft mass increases the bending stress, and inclusion of both masses produces stresses intermediate between these extreme values. Inclusion of either mass increases the time at which the peak stress occurs.

Lateral Payload Inertia

The effect of including the lateral payload inertia was determined by analyzing the structure shown in the inset in Figure 33 with and without the payload. The cylindrical section of the casing is made of steel of density 0.281 lb/in^3 (7773 kg/m^3) and is geometrically similar to that of a shallow penetrator. The payload has a density of 0.062 lb/in^3 (1715 kg/m^3) and a mass that is 78 percent of the mass of the cylindrical section. The mass of the front nose is 38 percent of the mass of the cylindrical section. Since the wall of this structure is as thin as a penetrator casing is likely to be made, this configuration emphasizes the effect of the payload lateral inertia.

The calculated bending stress histories shown in Figure 33 are similar with and without the payload. The maximum difference is about 14 percent and occurs at the time of the maximum bending strain.

Further response calculations do not include the effect of lateral payload inertia for two reasons. First, the effect on total strain is small. In an actual penetrator the payload could be made to slide relative to the casing, allowing the nose to decelerate the payload so that the axial component of stress in the casing would not be altered by the payload. Therefore, the effect of the payload on total (bending plus axial) stress is even less (by about a factor of 2) than the effect on bending stress. Second, the critical impact curves of Section 5 are most useful for comparing differences in peak response stress among several structures. The difference in peak response stress from one structure to another is similar with or without the payload.

Nose Rotation

We also determined the rotation of the nose to assess whether deformation of the structure could alter the terradynamics and therefore the load. For the simple tube structure without end masses [Figure 31(a)], the rotation of the front of the structure, relative to its orientation

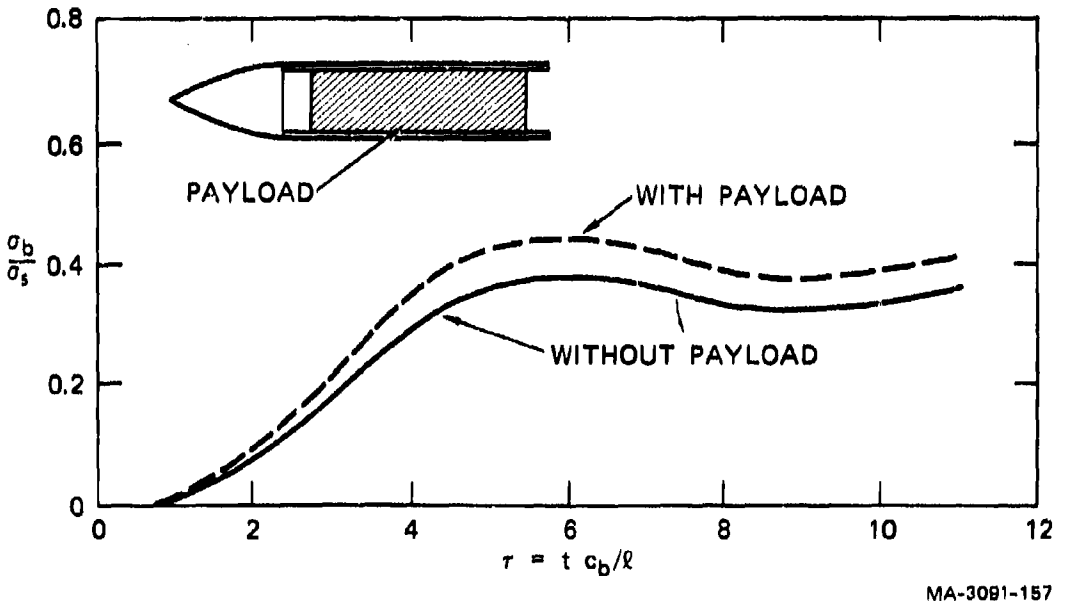

FIGURE 33 BENDING STRAIN AT $\chi = 0.27$ VERSUS TIME FOR A PENETRATOR WITH AND WITHOUT PAYLOAD ($\ell/d = 3.6$, $a/h = 10.0$, $\rho'/\rho = 1.955$, $\tau_r = 5.5$, $\eta = 0.2$)

when the load was applied, is only 0.032 degree at the time peak bending occurs. Thus, it is concluded that during penetration this rotation is not great enough to affect the loading on the nose.

CONCLUSIONS

Comparison of calculated response with that measured in the simulator experiments and in a reverse ballistics test showed that this simple beam-mass theory is sufficient for predicting the strain response in penetrator structures. The parameters that have the largest effect on the peak compressive strain are the eccentricity factor, the rise time, and the end masses.

5 CRITICAL IMPACT CURVES

The analysis was used to calculate the response of penetrator structures ranging from designs for deep penetration (large ℓ/d, small a/h) to those for shallow penetration (small ℓ/d, large a/h). Calculations are also made for penetrators with intermediate values of ℓ/d and a/h.

For design purposes, the most useful information is the relationship between the impact parameters and the response parameters. Then design tradeoffs can be made between the penetrator structure and the impact conditions. For example, for a given penetrator (i.e., a given allowable peak response stress) and a given target, a tradeoff can be made between impact velocity and angle of attack.

The complete impact-response relationship, including terradynamics, is complex and not well understood for many impact conditions. However, the procedure for determining this relationship can be simplified and some insight into the impact-response relationship can be gained by introducing an appropriate set of parameters that describe the loading on the penetrator. The impact-load relationship (from terradynamics) and the load-response relationship (from structural response) can be treated separately and then combined to produce the impact-response relationship sought. Because terradynamics is not well understood we must make reasonable assumptions, based on currently available information, about the impact-load relationship. The load-response relationship can be determined from the structural analysis described in Section 4.

CRITICAL IMPACT CURVES FOR SIMPLE TUBE STRUCTURES

This procedure is illustrated below for the simple tube structure with $\ell/d = 6$ and $a/h = 4$ analyzed in Section 4. The load-response

relationship is discussed first, then the impact-load relationship. These two relationships are combined to produce the impact-response relationship.

Load-Response Relationship

The dominant loading parameters are the rise time τ_r, the peak axial force* F, and the ratio η of lateral load to axial load. The dominant response parameter is the peak compressive stress σ_{max}. The relationship among these parameters can be determined from the results of the calculations of the effects of rise time discussed in Section 3. The results of some of these calculations were given in Figure 31, which shows the bending and axial stress at $\chi = 0.4828$ for $\eta = 0.2$ and for dimensionless rise times $\tau_r = c_b t_r/\ell$ of 0, 0.85, 1.7, 2.55, and 3.4. We first determine the normalized peak response stress as follows. For each rise time and value of η we find σ_{max}, the total compressive stress that is maximum in space and time during the time of interest, and then normalize it with respect to the amplitude of the normal stress σ_s on the loaded end. For example, in Figure 31(b) for $\tau_r = 0$ and $\eta = 0.2$, the maximum value of σ_b/σ_s is 1.51 at $\tau = 3$ and $\chi = 0.4828$ and the maximum value of σ_a/σ_s is 1.0 over a range of values of χ. Thus, the maximum value σ_{max}/σ_s is 2.51 at $\tau = 3$ and $\chi = 0.4828$.

Curves similar to those shown in Figure 31 can also be used to determine σ_{max}/σ_s for different values of η. Since the axial and bending responses are independent, the total stress for different values of η can be computed by weighting the bending component by the appropriate factor. For example, for $\eta = 0.1$, the bending stress shown in Figure 31 (for which $\eta = 0.2$) is multiplied by $0.1/0.2 = 0.5$ before being added to the axial stress.

---

*For the small angles of attack considered here, the amplitude of the axial load F_A is approximated by the amplitude of the load F parallel to the penetrator velocity vector.

The normalized peak response stress as a function of rise time for several values of η are plotted in Figure 34. Note that this load-response relationship applies for any impact conditions that produce the appropriate values of τ_r, F, and η.

Impact-Load Relationship

The dominant impact parameters are the impact velocity V, the angle of attack α, and the target impedance* Z. Thus, the impact-load relationship relates the loading parameters τ_r, F, and η to V, α, and Z. As discussed previously, the first loading parameter, the rise time τ_r, is well approximated by the submersion time of the tapered penetrator nose length ℓ_n:

$$\tau_r = c_b \ell_n / V\ell \tag{9}$$

The dependence of the loading force F on the impact parameters is not as well understood. However, a reasonable approximation is that F is proportional to the impact velocity V,

$$F = b(Z)\ V \tag{10}$$

where the proportionality factor $b(Z)$ depends on the target material. For normal impacts this relationship has been verified both experimentally and theoretically for soil targets; it also appears to hold for rock targets but fewer experimental data are available.†

The dependence of the load ratio η on the impact parameters is complex and has not been adequately investigated. However, some information is available. For normal impacts, that is, for $\alpha = 0$, $\tan^{-1} \eta = 0$. For angle-of-attack impacts, additional information can be inferred from the AVCO reverse ballistics test data and structural calculations shown

*The impedance Z includes any target properties affecting the loading parameters, including moduli, strength, density, and viscosity and frictional coefficients.

†P. F. Hadala, private communication, January 1977.

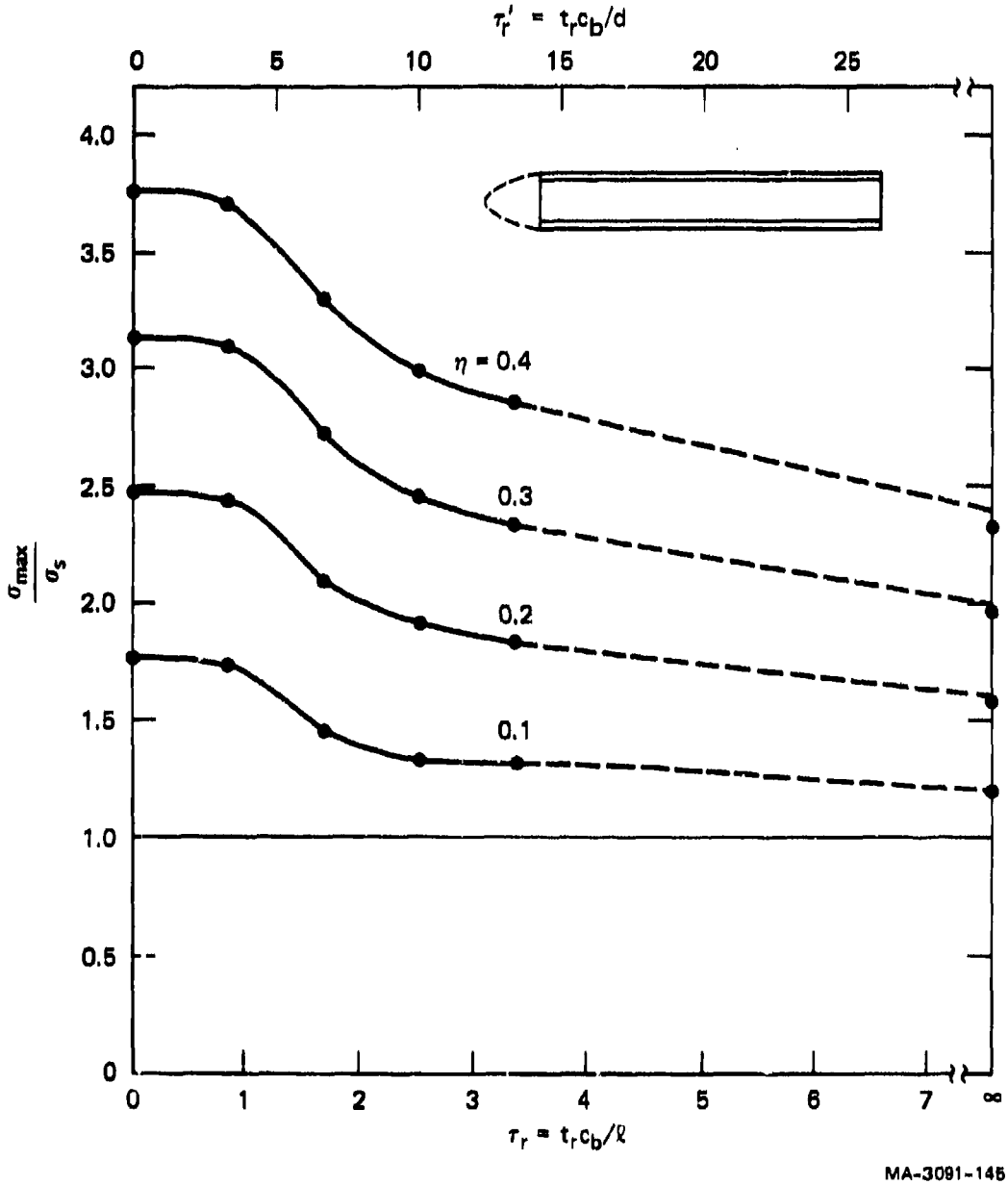

FIGURE 34 DYNAMIC AMPLIFICATION FACTOR VERSUS RISE TIME FOR A SIMPLE STEEL TUBE ($\ell/d = 6$, $a/h = 4$)

in Figure 28. For that test, $\alpha = 5$ degrees and the best agreement between measured and predicted strain was obtained for $\eta = 0.267$ or $\tan^{-1}\eta = 15$ degrees. Thus for this case, $\tan^{-1}\eta = 3\alpha$. We now make the reasonable assumption that the eccentricity angle increases linearly with angle of attack; that is, we assume that

$$\tan^{-1}\eta = 3\alpha \tag{11}$$

over the range of α of interest.

Impact-Response Relationship and Critical Impact Curves

The impact-response relationship is now found by relating the three parameters τ_r, σ_{max}/σ_s, and η in the load-response relationship of Figure 34 with the impact parameters V and α, using equations (9), (10), and (11).

First, τ_r is related to impact velocity by using equation (9). This requires specifying the nose length ℓ_n. Here we have chosen $\ell_n = 1.5d$. Then

$$V = c_b \ell_n / \tau_r \ell \tag{12}$$

Second, σ_{max}/σ_s is related to the impact force F through equation (10). However, so that the results will apply to any targets for which a linear force-velocity relationship is reasonable, we normalize the peak response stress with respect to the average loading pressure $P = F/A'$ at a particular velocity, where A' is the frontal area of the penetrator. For this normalization we choose P_{1000}, the loading pressure generated at an impact velocity of 1000 ft/sec. The peak response stress normalized with respect to P_{1000} is related to the normalized stress of Figure 34 through the identity

$$\frac{\sigma_{max}}{P_{1000}} = \frac{\sigma_{max}}{\sigma_s} \quad \frac{F(V)/A}{F(1000)/A} \tag{13}$$

Substitution of equation (10) into equation (12) and rearrangement gives

$$\frac{\sigma_{max}}{P_{1000}} = \left(\frac{\sigma_{max}}{\sigma_s}\right)\left(\frac{V}{1000}\right)\left(\frac{A'}{A}\right) \qquad (14)$$

where V is in ft/sec. For the simple steel tube, $A'/A = 2.29$.

Finally, the η = constant curves of Figure 34 are relabeled as α = constant curves according to equation (11). The resulting impact-response relationship is shown in Figure 35. Note that although this impact-response relationship relies on two assumptions concerning the impact-load relationship, the load-response relationship involves no such assumptions. Thus when more information about the impact-load relationship is available, the procedure developed here can be repeated with the same load-response relationship.

A more useful form of the impact-response relationship is found by constructing cross plots from Figure 35 for which the normalized peak response stress is constant, as shown in Figure 36. These curves are called critical impact curves and give the tradeoff between impact velocity and angle of attack at the maximum capability of the penetrator. That is, for a given penetrator (fixed σ_{max}) and target (fixed P_{1000}, determined experimentally or analytically), the curve for the appropriate ratio of σ_{max}/P_{1000} gives the combination of allowable values of V and α. For example, for $\sigma_{max}/P_{1000} = 6$, if the penetrator is to survive at angles of attack as large as 5 degrees, the impact velocity must not exceed 1400 ft/sec.

The critical impact curves can also be used to select the penetrator material, on the basis of yield stress, for a given range of V and α within which the penetrator must function. For example, if for a given system and target the maximum impact velocity is 2000 ft/sec and the maximum angle of attack is 5 degrees, a material with a yield strength of at least 10 P_{1000} is needed. In a similar way the critical impact curves of Figure 36 could be used to select targets for which a given system (i.e., specified combinations of σ_y, V, and α) could be used.

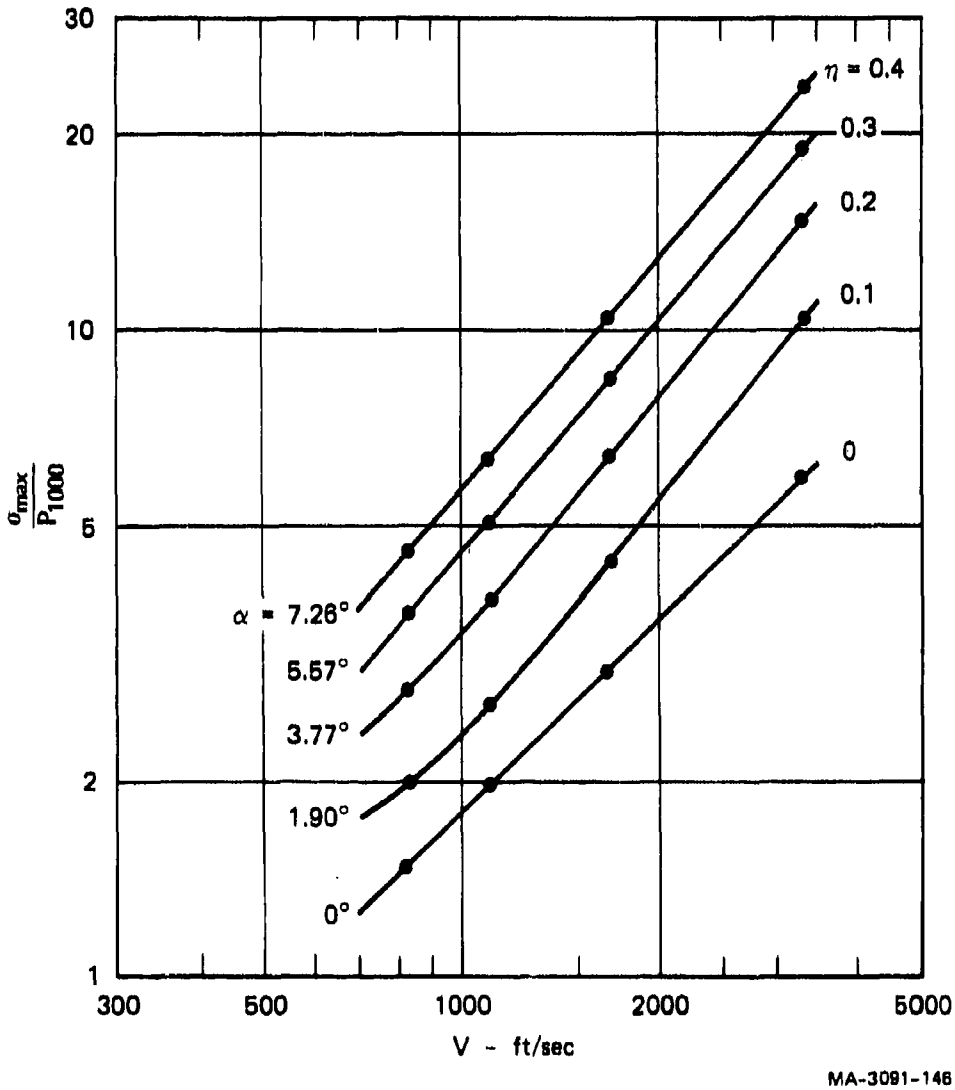

FIGURE 35 PEAK RESPONSE STRESS VERSUS IMPACT VELOCITY FOR A SIMPLE STEEL TUBE (ℓ/d = 6, a/h = 4, ℓ_n = d)

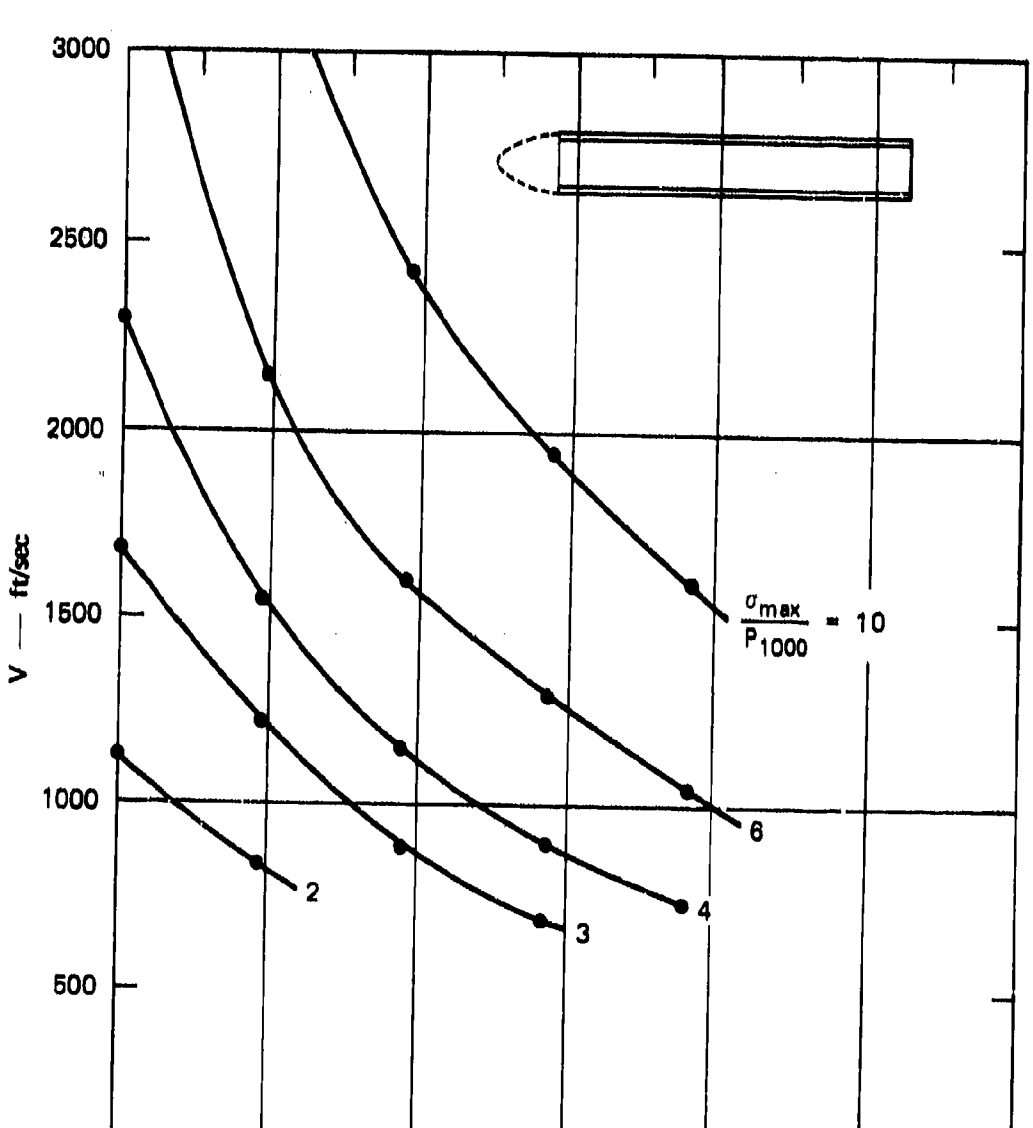

FIGURE 36 IMPACT VELOCITY VERSUS ANGLE OF ATTACK FOR CONSTANT PEAK RESPONSE STRESS IN A SIMPLE STEEL TUBE (ℓ/d = 6, a/h = 4)

Critical impact curves are perhaps most useful for comparing the performance of different penetrator structures. This is illustrated in the next section.

CRITICAL IMPACT CURVES FOR PENETRATOR STRUCTURES

Critical impact curves were developed for the four penetrator structures shown in Figure 37. Structure B is similar to that already used for deep penetration into hard targets. Structure C is similar to that proposed for shallow penetration. Structures A and D were analyzed to determine the effects of changing ℓ/d (along the rows of Figure 37) or a/h (along the columns of Figure 37).

The curves of the normalized peak response stress versus rise time for these four structures, with n as a parameter, are shown in Figures 38 through 41.* Two trends are apparent in these curves. First, for two structures of the same length and outside diameter, the structure with the thicker wall has a greater spread among the curves (compare Figures 38 with 40 and 39 with 41). This is because material added to the inside wall increases the lateral inertia proportionately more than the lateral (bending) stiffness. Thus, the bending stress, and therefore the total stress, is greater for the thicker walled structure. Second, for two structures of the same thickness, the shorter structure has curves with a steeper slope for small τ' and a change in slope at $\tau' \approx 20$ (compare Figure 38 with 39 and 40 with 41). For $\tau' > 20$, the response of the shorter structures is quasi-steady; that is, the peak stress depends on the load amplitude but not the rise time. In contrast, for the rise times considered here, the peak stress in the longer structures depends on both rise time and load amplitude.

---

*Since all four structures have the same diameter, the abscissa coordinate $\tau_r' = c_b t_r/d$ along the top of each graph is on the same scale in all four figures. Thus, we can make direct comparisons of the dependence of the peak response on rise time for the four structures.

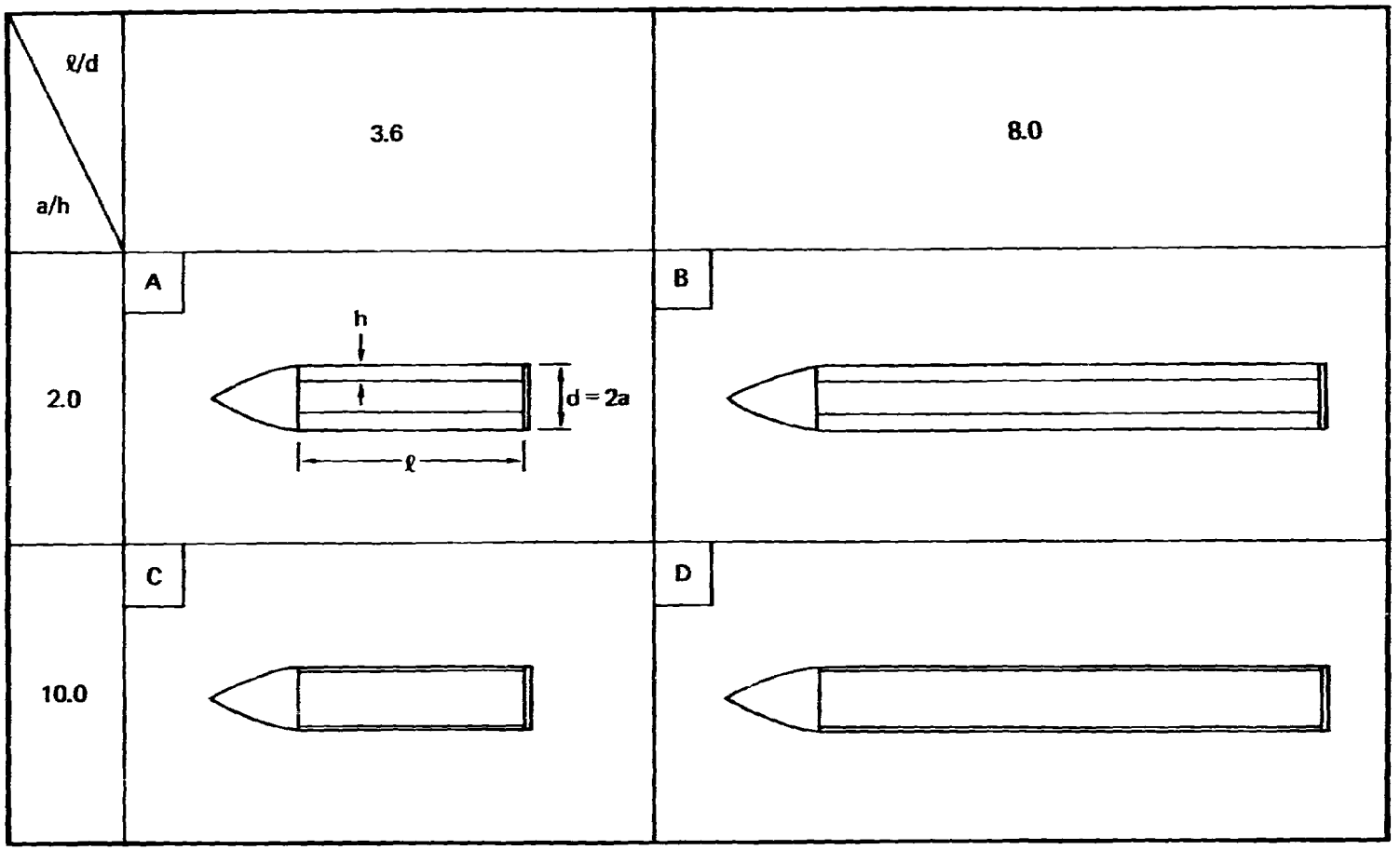

FIGURE 37 PENETRATOR STRUCTURES ANALYZED

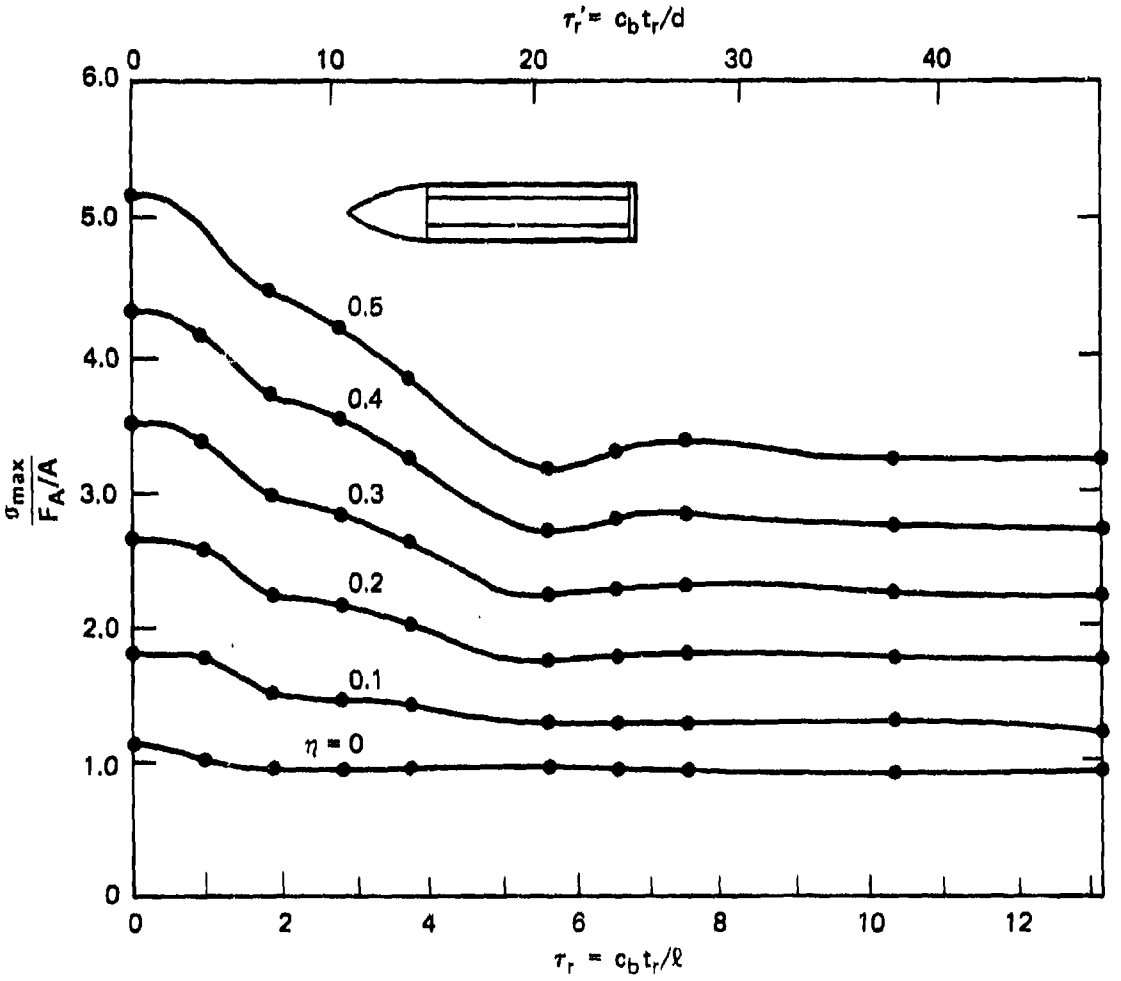

MA-3091-150

FIGURE 38 DYNAMIC AMPLIFICATION FACTOR VERSUS RISE TIME FOR STRUCTURE A (ℓ/d = 3.6, a/h = 2, ℓ_n = 1.5d)

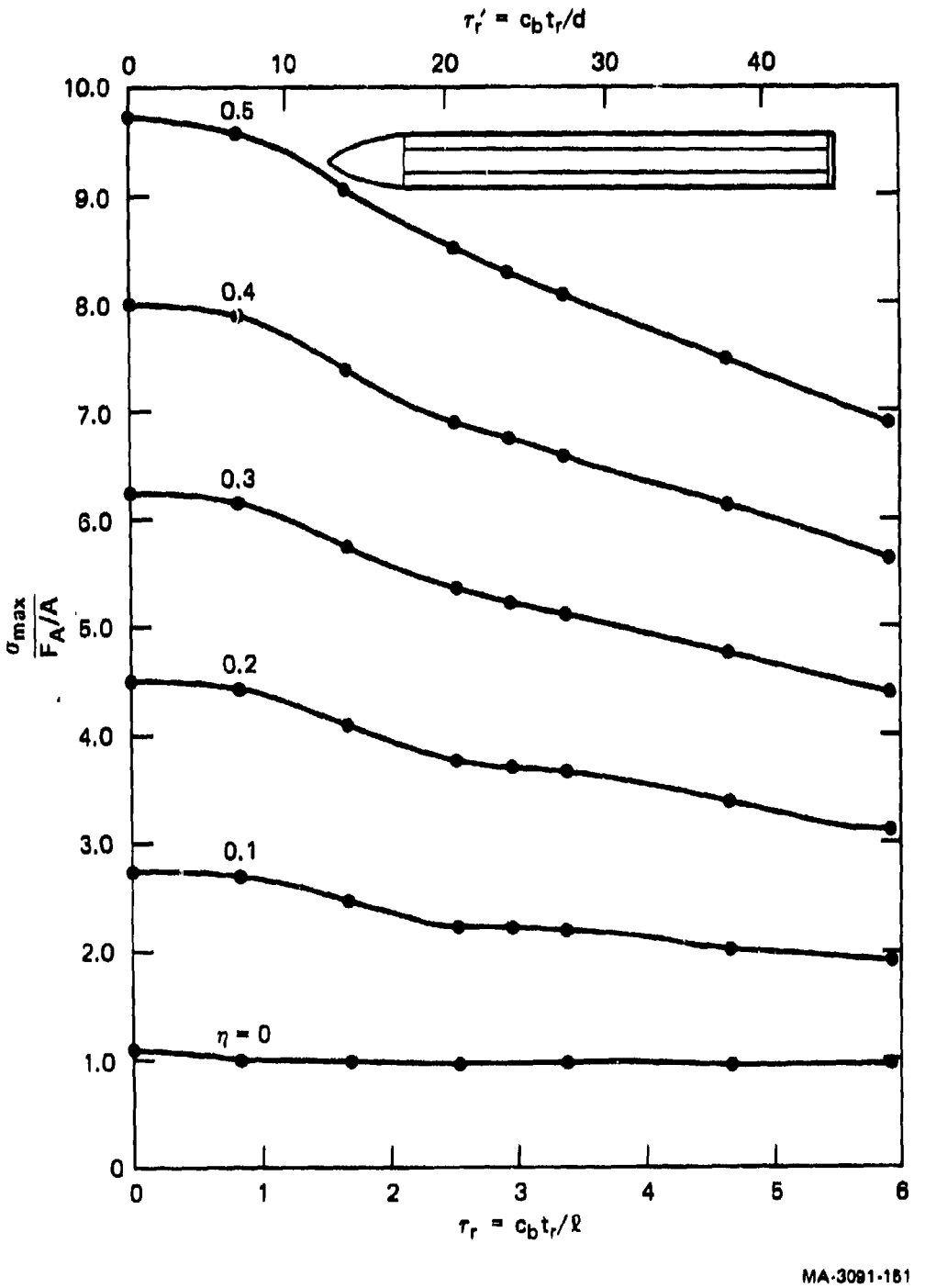

FIGURE 39 DYNAMIC AMPLIFICATION FACTOR VERSUS RISE TIME FOR STRUCTURE B (ℓ/d = 8.0, a/h = 2.0)

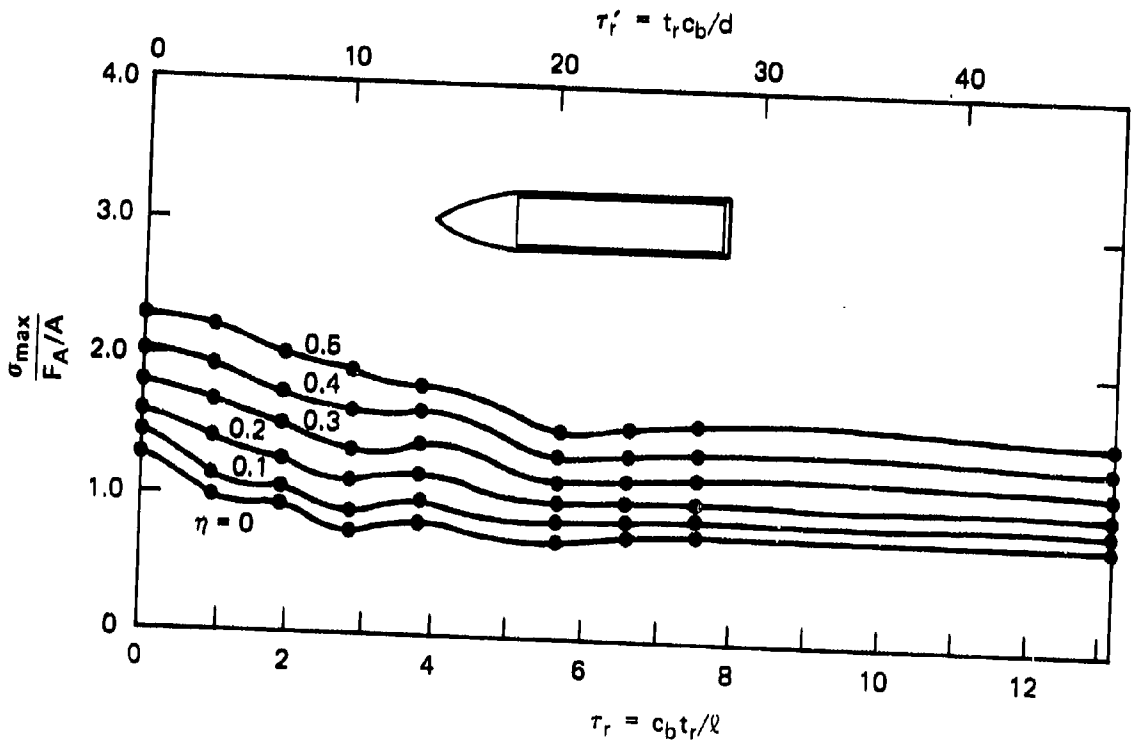

MA-3091-148

FIGURE 40 DYNAMIC AMPLIFICATION FACTOR VERSUS RISE TIME FOR STRUCTURE C (ℓ/d = 3.6, a/h = 10.0, ℓ_n = 1.5d)

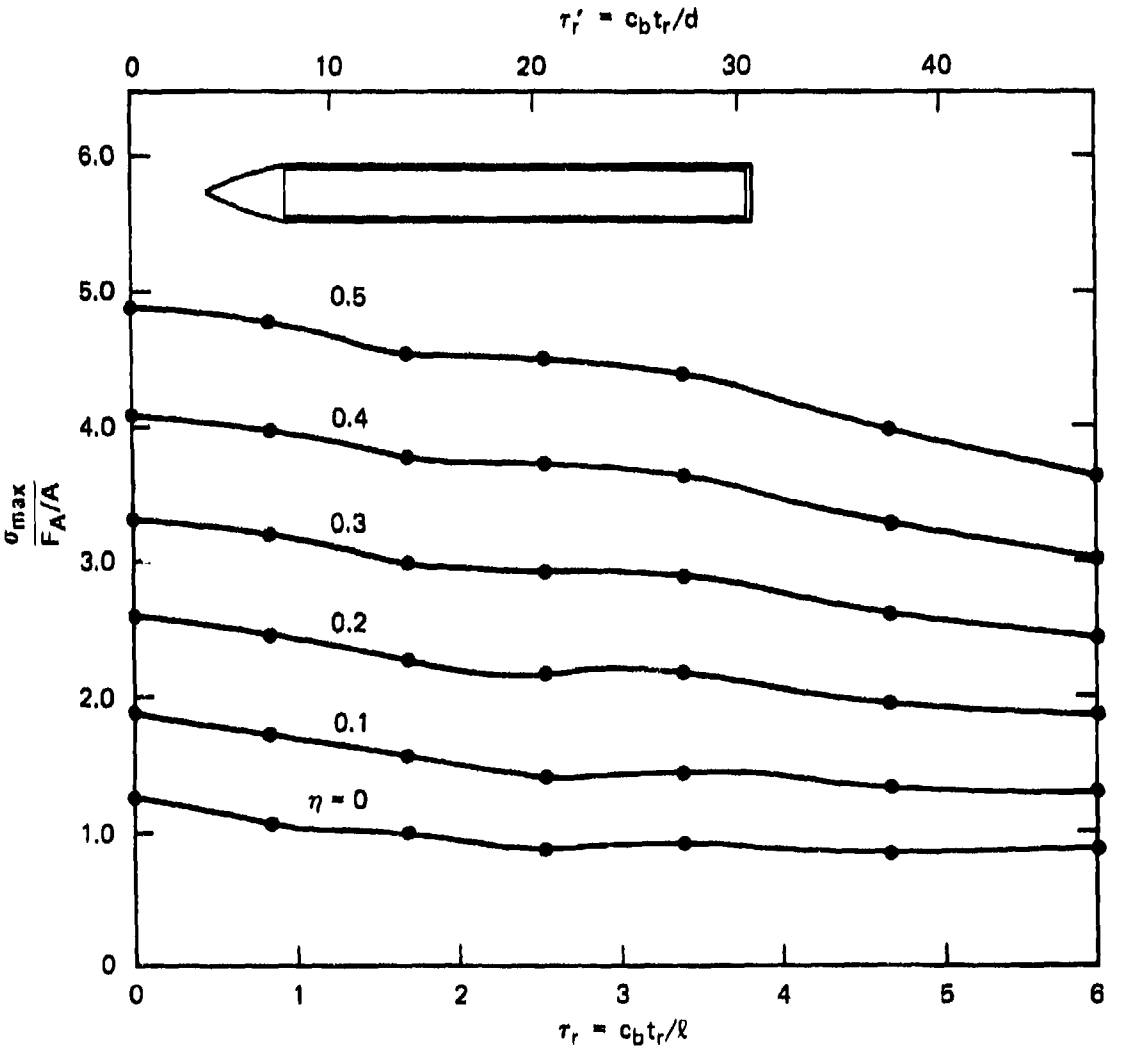

MA-3091-149

FIGURE 41 DYNAMIC AMPLIFICATION FACTOR VERSUS RISE TIME FOR STRUCTURE D (ℓ/d = 8.0, a/h = 10.0, ℓ_n = 1.5d)

The critical load curves for these four structures are shown in Figures 42 through 45.* The trends identified in the previous curves of peak response versus rise time carry over to this set of curves. First, for the thicker-walled structures, the greater spread in the curves of peak response versus rise time give steeper critical impact curves (compare Figure 42 with 44 and 43 with 45). Second, for the shorter structures and for small τ', the steeper slopes of the curves of peak response stress versus rise time give less steep critical impact curves at high velocity (compare Figure 42 with 43 and 44 with 45).

Critical impact curves similar to those in Figures 42 through 45 can be used to plan experiments. For example, the critical load curves for structure B (Figure 43) shows that, for impacts at about 1000 ft/sec and a 2-degree angle of attack, the severity of the response is very sensitive to the angle of attack. Thus it may be important to be able to control the angle of attack in the experiment or at least be able to measure it accurately. In contrast, Structure C (Figure 44) is more sensitive to impact velocity. Thus in testing Structure C it is more important to control or measure impact velocity than angle of attack.

Critical impact curves can also be used to interpret results of experiments or more detailed load and structural response calculations (e.g., a finite element code prediction). A particular experiment or detailed calculation gives a single point on a critical impact curve. Although such a data point represents a more complete response description than for the beam-mass model used here, many points are needed to determine the shape of the curve. The curves calculated with the beam-mass model can be used to determine this shape. Thus the appropriate values of V and α can be selected to minimize the data points

---

*As for the simple steel tube, these curves were generated from curves of σ_{max}/P_{1000} versus V (not shown).

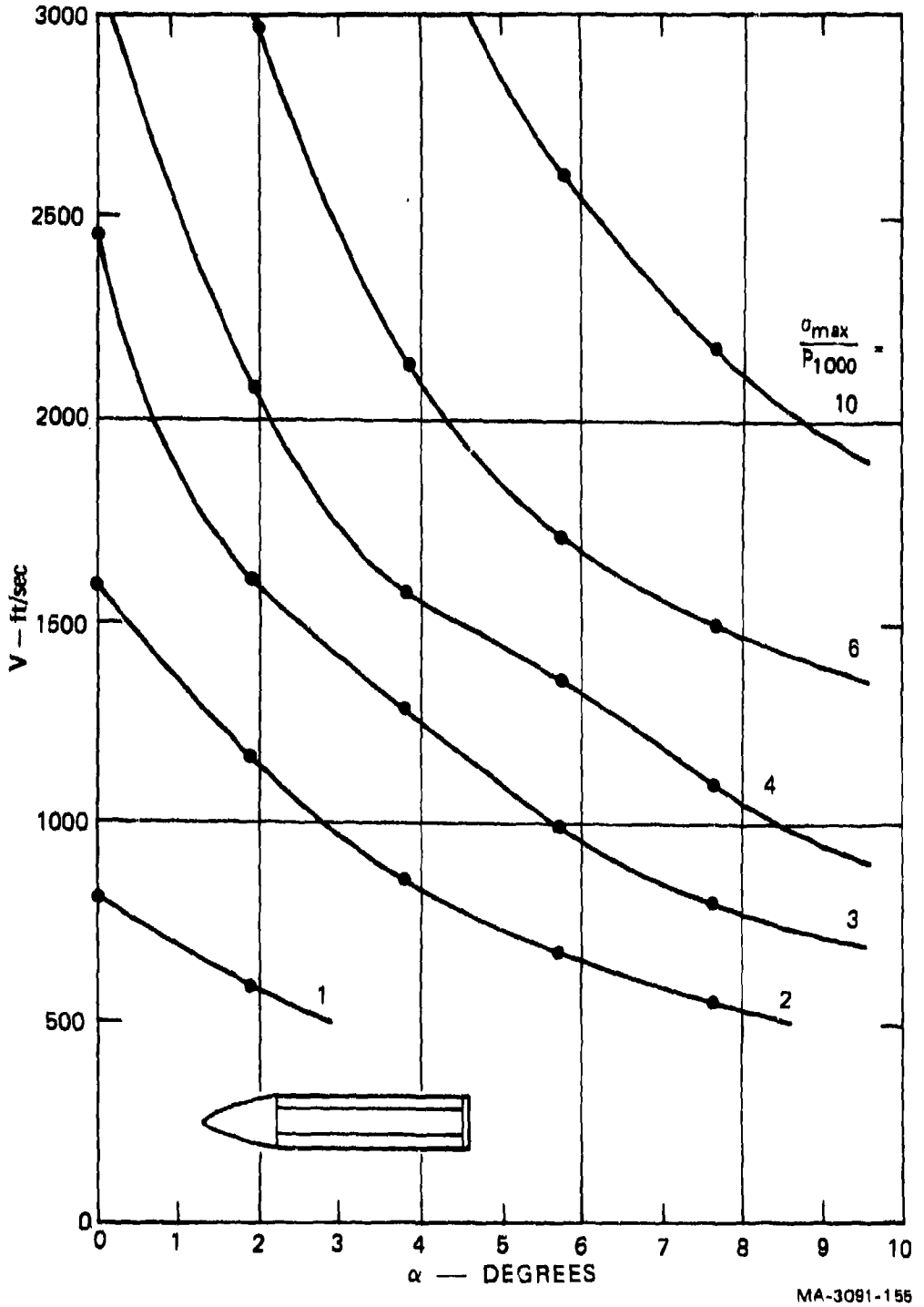

FIGURE 42 IMPACT VELOCITY VERSUS ANGLE OF ATTACK FOR CONSTANT PEAK RESPONSE STRESS IN STRUCTURE A (ℓ/d = 3.6, a/h = 2.0)

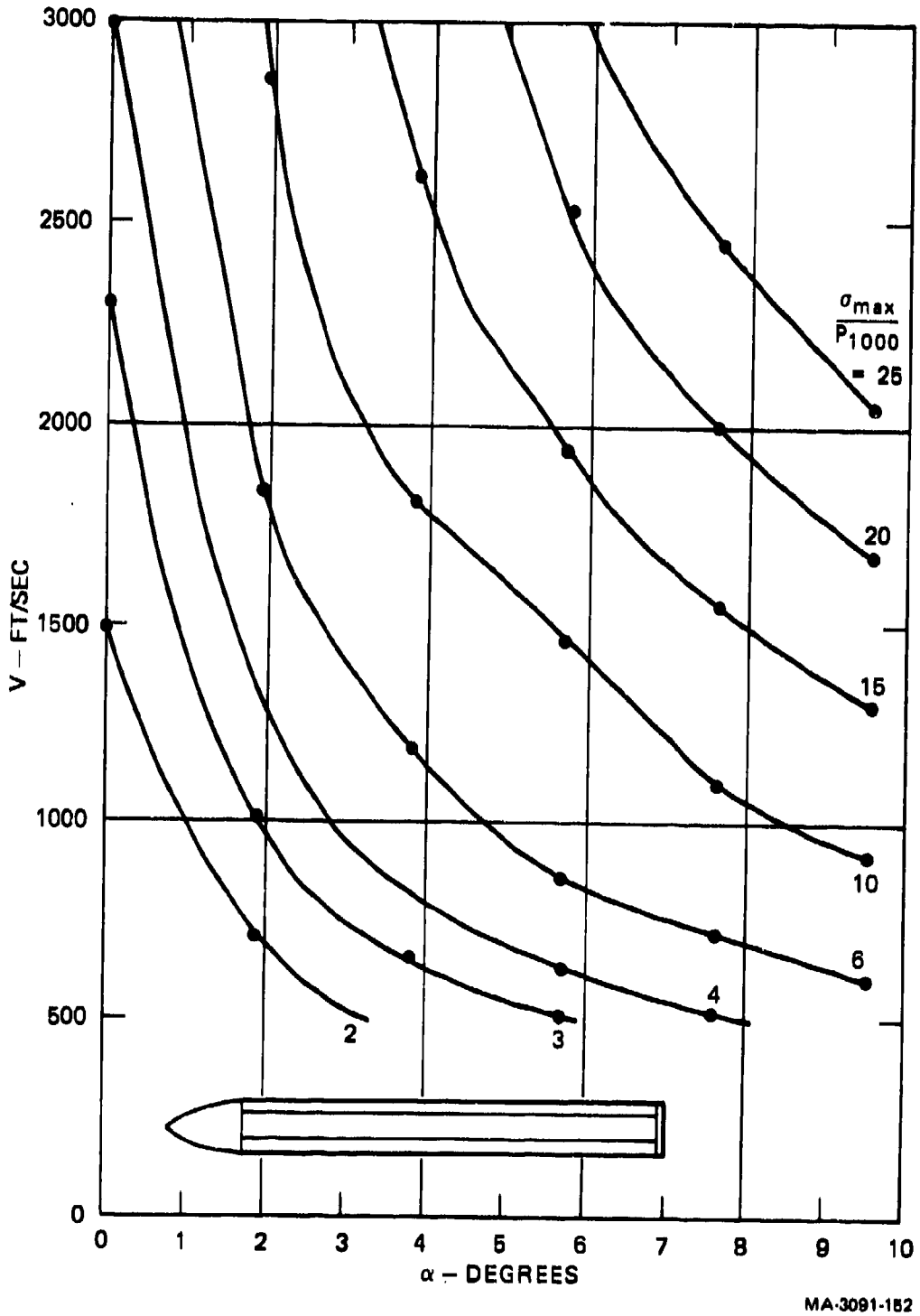

FIGURE 43 IMPACT VELOCITY VERSUS ANGLE OF ATTACK FOR CONSTANT PEAK RESPONSE STRESS IN STRUCTURE B (ℓ/d = 8.0, a/h = 2.0)

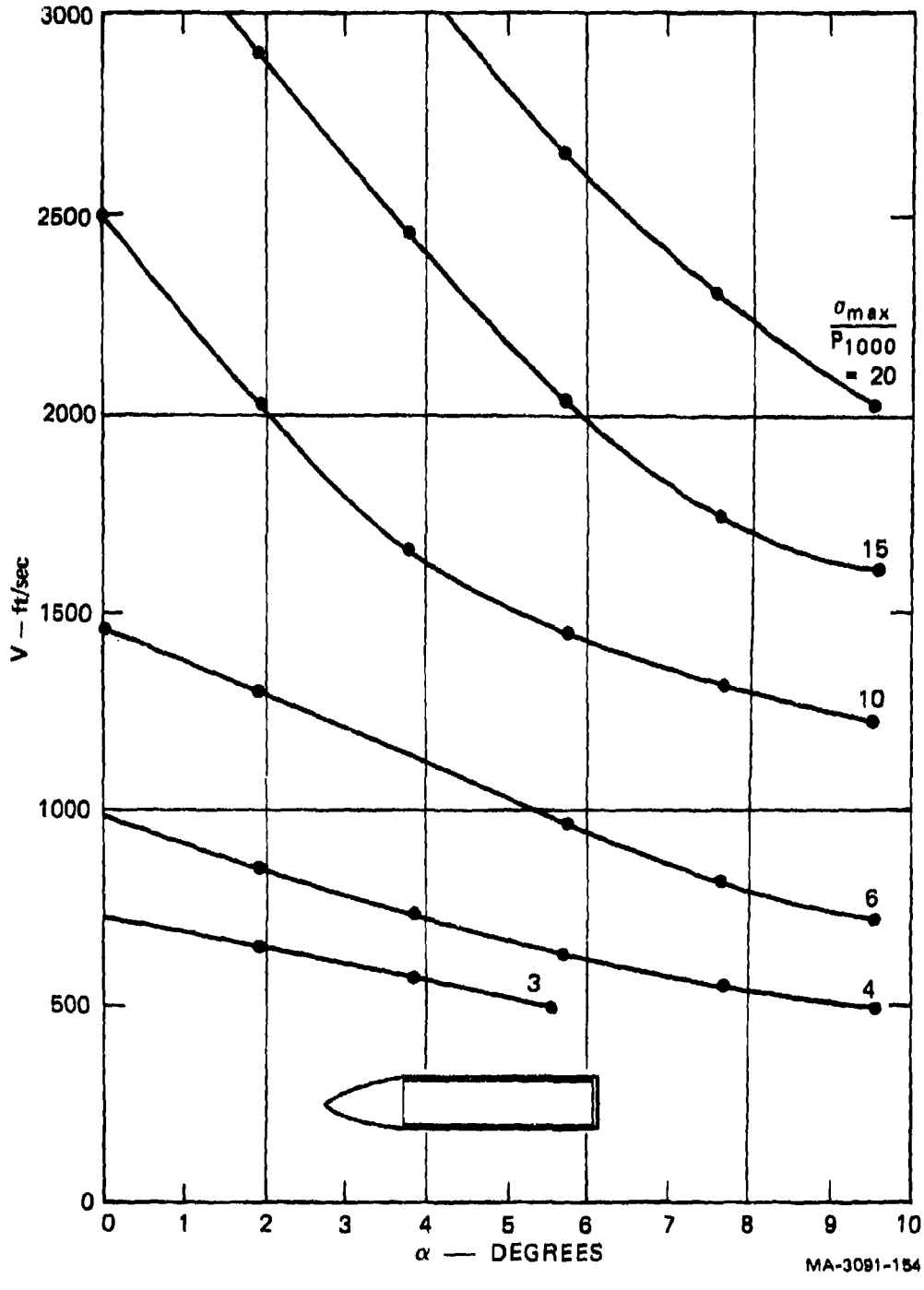

FIGURE 44 IMPACT VELOCITY VERSUS ANGLE OF ATTACK FOR CONSTANT PEAK RESPONSE STRESS IN STRUCTURE C (ℓ/d = 3.6, a/h = 10.0)

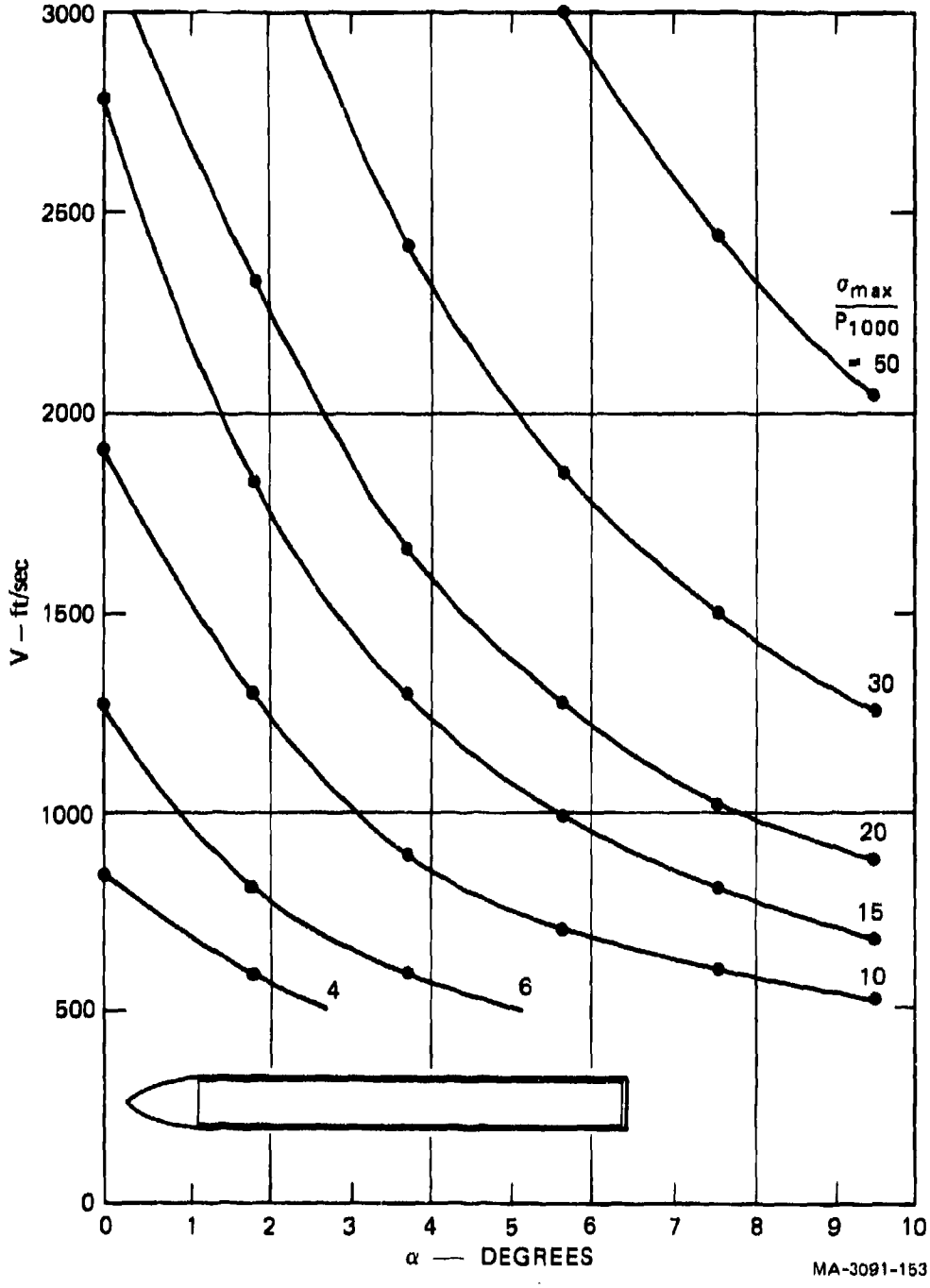

FIGURE 45 IMPACT VELOCITY VERSUS ANGLE OF ATTACK FOR CONSTANT PEAK RESPONSE STRESS IN STRUCTURE D (ℓ/d = 8.0, a/h = 10.0)

needed to define the curve. For example, for Structure B small increments in α and larger increments in V should be made to efficiently define the $\sigma_{max}/P_{1000} = 10$ curve for small α.

The critical impact curves are perhaps most useful for making design tradeoffs among candidate penetrator structures. For example, Figure 46 shows the $\sigma_{max}/P_{1000} = 10$ curves for each of the four structures analyzed. The curves for Structure B (deep penetrator) and for Structure C (shallow penetrator) pass through a similar region in the V-α plane and intersect at V = 1500 ft/sec and α = 5.7 degrees. However, the curve for Structure B (deep penetrator) is steeper and, for small angles of attack, this structure can withstand greater impact velocities. Both these penetrators can be made stronger by increasing only the wall thickness (from that of Structure C to that of Structure A) or by decreasing the length (from that of Structure B to that of Structure A). Note that either of these changes reduces the payload volume. Also, for small angles of attack, the velocity range can be extended more by increasing wall thickness than by decreasing length. Similar conclusions can be drawn by comparing curves for Structures B and C with that of Structure D.

CONCLUSIONS

A method has been developed for characterizing, in terms of critical impact curves, the ability of penetrator structures to withstand impacts. The principal advantage of this procedure is that it characterizes the response over a range of impact conditions. This allows tradeoffs to be made among structural dimensions, yield strength, and target characteristics and allows selection of the best structure from a group of structures for a particular application. Critical impact curves can also be used to plan and interpret experiments and more detailed calculations.

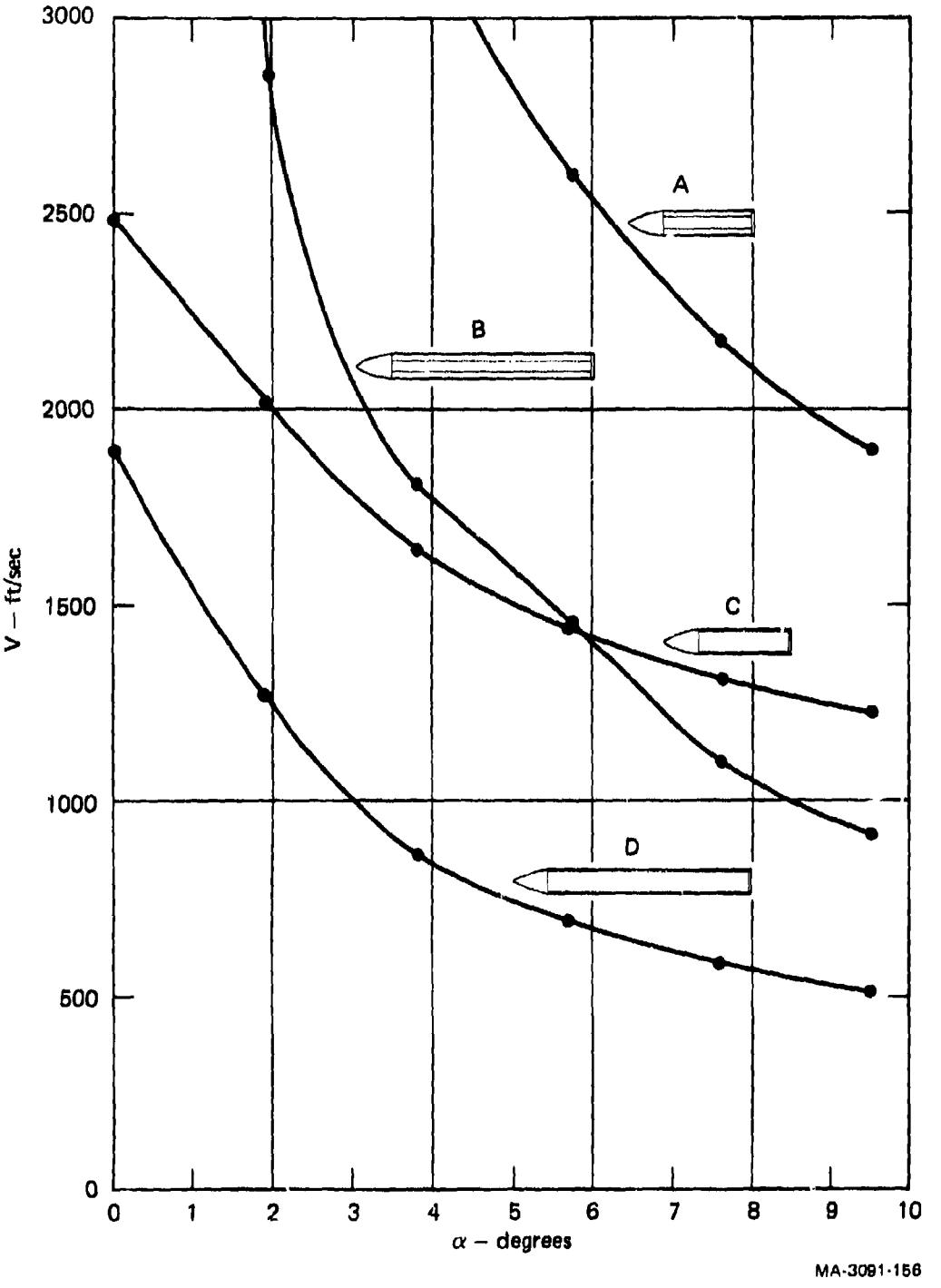

FIGURE 46 IMPACT VELOCITY VERSUS ANGLE OF ATTACK FOR CONSTANT PEAK RESPONSE STRESS FOR DIFFERENT STEEL PENETRATOR STRUCTURES (σ_{max}/P_{1000} = 10)

REFERENCES

1. W. J. Patterson, "DNA/Sandia Soil Penetratiron Experiment at DRES: Results and Analysis," Sandia Laboratories Report SAND-75-0001 (March 1975).

2. P. F. Hadala, "Evaluation of Empirical and Analytical Procedures Used for Predicting the Rigid Body Motion of an Earth Penetrator," Waterways Experiment Station Paper S-75-15 (June 1975).

3. M. H. Wagner, K. N. Kreyenhagen, and W. S. Goerke, "Numerical Analysis of Projectile Impact and Deep Penetration into Earth Media," Waterways Experiment Station Contract Report S-75-4 (August 1975).

4. K. N. Kreyenhagen and Y. M. Ito, "Internal Response in Earth Penetrators," presented at the DNA Earth Penetration Technology Review Meeting (October 1975).

5. D. Henderson et al., "Impact and Penetration Technology," Progress Report No. 2 under Contract DNA-75-C-0181 AVCO Corporation, (June 1975).

6. M. Anthony, Martin Marietta Aerospace Company, "Impact of Earth Penetrator Models into Simulated Rock Targets," presented at the DNA Earth Penetration Technology Review Meeting (October 1975).

7. J. D. Colton, "Multiple Fracture of Beams and Plates Under Localized Impulsive Loading," Poulter Laboratory Technical Report No. 004-73, Stanford Research Institute (November 1973).

8. D. J. Cagliostro, "Experiments on the Response of Hexagonal Subassembly Ducts to Radial Loads," SRI Interim Report for Argonne National Laboratory (August 1975).

Appendix A

EXPERIMENTAL DATA

Tables A-1 through A-4 give the experimental data measured under under this contract.

Table A-1

CALIBRATION TESTS WITHOUT MODEL PENETRATOR

Test No.	Date	Charge Mass[a] (gm)	Initial Piston Disp. (cm)	Vent Holes	Peak Pressure[b] (kPa)	Peak Acc. (gm)	Rise Time[c] (μsec)
1	3-12-76	0.66[d]	0.193		5,790	-[e]	-[e]
2	3-15-76	0.66[d]	0.193		6,070	1,700	100
3	3-26-76	0.543	0.457	f	4,140	1,050	180
4	3-26-76	0.543	0.457		3,650	850	170
5	3-29-76	1.086	0.457		7,760	2,000	150
6	3-29-76	1.086	0.457		7,760	2,400	110
7	3-30-76	1.086	0.457		7,070	1,800	135
8	3-30-76	2.00	0.457	g	14,130	4,000	120
9	3-30-76	2.00	0.762		11,720	3,600	240
10	4-02-76	1.00	0.305		7,450	2,000	145
11	4-02-76	1.00	0.152		10,340	2,650	115

[a] For tests 3 through 11, a small (0.02 to 0.05 gram) booster charge (Du Pont Detasheet) was used; the mass listed here includes that of 90/10 PTEN/microsphere charge only.

[b] Average of the two pressure gage measurements.

[c] Time to reach 75% of the peak acceleration.

[d] Includes large (approximately 0.18 gram) booster charge (Du Pont Detasheet).

[e] Bad gage record.

[f] Vent hole configuration: top pair open; middle pair open; bottom pair closed.

[g] Vent hole configuration: top pair open; middle pair closed; bottom pair closed.

Table A-2

CALIBRATION TESTS WITH LONG ROD

Test No.	Date	Device Setup[a] Charge Mass[b] (gm)	Device Setup[a] Initial Piston Displacement (cm)	Peak Pressure[c] (kPa)	Peak Strain at Aft Station[d] (%)	Remarks
12	4-06-76	1.00	0.152	--	--	Detonator misfired.
13	4-07-76	1.00	0.152	11,200	0.021[e]	
14	4-15-76	1.00	0.152	--	--	Detonator misfired.
15	4-15-76	1.00	0.152	--	--	Detonator misfired.
16	4-16-76	1.00	0.152	11,000	0.020	
17	4-16-76	1.00	0.081	--	--	Detonator misfired.
18	4-16-76	1.00	0.081	12,400	0.021	
19	4-19-76	1.00	0.081	13,800	0.027	
20	4-19-76	1.00	0.081	13,800	0.027	
21	4-20-76	3.00	0.094	43,400	0.103[f]	
22	4-21-76	3.00	0.094	--	--	Detonator misfired.
23	4-21-76	3.00	0.094	46,100	0.090	
24	5-13-76	3.00	0.094	48,900	0.089	
25	5-13-76	3.00	0.094	46,500	0.087	
26	5-14-76	3.00	0.305	34,500	0.053	Special end condition tested.
27[a]	5-27-76	1.00	0.094	12,200	0.020[g]	15.2-cm-radius loaded end.
28	5-28-76	1.00	0.094	10,700	0.014	Load cell tested.
29	6-23-76	1.00	0.152	--	--	No gage records.
30	6-23-76	1.00	0.152	9,100	0.016	Load cell tested.

[a] Additional device setup parameters for Tests 12 through 30:
Vent hole configuration: top pair open; middle pair open; bottom pair closed, except for Test 27 where all three pairs were open.

Orifice Area: 1.455 cm^2

[b] For Tests 12 through 30, a small (0.02 to 0.06 gram booster charge (Du Pont Detasheet) was used; the mass listed here includes that of 90/10 PETN/microsphere charge only.

[c] Average of the two pressure gage measurements.

[d] Average of three or four gages from aft station (except as noted).

[e] Gage 5 only.

[f] Gage 1 only.

[g] Average of Gages 1, 2, and 3.

Table A-3

MODEL STRUCTURE TESTS

Test No.[a]	Date	Model Penetrator[b]	Initial Angle [degree (rad)]	Peak Load[c] (kN)	Strains at Aft Station (%) Bending[d]	Strains at Aft Station (%) Peak Axial[e]
31[a]	6-24-76	SS	Normal	90[f]	--	0.022[g]
35	7-20-76	SS	Normal	89.0	--	0.018
36	7-22-76	SS	Normal	89.0	--	0.018
37	7-22-76	SS	Normal	77.8	--	0.015
32	7-07-76	SS	4° (0.07)	73.4	0.006	0.016
34	7-09-76	SS	5° (0.09)	71.2	0.015	0.015
33	7-08-76	SS	8° (0.14)	75.6	0.018	0.017
38	8-03-76	TkW	Normal	89.0	--	0.029
39	8-03-76	TkW	Normal	66.7	--	--[h]
40	8-04-76	TkW	Normal	73.4	--	0.027
41	8-04-76	TkW	Normal	75.6	--	0.025
43	8-06-76	TkW	7°10' (0.125)	71.2	0.016	0.023
42	8-05-76	TkW	7°20' (0.128)	70[f]	0.020	0.021
45	8-17-76	TkW	8°30' (0.148)	89.0	0.022	0.028
44	8-16-76	TkW	8°45' (0.153)	62.3	0.020	0.020
47	8-19-76	TA1	Normal	46.7	--	0.030
49	8-20-76	TA1	6°10' (0.108)	35.6	--	--[i]
46	8-18-76	TA1	6°15' (0.109)	44.5	0.005	0.027
48	8-20-76	TA1	7°0' (0.122)	51.2	0.008	0.032

[a]Device setup parameters for Tests 31 through 49:
Vent hole configuration: top pair open; middle pair open; bottom pair closed.
Charge mass: 2.00 gram 90/10 PETN/microsphere charge. No booster charge was used except in Test 31 where a 0.03-gram patch of Du Pont Detasheet was used in addition to the 2.00-gram 90/10 charge.
Initial piston displacement: 0.152 cm.
Orifice area: 1.455 cm^2.

[b]Abbreviations: SS--solid steel model; TkW--thicked-walled model; TA1--tapered aluminum model.

[c]Peak vertical load measured with load cell.

[d]Bending strain at time of peak axial strain (average magnitude of two gages).

[e]Average of four gages.

[f]Determined from pressure record.

[g]Average of three gages.

[h]Test incorrectly set up.

[i]Bad gage records.

Table A-4

MODEL STRUCTURE TESTS WITH PHOTOGRAPHY

Test No.	Date	Model Penetrator[a]	Initial Angle [degree (rad)]	Device Setup[b] Charge Mass[c] (gm)	Initial Piston Displacement (cm)	Orifice Area (cm^2)	Peak Load[d] (kN)	Load Ratio F_H/F_V	Strains at Aft Station (%) Bending[e]	Axial[f]	Remarks
50	9-24-76	SS	Normal	2.00	0.152	1.455	122.3	0.007			Measures precision of load ratio measurements.
56	10-08-76	SS	7° (0.12)	2.00	0.152	1.455	57.8	0.087			Pulse arrested after 300 μsec.
58	10-11-76	SS	7° (0.12)	2.00	0.152	1.455	73.4	0.096			Pulse arrested after 350 μsec.
60	10-12-76	SS	7° (0.12)	2.00	0.152	1.455	80.1	0.064	[g]		Pulse arrested after 500 μsec.
51	9-27-76	SS	7-1/2° (0.13)	2.00	0.152	1.455	82.3	0.080			
52	9-28-76	SS	7-1/2° (0.13)	2.00	0.152	1.455	80.1	0.079			
59	10-12-76	SS	7-1/2° (0.13)	2.00	0.152	1.455	77.8	0.074			Pulse arrested after 500 μsec.
57	10-08-76	SAl	7°30' (0.131)	3.00	0.152	1.455	117.9	0.095			Pulse arrested after 250 μsec.
53	9-28-76	TkW	7°5' (0.124)	2.00	0	1.455	51.2	--[h]	0.010	0.018	
54	9-30-76	TkW	7°35' (0.132)	2.00	0.076	1.455	77.8	--[h]	0.012	0.029	
65	10-29-76	TkW	17°0' (0.297)	1.50	0.152	5.820	60.1	0.159	0.043	0.023	
62	10-27-76	TkW	17°50' (0.311)	1.50	0.152	5.820	55.6	0.119	--[i]		
63	10-28-76	TkW	19°25' (0.339)	1.50	0.152	5.820	--[i]	0.080	--[i]		
64	10-28-76	TkW	19°30' (0.340)	1.50	0.152	5.820	66.7	0.141	0.042	0.022	
61	10-26-76	TnW	6-1/2° (0.11)	4.00	0.152	5.820	113.4	0.026	0.014	0.051	
55	9-30-76	TnW	8°10' (0.143)	2.00	0.076	1.455	48.9	--[h]	0.004	0.019	
66	10-29-76	TnW	18°15' (0.319)	1.50	0.152	5.820	50.0	0.074	0.015	0.023	

[a] Abbreviations: SS--solid steel model; TkW--thick-walled model; SAl--solid aluminum model; TnW--thin-walled model.

[b] Vent hole configuration: Top pair open; middle pair open; bottom pair closed (Tests 50 through 66).

[c] Mass of 90/10 PETN/microsphere charge. No booster charges used in Tests 50 through 66.

[d] Peak vertical load measured with load cell.

[e] Bending strain at time of peak axial strain (average magnitude of two gages).

[f] Average of four gages.

[g] Strains not measured.

[h] High-speed photography not used.

[i] Bad gage records.

Appendix B

SOLUTION OF EQUATIONS FOR BEAM WITH END MASSES

Referring to Figure 21, the finite difference form of the equations for the front end are

$$N_A - N_B + \rho c_b A\left(V_A - V_B\right) = 0 \tag{1}$$

$$M_A - M_B - \rho c_b I\left(\omega_A - \omega_B\right) = -c_b\left(\frac{Q_A + Q_B}{2}\right)\Delta t \tag{2}$$

$$Q_A - Q_C + \rho A c_s\left(W_A - W_C\right) = -\rho c_s^2\left(\frac{\omega_A + \omega_C}{2}\right)\Delta t \tag{3}$$

$$F_A + N_A = m_f\left(\frac{V_A - V_D}{2\Delta t}\right) \tag{4}$$

$$-F_L + Q_A = m_f\left(\frac{W_A - W_D}{2\Delta t}\right) \tag{5}$$

$$-M_A + Q_A \ell_0 = I_f\left(\frac{\omega_A - \omega_D}{2\Delta t}\right) \quad . \tag{6}$$

Let

$$\beta = \frac{c_s}{c_b} \quad .$$

Then, interpolating

$$Q_C = \frac{1}{2}\,(1 - \beta)\left(Q_A + Q_D\right) + \beta Q_B$$

for values at point c,

$$W_C = \frac{1}{2}\,(1 - \beta)\left(W_A + W_D\right) + \beta W_B$$

$$\omega_C = \frac{1}{2}\,(1 - \beta)\left(\omega_A + \omega_D\right) + \beta \omega_B \quad .$$

Let

$$K_A = \sqrt{\frac{I}{A}} \quad .$$

Introduce nondimensional variables

$$\bar{N}_A = \frac{N_A}{\rho A c_b^2} \qquad \bar{N}_B = \frac{N_B}{\rho A c_b^2}$$

$$\bar{V}_A = \frac{V_A}{c_b} \qquad \bar{V}_B = \frac{V_B}{c_b} \qquad \bar{V}_D = \frac{V_D}{c_b}$$

$$\bar{M}_A = \frac{M_A K_A}{\rho I c_b^2} \qquad \bar{M}_B = \frac{M_B K_A}{\rho I c_b^2}$$

$$\bar{Q}_A = \frac{Q_A}{\rho A c_s^2} \qquad \bar{Q}_B = \frac{Q_B}{\rho A c_s^2}$$

$$\bar{W}_A = \frac{W_A}{c_b} \qquad \bar{W}_D = \frac{W_D}{c_b}$$

$$\bar{\omega}_A = \frac{\omega_A K_A}{c_b} \qquad \bar{\omega}_D = \frac{\omega_D K_A}{c_b}$$

$$\bar{F}_A = \frac{F_A}{\rho A c_b^2} \qquad \bar{F}_L = \frac{F_L}{\rho A c_b^2}$$

$$\Delta\tau = \frac{\Delta t c_b}{K_A}$$

Define the following constants:

$$\gamma = \frac{\Delta\tau}{2}$$

$$\alpha_1 = \frac{m_f}{\rho A K_A}$$

$$\alpha_2 = \frac{\ell_Q}{K_A}$$

$$\alpha_3 = \frac{I_f}{\rho I K_A}$$

$$b_1 = -\alpha_3 - 4\gamma$$

$$b_2 = 4\beta^2\gamma(\alpha_2 + \gamma)/b_1 - (1 + \beta)/[\gamma(3 - \beta)]$$

$$b_3 = (1 + \beta)/[\beta\gamma(3 - \beta)]$$

$$b_4 = \alpha_1 b_2 - 4\beta^2\gamma b_3$$

$$C_1 = \left[4\gamma\left(\bar{M}_B - \bar{\omega}_B - \beta^2\gamma\bar{Q}_B\right) - \alpha_3\bar{\omega}_D\right]/b_1$$

$$-\left[(1 - \beta)\left(\bar{Q}_D + \bar{W}_D/\beta - \gamma\bar{\omega}_D\right) + 2\beta\left(\bar{Q}_B + \bar{W}_B/\beta - \gamma\bar{\omega}_B\right)\right]/[\gamma(3 - \beta)] \quad .$$

The solution to Eqs. (1)-(6) in terms of dimensionless quantities is:

$$\bar{N}_A = \left[\alpha_1\left(\bar{N}_B + \bar{V}_B - \bar{V}_D\right) - 4\gamma\bar{F}_A\right]/\left(\alpha_1 + 4\gamma\right)$$

$$\bar{V}_A = \bar{N}_B - \bar{N}_A + \bar{V}_B$$

$$\bar{Q}_A = \left(\alpha_1 C_1 + \alpha_1 b_3\bar{W}_D - 4\gamma b_3\bar{F}_L\right)/b_4$$

$$\bar{W}_A = \left(b_2\bar{Q}_A - C_1\right)/b_3$$

$$\bar{\omega}_A = \left\{-\alpha_3\bar{\omega}_D + 4\gamma\left[\bar{M}_B - \bar{\omega}_B - \beta^2\gamma\bar{Q}_B - \beta^2\left(\alpha_2 + \gamma\right)\bar{Q}_A\right]\right\}/b_1$$

$$\bar{M}_A = \beta^2\alpha_2\bar{Q}_A - \alpha_3\left(\bar{\omega}_A - \bar{\omega}_D\right)/(4\gamma) \quad .$$

Similarly, the equations for the rear end of the beam are

$$N_Z - N_X - \rho c_b A_Z\left(V_Z - V_X\right) = 0 \tag{7}$$

$$M_Z - M_X + \rho I_Z c_b\left(\omega_Z - \omega_X\right) = c_b\left(\frac{Q_Z + Q_X}{2}\right)\Delta t \tag{8}$$

$$Q_Z - Q_Y - \rho A_Z c_s \left(W_Z - W_Y\right) = -\rho c_s^2 A_Z \left(\frac{\omega_Z + \omega_Y}{2}\right)\Delta t \tag{9}$$

$$-N_Z = m_a \left(\frac{V_Z - V_W}{2\Delta t}\right) \tag{10}$$

$$-Q_Z = m_a \left(\frac{W_Z - W_W}{2\Delta t}\right) \tag{11}$$

$$M_Z + Q_Z \ell_2 = I_a \left(\frac{\omega_Z - \omega_W}{2\Delta t}\right) \quad . \tag{12}$$

Again, let

$$\beta = \frac{c_s}{c_b}$$

so that

$$Q_Y = \frac{1}{2}\ (1 - \beta)\left(Q_Z + Q_W\right) + \beta Q_X$$

$$W_Y = \frac{1}{2}\ (1 - \beta)\left(W_Z + W_W\right) + \beta W_X$$

$$\omega_Y = \frac{1}{2}\ (1 - \beta)\left(\omega_Z + \omega_W\right) + \beta \omega_X \quad .$$

Let

$$K_Z = \sqrt{\frac{I}{A}} \quad .$$

Introduce the dimensionless quantities:

$$\overline{N}_Z = \frac{N_Z}{\rho A c_b^2} \qquad \overline{N}_X = \frac{N_X}{\rho A c_b^2}$$

$$\overline{V}_Z = \frac{V_Z}{c_b} \qquad \overline{V}_X = \frac{V_X}{c_b} \qquad \overline{V}_W = \frac{V_W}{c_b}$$

$$\overline{M}_Z = \frac{M_Z K_Z}{\rho I c_b^2} \qquad \overline{M}_X = \frac{M_X K_Z}{\rho I c_b^2}$$

$$\bar{Q}_Z = \frac{Q_Z}{\rho A c_s^2} \qquad \bar{Q}_X = \frac{Q_X}{\rho A c_s^2}$$

$$\bar{W}_Z = \frac{W_Z}{c_b} \qquad \bar{W}_W = \frac{W_W}{c_b}$$

$$\bar{\omega}_Z = \frac{\omega_Z K_Z}{c_b} \qquad \bar{\omega}_W = \frac{\omega_W K_Z}{c_b}$$

$$\Delta\tau = \frac{\Delta t c_b}{K_Z}$$

Define:

$$\gamma = \frac{\Delta\tau}{2}$$

$$\alpha_4 = \frac{m_a}{\rho A K_Z}$$

$$\alpha_5 = \frac{\ell_2}{K_Z}$$

$$\alpha_6 = \frac{I_a}{\rho I K_Z}$$

$$d_1 = 1/[\gamma(3 - \beta)]$$

$$d_2 = d_1/\beta$$

$$d_3 = -\alpha_6 - 4\alpha_5$$

$$d_4 = 1/\left[2\left(\gamma + \alpha_5\right)\right]$$

$$d_5 = \left(2 - d_3 d_4\right)/4$$

$$d_6 = -\beta^2\gamma/2 - (1 + \beta) d_1 d_5$$

$$d_7 = (1 + \beta) d_2 d_5$$

$$e_1 = -d_1\left[(1 - \beta)\bar{Q}_W + 2\beta\bar{Q}_X\right] + d_2\left[(1 - \beta)\bar{W}_W + 2\beta\bar{W}_X\right]$$

$$+\left[(1 - \beta)\bar{\omega}_W + 2\beta\bar{\omega}_X\right]/(3 - \beta)$$

$$e_2 = \left(\bar{M}_X + \bar{\omega}_X + \beta^2\gamma\bar{Q}_X\right)/2 - d_4\left[\alpha_5\left(\bar{M}_X + \bar{\omega}_X + \beta^2\gamma\bar{Q}_X\right) - \alpha_6\bar{\omega}_W/4\right] + d_5 e_1 \quad .$$

The solution to Eqs. (7)-(12) in terms of dimensionless quantities is:

$$\bar{N}_Z = \alpha_4\left(\bar{N}_X + \bar{V}_W - \bar{V}_X\right)/\left(\alpha_4 + 4\gamma\right)$$

$$\bar{V}_Z = \bar{N}_Z - \bar{N}_X + \bar{V}_X$$

$$\bar{Q}_Z = \alpha_4\left(e_2 - d_7\bar{W}_W\right)/\left(\alpha_4 d_6 - 4\beta^2\gamma d_7\right)$$

$$\bar{W}_Z = \left(e_2 - d_6\bar{Q}_Z\right)/d_7$$

$$\bar{\omega}_Z = (1 + \beta)\left(\bar{W}_Z - \beta\bar{Q}_Z\right)d_2 - e_1$$

$$\bar{M}_Z = -\beta^2\alpha_5\bar{Q}_Z - \alpha_6\left(\bar{\omega}_W - \bar{\omega}_Z\right)/(4\gamma) \quad .$$

DISTRIBUTION LIST

DEPARTMENT OF DEFENSE

Director
Defense Advanced Rsch. Proj. Agency
ATTN: Technical Library

Director
Defense Civil Preparedness Agency
ATTN: Admin. Officer

Defense Documentation Center
Cameron Station
12 cy ATTN: TC

Director
Defense Intelligence Agency
ATTN: DI-7E
ATTN: DT-2, Wpns. & Sys. Div.
ATTN: Technical Library
ATTN: Charles A. Fowler
ATTN: DB-4C, Edward O'Farrell

Director
Defense Nuclear Agency
ATTN: SPAS
ATTN: DDST
ATTN: TISI Archives
3 cy ATTN: TITL, Tech. Library
5 cy ATTN: SPSS

Commander
Field Command, Defense Nuclear Agency
ATTN: FCPR

Director
Interservice Nuclear Weapons School
ATTN: Document Control

Director
Joint Strat. Tgt. Planning Staff, JCS
ATTN: STINFO Library

Chief
Livermore Division Fld. Command, DNA
ATTN: FCPRL

Under Sec'y of Def. for Rsch. & Engrg.
ATTN: S&SS (OS)

DEPARTMENT OF THE ARMY

Dep. Chief of Staff for Rsch. Dev. & Acq.
ATTN: Technical Library
ATTN: DAMA-CSM-N, LTC G. Ogden
ATTN: DAMA (CS), MAJ A. Gleim

Chief of Engineers
2 cy ATTN: DAEN-MCE-D
2 cy ATTN: DAEN-RDM

Deputy Chief of Staff for Ops. & Plans
ATTN: Technical Library
ATTN: Dir. of Chem. & Nuc. Ops.

Chief
Engineer Strategic Studies Group
ATTN: DAEN-FES

DEPARTMENT OF THE ARMY (Continued)

Project Manager
Gator Mine Program
ATTN: E. J. Lindsey

Commander
Harry Diamond Laboratories
ATTN: DRXDO-RBH, James H. Gwaltney
ATTN: DELHD-NP

Commander
Picatinny Arsenal
ATTN: Marty Margolin
ATTN: SMUPA-AD-D-A-7
ATTN: P. Angelloti
ATTN: Jerry Pantal
ATTN: Ray Moesner
ATTN: SMUPA-AD-D-M
ATTN: Technical Library
ATTN: SMUPA-AD-D-A
ATTN: B. Shulman, DR-DAR-L-C-FA
ATTN: Paul Harris
ATTN: Ernie Zimpo

Commander
Redstone Scientific Information Ctr.
ATTN: Chief, Documents

Commander
U.S. Army Armament Command
ATTN: Tech. Lib.

Director
U.S. Army Ballistic Research Labs.
ATTN: G. Roecker
ATTN: J. W. Apgar
ATTN: A. Ricchiazzi
ATTN: DRXBR-X
ATTN: J. H. Keefer, DRDAR-BLE
ATTN: DRXBR-TB
ATTN: G. Grabarek
2 cy ATTN: Tech. Lib., Edward Baicy

Commander and Director
U.S. Army Cold Region Res. Engr. Lab.
ATTN: G. Swinzow

Commander
U.S. Army Comb. Arms Combat Dev. Acty.
ATTN: LTC G. Steger
ATTN: LTC Pullen

Commander
U.S. Army Engineer Center
ATTN: ATSEN-SY-L

Division Engineer
U.S. Army Engineer Div., Huntsville
ATTN: HNDED-SR

Division Engineer
U.S. Army Engineer Div., Missouri Rvr.
ATTN: Tech Library

DEPARTMENT OF THE ARMY (Continued)

Commandant
U.S. Army Engineer School
ATTN: ATSE-CTD-CS
ATTN: ATSE-TEA-AD

Director
U.S. Army Engr. Waterways, Exper. Sta.
ATTN: Behzad Rohani
ATTN: William Flathau
ATTN: John N. Strange
ATTN: D. K. Butler
ATTN: Guy Jackson
ATTN: Technical Library
ATTN: Leo Ingram
ATTN: P. Hadala

Commander
U.S. Army Mat. & Mechanics Rsch. Ctr.
ATTN: Technical Library

Commander
U.S. Army Materiel Dev. & Readiness Cmd.
ATTN: Technical Library

Director
U.S. Army Materiel Sys. Analysis Acty.
ATTN: Joseph Sperazza

Commander
U.S. Army Missile Command
ATTN: F. Fleming
ATTN: W. Jann
ATTN: J. Hogan

Commander
U.S. Army Mobility Equip. R&D Ctr.
ATTN: STSFB-XS
ATTN: Technical Library
ATTN: STSFB-MW

Commander
U.S. Army Nuclear Agency
ATTN: Doc. Con.
ATTN: Tech. Lib.

Commander
U.S. Army Training and Doctrine Comd.
ATTN: LTC J. Foss
ATTN: LTC Auveduti, COL Enger

Commandant
U.S. Army War College
ATTN: Library

U.S. Army Mat. Cmd. Proj. Mngr. for Nuc. Munitions
ATTN: DRCPM-NUC

DEPARTMENT OF THE NAVY

Chief of Naval Operations
ATTN: OP 982, LTCOL Dubac
ATTN: Code 604C3, Robert Piacesi
ATTN: OP 982, CAPT Toole
ATTN: OP 982, LCDR Smith

Chief of Naval Research
ATTN: Technical Library

DEPARTMENT OF THE NAVY (Continued)

Officer-in-Charge
Civil Engineering Laboratory
ATTN: Technical Library
ATTN: R. J. Odello

Commandant of the Marine Corps
ATTN: POM

Commanding General
Development Center, Fire Support Branch
ATTN: LTCOL Gapenski
ATTN: CAPT Hartneady

Commander
Naval Air Systems Command
ATTN: F. Marquardt

Commanding Officer
Naval Explosive Ord. Disposal Fac.
ATTN: Code 504, Jim Petrousky

Commander
Naval Facilities Engineering Command
ATTN: Technical Library

Superintendent (Code 1424)
Naval Postgraduate School
ATTN: Code 2124, Tech. Rpts. Librarian

Director
Naval Research Laboratory
ATTN: Code 2600, Tech. Lib.

Commander
Naval Sea Systems Command
ATTN: ORD-033
ATTN: SEA-9931C

Officer-in-Charge
Naval Surface Weapons Center
ATTN: M. Kleinerman
ATTN: Code WA501, Navy Nuc. Prgms. Off.
ATTN: Code WX21, Tech. Lib.

Commander
Naval Surface Weapons Center
ATTN: Technical Library

Commander
Naval Weapons Center
ATTN: Code 533, Tech. Lib.
ATTN: Carl Austin

Commanding Officer
Naval Weapons Evaluation Facility
ATTN: Technical Library

Director
Strategic Systems Project Office
ATTN: NSP-43, Tech. Lib.

DEPARTMENT OF THE AIR FORCE

AF Armament Laboratory, AFSC
ATTN: Masey Valentine
3 cy ATTN: John Collins, AFATL/DLYV

DEPARTMENT OF THE AIR FORCE (Continued)

AF Institute of Technology, AU
ATTN: Library AFIT, Bldg. 640, Area B

AF Weapons Laboratory, AFSC
ATTN: SUL

Assistant Secretary of the Air Force
Research and Development
ATTN: Col R. E. Steere

Deputy Chief of Staff
Research and Development
ATTN: Col J. L. Gilbert

Commander
Foreign Technology Division, AFSC
ATTN: NICD Library

Hq. USAF/IN
ATTN: INATA

Hq. USAF/RD
ATTN: RDPM

Oklahoma State University
Fld. Off. for Wpns. Effectiveness
ATTN: Edward Jackett

Commander
Rome Air Development Center, AFSC
ATTN: EMTLD, Doc. Library

SAMSO/RS
ATTN: RSS

DEPARTMENT OF ENERGY

Albuquerque Operations Office
ATTN: Doc. Con. for Tech. Library

Division of Headquarters Services
ATTN: Doc. Con. for Class Tech. Lib.

Nevada Operations Office
ATTN: Doc. Con. for Tech. Lib.

Division of Military Application
ATTN: Doc. Control for Test Office

University of California
Lawrence Livermore Laboratory
ATTN: Jerry Goudreau
ATTN: Tech. Info., Dept. L-3
ATTN: Mark Wilkins, L-504

Los Alamos Scientific Laboratory
ATTN: Doc. Control for Reports Lib.
ATTN: Doc. Control for Tom Dowler

Sandia Laboratories, Livermore Laboratory
ATTN: Doc. Control for Tech. Library

Sandia Laboratories
ATTN: Doc. Con. for John Colp
ATTN: Doc. Con. for John Keizur
ATTN: Doc. Con. for William Patterson
ATTN: Doc. Con. for William Caudle
ATTN: Doc. Con. for W. Altemeirer
ATTN: Doc. Con. for 3141 Sandia Rpt. Coll.
ATTN: Doc. Con. for Walter Herrmann

OTHER GOVERNMENT AGENCIES

NASA
Ames Research Center
ATTN: Robert W. Jackson

Office of Nuclear Reactor Regulation
Nuclear Regulatory Commission
ATTN: Lawrence Shao
ATTN: Robert Heineman

DEPARTMENT OF DEFENSE CONTRACTORS

Aerospace Corporation
ATTN: Tech. Info. Services

Agbabian Associates
ATTN: M. Agbabian

Applied Theory, Inc.
2 cy ATTN: John G. Trulio

Avco Research & Systems Group
ATTN: David Henderson
ATTN: Research Lib., A830, Rm. 7201
ATTN: Pat Grady
ATTN: J200, W. Broding

Battelle Memorial Institute
ATTN: Technical Library

Acurex Corporation
ATTN: J. Huntington

The BDM Corporation
ATTN: Technical Library

The Boeing Company
ATTN: Aerospace Library

California Research & Technology, Inc.
ATTN: Technical Library
ATTN: Ken Kreyenhagen

Civil/Nuclear Systems Corp.
ATTN: Robert Crawford

EG&G, Inc.
Albuquerque Division
ATTN: Technical Library

Engineering Societies Library
ATTN: Ann Mott

General Dynamics Corp.
Pomona Division
ATTN: Keith Anderson

General Electric Company
TEMPO-Center for Advanced Studies
ATTN: DASIAC

Georgia Institute of Technology
Georgia Tech. Research Institute
ATTN: L. W. Rehfield
ATTN: S. V. Hanagud

Honeywell Incorporated
Defense Systems Division
ATTN: T. N. Helvig

DEPARTMENT OF DEFENSE CONTRACTORS (Continued)

Institute for Defense Analyses
ATTN: IDA Librarian, Ruth S. Smith

Kaman AviDyne
Division of Kaman Sciences Corp.
ATTN: E. S. Criscione
ATTN: Norman P. Hobbs
ATTN: Technical Library

Kaman Sciences Corporation
ATTN: Library

Lockheed Missiles & Space Co., Inc.
ATTN: Technical Library
ATTN: M. Culp

Lockheed Missiles and Space Co., Inc.
ATTN: Tech. Info. Ctr., D/Coll.

Martin Marietta Corporation
Orlando Division
ATTN: Al Cowan
ATTN: M. Anthony
ATTN: H. McQuaig

Merritt CASES, Incorporated
ATTN: J. L. Merritt
ATTN: Technical Library

University of New Mexico
Dept. of Campus Security and Police
ATTN: G. E. Triandafalidis

Nathan M. Newmark
Consulting Engineering Services
ATTN: W. Hall
ATTN: Nathan M. Newmark

Pacifica Technology
ATTN: R. Bjork
ATTN: G. Kent

Physics International Company
ATTN: Doc. Con. for Tech. Lib.
ATTN: Doc. Con. for Dennis Orphal
ATTN: Doc. Con. for Larry A Behrmann

DEPARTMENT OF DEFENSE CONTRACTORS (Continued)

R & D Associates
ATTN: Cyrus P. Knowles
ATTN: J. G. Lewis
ATTN: William B. Wright, Jr.
ATTN: Paul Rausch
ATTN: Harold L. Brode
ATTN: Technical Library
ATTN: Arlen Fields
ATTN: Henry Cooper

The Rand Corporation
ATTN: Technical Library

Science Applications, Inc.
ATTN: Technical Library

SRI International
ATTN: George R. Abrahamson
ATTN: Jim Colton
ATTN: H. E. Lindberg
ATTN: R. E. Emerson
ATTN: J. K. Gran

Systems, Science and Software, Inc.
ATTN: Edward Gaffney
ATTN: Robert Sedgewick
ATTN: Technical Library

Terra Tek, Inc.
ATTN: Technical Library

TRW Defense & Space Sys. Group
ATTN: Tech. Info. Center/S-1930
ATTN: Peter K. Dai, R1/2170

TRW Defense & Space Sys. Group
San Bernardino Operations
ATTN: E. Y. Wong, 527/712

Weidlinger Assoc. Consulting Engineers
ATTN: J. M. McCormick
ATTN: Melvin L. Baron

Weidlinger Assoc. Consulting Engineers
ATTN: J. Isenberg